Doctoral Thesis

Superhydrophobic surface coatings for protection against water-soluble chemical and biological contaminants

Ritesh Soni

School of Energy and Chemical Engineering

(Chemical Engineering)

Ulsan National Institute of Science and Technology

2023

Superhydrophobic surface coatings for protection against water-soluble chemical and biological contaminants

Ritesh Soni

School of Energy and Chemical Engineering

(Chemical Engineering)

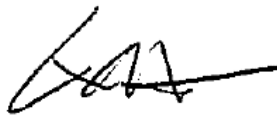Ulsan National Institute of Science and Technology

Superhydrophobic surface coatings for protection against water-soluble chemical and biological contaminants

A thesis/dissertation submitted to

Ulsan National Institute of Science and Technology

in partial fulfillment of the

requirements for the degree of

Doctor of Philosophy

Ritesh Soni

06.14.2023 of submission

Approved by

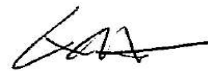_____

Advisor

Prof. Chang Young Lee

Superhydrophobic surface coatings for protection against water-soluble chemical and biological contaminants

Ritesh Soni

This certifies that the thesis/dissertation of Ritesh Soni is approved.
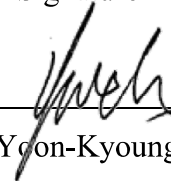
06.14.2023 of submission

Signature

Advisor: Prof. Chang Young Lee

Signature

Prof. Yoon-Kyoung Cho

Signature

Prof. Young-Nam Kwon
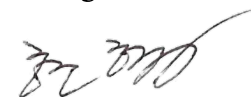
Signature

Prof. Chunggi Baig

Signature

Prof. Hyunhyub Ko

Signature

Abstract

Superhydrophobic surface coating materials have been inspired by many natural systems like lotus leaf and insect wings. Due to their remarkable anti-wetting behavior, superhydrophobic coating materials have been used in a wide range of applications. Regardless of their promising functionalities, commercial accessibility of these materials is still inadequate due to encountering several challenges in terms of material compatibility, robustness, cost, complexity, uniformity, scaling-up hitches, and durability. While there is abundance of reported methods for fabrication of artificial superhydrophobic surfaces, the consideration of these limiting factors is critical for the broader applicability of superhydrophobic surfaces.

The aim of thesis is to promote the broader applicability of superhydrophobic surfaces for use in protection from biological and chemical contaminants in real-life applications. This aim has been achieved by investigating the current limitations of uncoated surgical face mask surfaces and attempting to solve them by developing simple coating method for making reusable superhydrophobic surgical face mask for protection against bacteria and virus (Chapter 2). Following this, bio-adhesive based eco-friendly and fluorine-free nanocoating has been developed for various solid and porous substrates to use it for protection against water-soluble chemical contaminants like acid rain and organic dyes (Chapter 3). After that, fabrication of superhydrophobic sand for increasing water withholding capacity of agricultural land for arid regions and use this modified sand for oil/water separation (Chapter4).

Acknowledgments

I would like to express my gratitude to all who contributed ideas, encouragement, and support. I would like to thank, firstly, Shiv Baba for giving me grace and wisdom.

I would like to convey my deep sense of gratitude to my supervisor, Prof. Chang Young Lee, Associate Professor, School of Energy and Chemical Engineering, Ulsan National Institute of Science and Technology (UNIST), South Korea. His continuous motivation and support at every stage of my PhD research journey encouraged me to give my best efforts. His vast experience on nanomaterials and their applications helped me to resolve practical issues and design the experiments. Apart from the knowledgeable guide he is a person with humble and kind heart. He has always supported me throughout my degree program to achieve my research goals. He has always guided me in both professional and personal situations during my stay at UNIST.

It is my pleasure to thank, Prof. Young-Nam Kwon, Prof. Yoon-Kyoung Cho, and Prof. Gun-Ho Kim for their help and collaboration on multiple research projects and expand my horizon of knowledge in interdisciplinary research areas during my degree program in UNIST. I wish to express my sincere gratitude to Dr. Saikat Sinha Ray, Dr. Sumit Kumar, and Dr. Shalik Ram Joshi for being my research collaborators and providing me with their valuable discussions.

I want to thank all my colleagues in Carbon Nanomaterials Lab, UNIST for their warm hospitality and providing me with a very co-operative ambience, in which completing my work was a privilege and pleasure. I would like to thank Dr. Yun-Tae Kim, Dr. Jae Hong Choi, Dr. Hyegi Min, Dr. Seung Min Moon, Dr. Sanghwan Park, Dr. Sook Yoon, Dr. Deukyeon lee, Ms. Anar Zhexembekova, Mr. Seongwoo Lee, Mr. Yongsic Kim, Mr. Seoungyeop Lim, Ms.

To my parents.

Contents

Chapter 2. Superhydrophobic Face Mask   19

Chapter 3. Bio Adhesive based Superhydrophobic Coating   45

Chapter 4. Superhydrophobic Sand   **65**

Chapter 5. Conclusion and Future Work   **84**

List of Figures

Figure 2.12: Photothermal performance of the masks (A) Schematic of the setup used for photothermal studies. (B) Time-lapse thermal images of the CNT-coated mask. (C) Human dummy wearing a CNT-coated mask showing the temperature increase at 1 sun intensity. (D) Surface temperature measured by an IR camera against time for the pristine (black curve) and the CNT-coated (red curve) masks. (E) Reflectance spectra of the pristine (black curve) and the CNT-coated (red curve) masks. (F) Temperature of the CNT-coated mask under multiple on/off cycles of 1 sun illumination.

Figure 2.13: Solar illumination effects on CNT-coated mask surface. (A) Optical photograph of solar simulator setup (B) Contact angles measured after 10 cycles under solar illumination (C) SEM image of CNT-coated poly propylene fibers of the mask before solar illumination (D) SEM image of CNT-coated poly propylene fibers of the mask after 10 cycles of solar illumination (E) Human wearing CNT-coated mask IR image under direct sun light at around 9 AM (F) Human wearing CNT-coated mask IR image under direct sun light at around 12 PM (G) Human wearing CNT-coated mask IR image under direct sun light at around 3 PM (H) IR image of CNT-coated mask back side under direct sun light at around 12 PM (I) IR image of CNT-coated mask kept on ground under direct sun light at around 12 PM (J) Human wearing pristine mask IR image under direct sun light at around 12 PM.

Figure 2.14: Electrothermal effect on CNT-coated mask surface. (A) Optical photograph of electrothermal setup (B) IR image of CNT-coated mask sample at 10 volts (C) IR image of CNT-coated mask sample at 20 volts (D) IR image of CNT-coated mask sample at 30 volts (E) On/Off response for CNT-coated mask at 10 volts (F) On/Off response for CNT-coated mask at 20 volts (G) On/Off response for CNT-coated mask at 30 volts.

Figure 2.15: Antimicrobial and antiviral properties. (A) Detection of the antibacterial effect (CFU mL^{-1}) of the *E. coli* ATCC 25922 bacteria on the pristine and the CNT-coated masks under dark and light conditions. (B) High-resolution confocal fluorescence microscopy images of the live/dead assay of *E. coli* ATCC 25922 stained with SYTO 9 and propidium iodide. (C) Number of viable *E. coli* bacteria calculated from CFUs after solar illumination of the surfaces of the control (glass surface), pristine, and CNT-coated masks. Data are expressed as mean ± standard deviation values; n = 3 independent experiments. (D) Changes in the concentration of the VPs on the control, pristine, and CNT-coated masks under dark and light conditions. (E) Representative SDS-PAGE electrophoresis data for the control, pristine, and CNT-coated masks after treatment of VPs under light mode.

Figure 2.16: Characterization of virus-like particles (VPs). (A) Slope obtained from Bicinchoninic acid assay (BCA) of the standard protein to calculate the concentration of VPs (B) Size distribution of VPs.

Figure 3.1: Schematic representation of making process of SSO coating solution.

Figure 3.2: Surface morphology analysis of uncoated and SSO coated substrates (A) polypropylene (B) SSO coated pp (C) glass (D) SSO coated glass (E) polyethylene terephthalate (F) SSO coated pet.

List of Equations

List of Tables

Chapter 1

Introduction

1.1 Superhydrophobicity: Definition and Requirements

Water interaction with surfaces has been an area of interest for many decades. Mother Nature is full of interesting surface designs that are structures to interact with water in an explicit manner. Surfaces with both high and low interaction to water droplets are significant to numerous real-life applications, which indicates the importance of studying surface wettability and emerging approaches to manipulation it depends on the required outcome.[1-3] Superhydrophobic surfaces are illustrated by its superior water-resistant properties and have been used for many applications.[4] These applications comprises self-cleaning surfaces,[5] anti-fouling,[6] drag reduction,[7] anti-icing,[8] face masks,[9] anti-fogging,[10] anti-corrosion,[11] oil/water separation,[12] energy saving,[13] historical stones artifact protection,[14] and agriculture sector.[15] In the nature superhydrophobic surfaces are also commonly observed, from the *Salvinia Molesta* leaves that can show anti-water properties for several weeks below water submersion, [16, 17] to water spider called *Gerris remiges* which can stand on the water surface.[18, 19] The 'Lotus effect' is the mostly recognized example of natural existing water-resistant surface for lotus leaf.[20, 21]

1.1.1. The Lotus Effect and Self-cleaning mechanism

Lotus leaves show impressive self-cleaning abilities (Figure 1.1) due to micro/nano structural textures, with as added layer of smaller scale hair like structures covering both surface protrusions and the plane areas as shown in scanning electron microscope (SEM) images (Figure 1.1). These micro/nanostructures were exhibited to cause air to be trapped beneath

water droplet upon wetting the surface, which allows the droplet rolling-off the surface activity.[20] The Lotus effect can be explained by the self-cleaning process on the surface of lotus leaf (*Nelumbo nucifera*).[22] As shown in the Figure 1.2, While a water droplet would generally slide along a sloped hydrophilic surface and shows strong interaction with the present dirt or bio contaminants, a surface with a superhydrophobicity would cause the near-spherical water droplet to roll-off across the surface instead and shows self-cleaning ability. This rolling-off action increases the chances of picking up water-soluble biological and chemical contaminants (dirt particles, bacteria, organic dyes etc.) attached on the surface.[20]

(A) **(B)** **(C)**

(D) **(E)** **(F)**
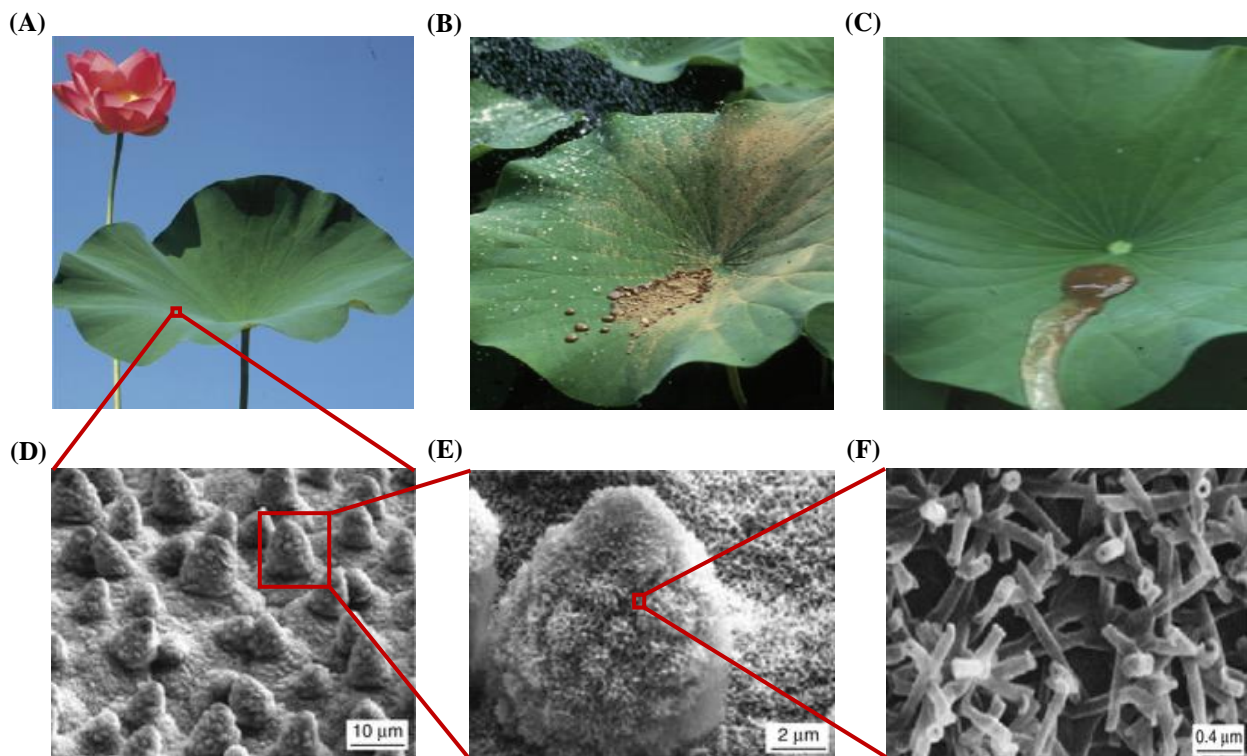
Figure 1.1: The lotus effect (A) image of lotus leaf (*Nelumbo nucifera*) (B) dirt present on lotus leaf (C) self-cleaning ability of the leaf surface (D, E, F) SEM Images of lotus leaf at different magnifications. Reproduced with permission.[21] Copyright 2009, Elsevier.

1.1.2. Characterization of Superhydrophobicity

(A)

Hydrophilic surface

(B)

Superhydrophobic surface
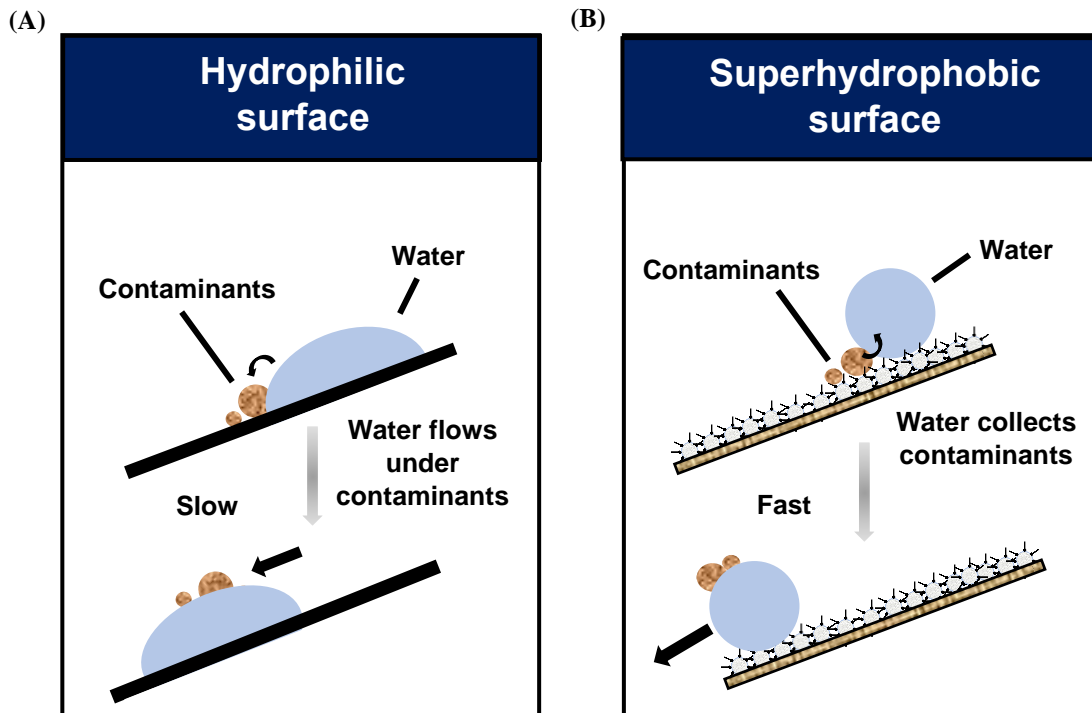
Figure 1.2: Self-cleaning properties (A) contaminants sticking phenomena on a hydrophilic surface (B) Self-cleaning process on superhydrophobic surface.

Surface wettability measurement has been obtained by using many approaches to differentiate between hydrophilic and hydrophobic surfaces. Water contact angle (WCA) measurement is the most used method for surface wettability analysis. The WCA of a surface is evaluated by the surface water contact place to tangent line of water-air contact.[4] As shown in Figure 1. 3, a surface is defined as superhydrophilic when $\theta < 10°$, and as hydrophilic when $\theta < 90°$. In contrast, superhydrophobic are defined by contact angles as hydrophilic when $\theta > 150°$ and $\theta > 90°$, respectively (Figure 1.3) due to water resistant spreading phenomena.[23] A minimum contact angle is obtained for superhydrophilic surface where the water droplet show complete spreading and wets the surface but when droplet form a near-spherical droplet on the surface then a maximum contact angle is obtained.[24]

Measurement of WCAs is extensively used and accepted to evaluate water interaction with

3

Different wetting stages of water droplet

(A) $\theta < 10°$ — Superhydrophilic state

(B) $\theta < 90°$ — Hydrophilic state

(C) $\theta > 90°$ — Hydrophobic state

(D) $\theta > 150°$ — Superhydrophobic state
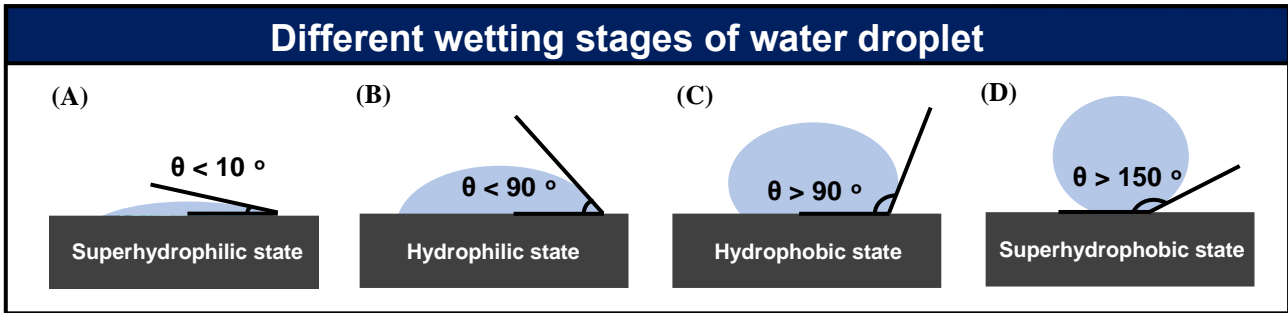
Figure 1.3: Different wetting stages of water droplet (A, B, C, and D) wetting stage of superhydrophilic surface, hydrophilic surface, hydrophobic surface, and superhydrophobic surface.

surfaces. The water droplet rolling-off behavior make some surfaces to be 'slippery' and on the other hand where droplet bonds to the surface strongly and can be hard to remove entirely shows a 'pinning effect'.[25] Hence, contact angle hysteresis (CAH) method has been developed to complement WCA analysis by differentiating between 'sticky' and 'slippery' surfaces. CAH is one of the prominent factors in surface chemistry to understand sticky or non-sticky behavior of substrates. As shown in Equation 1.1, It is defined as the difference between the maximum advancing contact angle (θ_A) and minimum receding contact angle (θ_R) which is usually used to analysis the wetting tendency of the surfaces.[26]

$$CAH = \theta_A - \theta_R \qquad \qquad ……(Equation\ 1.1)$$

Typically, θ_A shows the maximum contact angle, whereas θ_R exhibits the minimum contact angle for water droplet on a surface (Figure 1.4). Intriguingly, it was observed that a higher contact angle hysteresis value provides higher degree of water droplet adhesion and have higher tendency of corrosion for a surface. Mostly, superhydrophobic surfaces is non-adhesive, anti-corrosive and shows exceptionally low water contact angle hysteresis.[27] In other words, lower

contact angle hysteresis value ($< 10°$) of superhydrophobic surfaces corresponds to high wetting stability against Cassie-Baxter to Wenzel transition.[28]
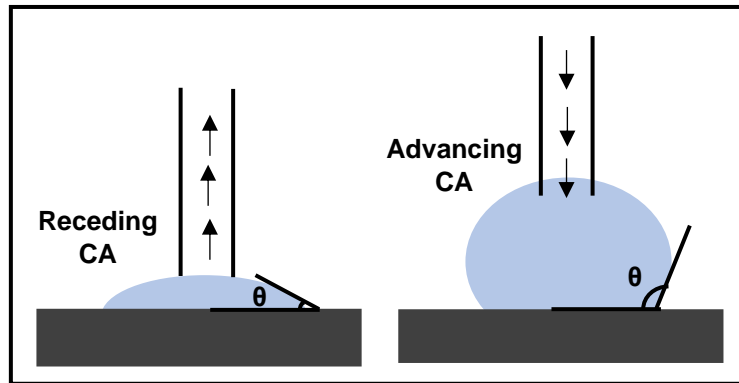
Figure 1.4: Contact angle hysteresis phenomena (A) maximum receding contact angle of a surface (B) maximum advancing contact angle of a surface.

Alternate approaches have been reported for a similar purpose. The sliding or rolling-off angle is determined by slow surface tilting and observing the angle at which the water droplet starts to roll-off from surface. Superhydrophobic surfaces usually have a sliding or rolling-off angle $< 10°$.[4]

1. 2 Wetting Models

It is particularly important to identify and predict the interaction between the water droplet and surface to evaluate the wetting behavior of the surface and its applicability in various domains. For these reasons, wetting models for surfaces were utilized to understand the interaction between solid/water/air and to predict the wetting behaviour.[4]

1.2.1 Young's Model

Young's Model is believed to be the easiest wetting model. This model envisions an "ideal surface" that is chemical homogenous and entirely smooth. To show the resulting equilibrium

contact angle this model utilizes interfacial surface tensions/energies (per unit area) (Equation 1.2, Figure 1. 5A).[29]

$$\gamma SA = \gamma SL + \gamma LA \cos \theta_y \qquad \qquad \ldots\ldots(\text{Equation 1.2})$$

When the three interfacial tensions [solid-air (γSA), solid-liquid (γSL), liquid-air (γLA)] balance and reach thermodynamic equilibrium then the contact angle (θ_y) is determined. In the case of hydrophobic surface, the solid-liquid interfacial energy (γSL) should surpass the solid-air interfacial energy (γSA) and the water droplet changes its shape to minimize the solid-liquid interfacial area until the lowermost possible energy state of the system is reached. The opposite is true for hydrophilic wetting behavior when the contact angles are $\theta < 5°$ for superhydrophilic and $\theta < 90°$ for hydrophilic surface. It happens because of solid-liquid interfacial energy (γSL) being minimized and favoring surface and water droplet interaction.

Young's model explains the wetting behavior for ideal surface which hardly exists. The contact angle of a surface can be increased even without changing the chemical composition solely by increasing surface roughness of the surface which is not possible to explain by this model.[4] There are alternative wetting models to clarify the wetting behavior of real-life solid surfaces. [30, 31]
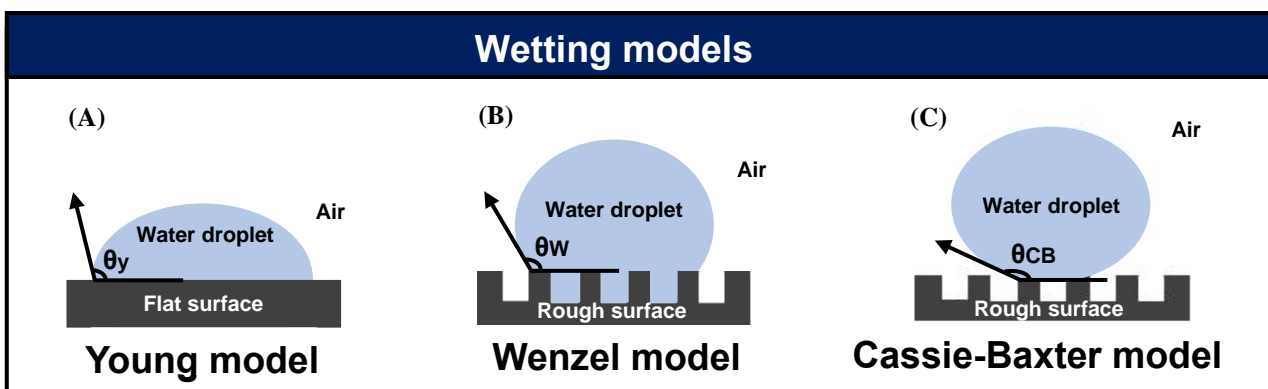
Figure 1.5: Wetting models for a droplet (A) Young's model (B) Wenzel model (B) Cassie-Baxter model.

1.2.2 Wenzel Model

A correction factor has been established to explain surface roughness, referred to as the roughness factor (r). The roughness factor (r) is defined as the ratio of the true surface area and planned surface, which is higher than 1 for any rough surface.[32] As shown in Figure 1.5B, the Wenzel model envisions an entire wetting for a rough surface, it means that under the water droplet there is no air trapped.[4] Wenzel model has been utilized to link surface wettability with both surface roughness and surface interfacial tensions through the direct insertion of a roughness factor (Equation 1.3).[30, 33]

$$\cos\theta_w = r\cos\theta_y = r(\gamma_{SA} - \gamma_{SL})/\gamma_{LA} \qquad \text{.......(Equation 1.3)}$$

Where θ_w is the Wenzel contact angle, and θ_y is Young's contact angle. This equation mathematically suggests that as the surface gets roughened, the surface properties being magnified which indicates that the WCA increases when a hydrophobic surface roughness increases.[4]

1.2.3 Cassie-Baxter Model

C-B model also explains roughness of the surface. Opposite to Wenzel model in which entire wetting is presumed, the C-B model implies the development of air gaps under the water droplet because of trapped air not being removed by wetting.[4] As shown in Figure 1.5C, for C-B model, water droplet is imagined standing on the surface roughness and air pockets between the protrusions, so their contact with the surface is avoided. The C-B equation can be written as: [30, 33, 34]

$$\cos\theta_{CB} = f_s \cdot \cos\theta_s + f_v \cdot \cos\theta_v \qquad \text{.........(Equation 1.4)}$$

Where f_s and f_v are the area fractions of solid and air under the droplet on the surface respectively. Considering f_{s+} $f_{v=}$ 1, the equilibrium contact angle between droplets and surrounding vapor is a constant of 180°, and equilibrium contact angle of droplet on the solid substrate equals to Young's θ_y, the C-B equation can be simplified as:

$$\cos\theta_{CB} = f_s \, (1 + \cos \theta_Y) - 1 \qquad \qquad \text{.......(Equation 1.5)}$$

From the Wenzel model, it can be established that surface roughness factor (r) amplifies the wettability of the original surface. In the C-B model, the area fractions under the droplet are important because if the area fraction of air is significantly large, then the WCA will be higher. These models have been broadly utilized lately with dynamic research for superhydrophobic surfaces even though these wetting models were established over half a century ago.[4]

1.3 Fabrication Methods for Superhydrophobic Surfaces

Superhydrophobic surface making approaches are various and follow diverse fabrication methods. There are range of approaches for creating of surfaces roughness and broad selection for utilizing materials with low surface energy.[24] These methods can be categorized for creating rough surfaces, which falls into two main classifications: i) top-down methods; in which to create surface roughness structuring of the surface with bulk material, and ii) bottom-up methods; small scale material addition to the surface is used for creating roughness.[35]

1.3.1   Top-Down Methods

In this section the methods discussed, bulk substrates are structured to produce roughness. This goal can be achieved by soft material imprinting using a mould or by the selective exclusion of hard materials. Some of the common 'top-down´ method examples for making superhydrophobic surfaces are presented here.

1.3.1.1 Lithography

Lithography technique is a broadly utilized method to create small-scale patterns on substrates and thin films. The most known lithography method is photolithography, in which substrate gets coating with thin layer of photoresist, then exposed (by Electron beam, X-ray, UV etc.) through a photo or chrome mask prepare with specific pattern, letting the design transfer into the substrate. Furthermore, development steps are required to eliminate the exposed (or the unexposed) photoresist material and make a positive (or a negative) replica. This step can be followed by post treatment with a hydrophobic material.[36, 37]

Feng at el. reported the fabrication of hierarchical SU-8 surfaces thorough a double Electron beam lithography (EBL) exposure method. Initially, a layer of SU8 was spin coated onto silicon wafer with thickness of 10um and 15um followed by single EBL exposure and post-exposure bake, a thin layer of SU-8 of around 500nm in thickness was spin coated on the top of
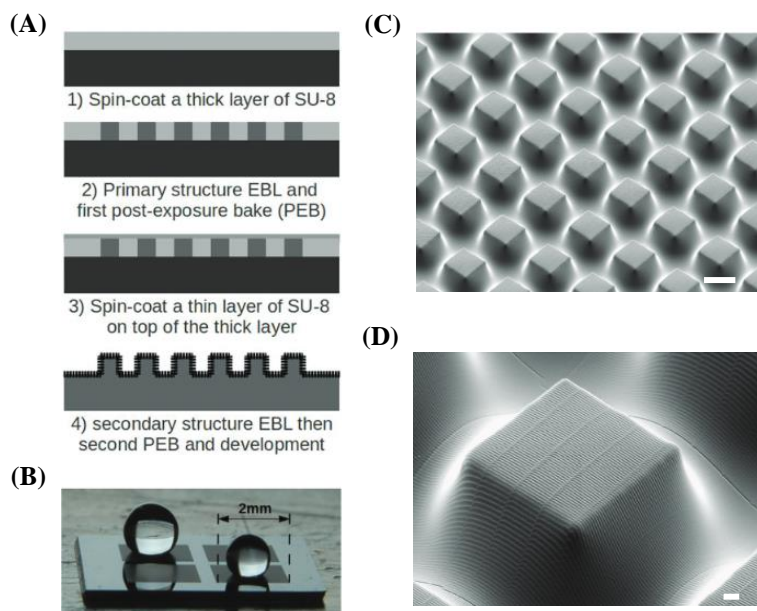
Figure 1.6: Lithography for making superhydrophobic surface (A) schematic diagram of a double layer e-beam lithography process to make hierarchical SU-8 surfaces (B) macroscopic

superhydrophobic surface with 2 mm linear dimension (C, D) SEM images of SU-8 structure

on different magnifications (10μm, 1μm). Reproduced with permission.[36] Copyright 2011,

Wiley.

undeveloped layer then exposed again with EBL to create the secondary features over the

complete surface (Figure 1.6). This process produces micro/nano hierarchical structures in

which nano size structures covering not only the tops of the micrometer structures but also their

sidewalls and valleys between them. [36]

1.3.1.2 Etching

Etching is a modest method to increase the surface roughness of the substrates. In many cases

superhydrophobicity can be obtain by modification of the etched substrate using low surface

energy material.[38] Etching can be performed through chemical routes for removal of substrate

materials by exposure to harsh solutions (basic or acidic). Kim et al. demonstrated the making

of stainless steel based superhydrophobic surfaces by hydrogen fluoride (HF) etching and

further treatment with a hot 0.1% NaCl solution, followed by fluorination treatment. As shown

in Figure 1.7, Stainless steel without any treatment shows hydrophilic behavior, after treatment

with HF etching the water contact angle (WCA) of 164°, and further treatment with 0.1% NaCl

solution increased the water contact angle (WCA = 168°). It happens because of the petal-like

structures formation on the stainless steel surface by etching (Figure 1.7).[39]

1.3.2   Bottom-Up Methods

In this section methods discussed related to ´bottom-up´ methods in which the small

hydrophobic blocks assembling to create a rough superhydrophobic surface. Some of these

approaches' examples overview is presented here.

(A)
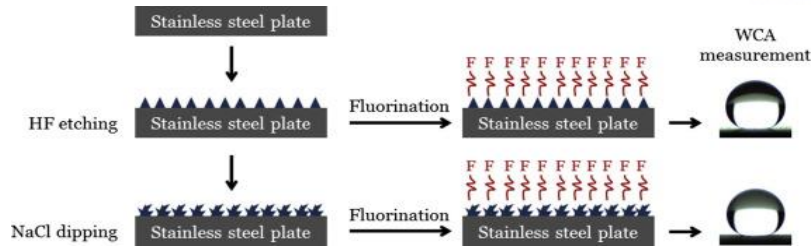
(B)
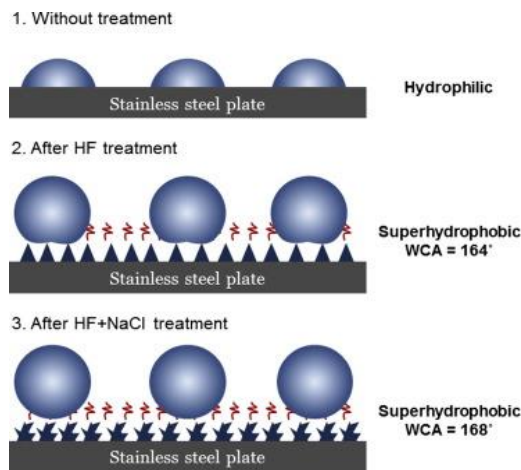
(C)
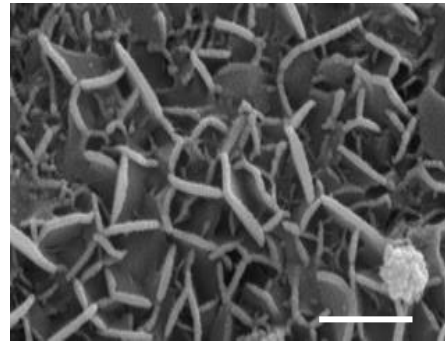
Figure 1.7: Etching process for making superhydrophobic surface (A) schematic representation of the different steps to make stainless steel surface superhydrophobic by etching method (B) schematic diagram of the hydrophobic sates of stainless steel before and after chemical etching treatments (C) SEM images of surface after dipping with 0.1% NaCl solution (500 nm scale). Reproduced with permission.[39] Copyright 2018, Elsevier.

1.3.2.1 3D Printing

3D printing has been reported for making superhydrophobic surfaces. This method involves layer-by-layer surface creation and provides great control over the construction parameters. Kang et al. prepared a mold by using 3D printer to create roughness on PDMS surface to obtain superhydrophobicity. This 3D printing mold was created as a support part using different printing angles and then PDMD was poured. Furthermore, this PDMS was degassed to remove

bubbles and then baking and detaching process was performed to create superhydrophobic

PDMS surface (Figure 1.8).[40]
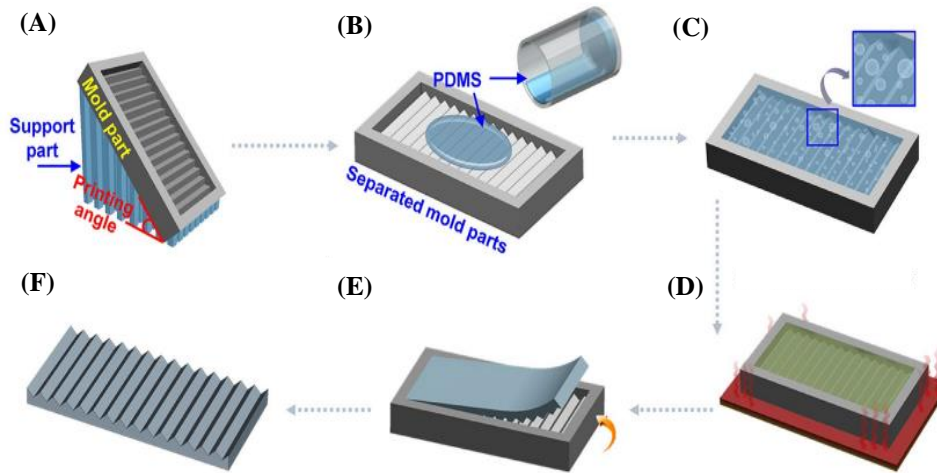
Figure 1.8: 3D printing method for making superhydrophobic polymer surface (A) mold

printing with a support part using different printing angles (B) PDMS pouring onto the mold

(C) degassing process for remove air bubbles (D) baking process for curing of the polymer (E)

cured PDMS detachment from the mold (F) superhydrophobic surfaces. Reproduced with

permission.[40] Copyright 2019, Springer.

1.3.2.2 Chemical Vapour Deposition

Chemical vapour deposition (CVD) method implies gaseous-phase precursors deposition to

form a solid product. In this method, heating is broadly utilized to begin the chemical reaction,

and removal of any unreacted material from the system. The morphology of the deposited

coatings has been controlled by using various CVD techniques. Huang et al. have demonstrated

nano cone array coatings using a two-stage initiated CVD (iCVD) process to make glass slide

and Silicon wafer superhydrophobic. First, they introduced initiator tert-butyl peroxide (TBP)

and a monomer ethylene glycol diacrylate (EDGA) into iCVD reactor. This initiator gets

thermally decomposed and the resultant free radicals were adsorbed onto substrate surface

along with the monomer, initiating polymerization and deposition of poly (ethylene glycol diacrylate) (pEDGA). This PFDA vapor believed to condense on the substrate and start forming nanosized nucleation center where monomer vapor helps to growth of nano cone array (Figure 1.9).[43]
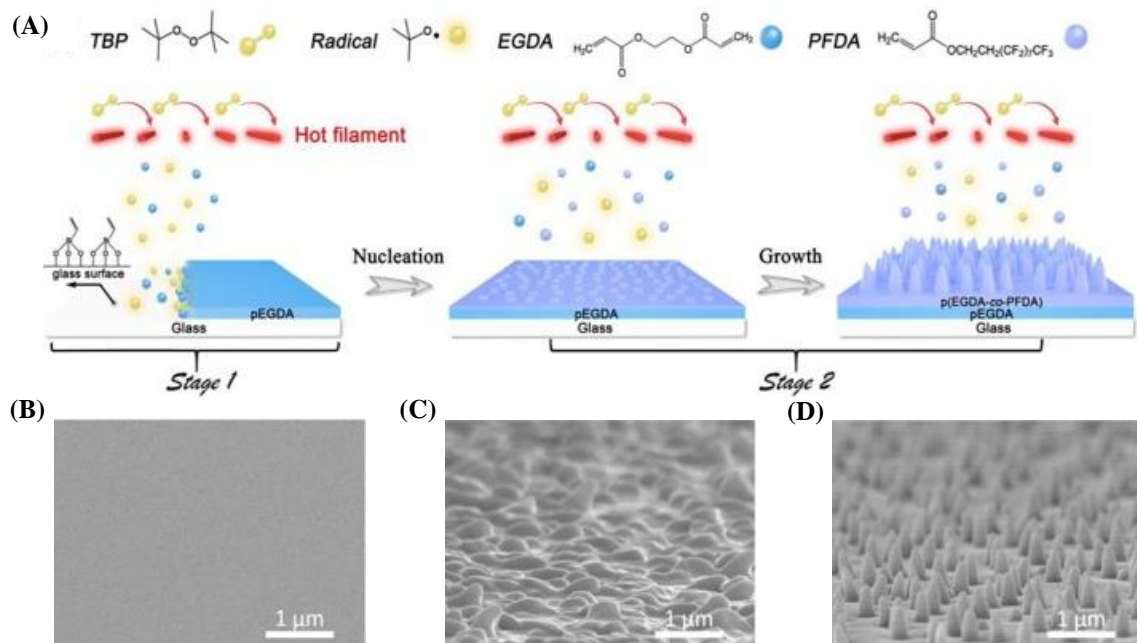
Figure 1.9: Chemical vapour deposition (CVD) process for making superhydrophobic surface (A) Schematic representation of the CVD growth process of polymer nano cone array coatings (B) SEM images of flat coating (C) irregular rough coating (D) nano cone array coating. Reproduced with permission.[43] Copyright 2023, Elsevier.

1.4   Factors Limiting Broder Application of Superhydrophobic Surfaces

Superhydrophobic surfaces distinctive interaction with water droplets results in various abilities that are useful for numerous real-life applications like self-cleaning surfaces,[5] anti-icing,[8] reusable face masks,[9] heritage stone artifacts protection from acid rain,[14] concrete modification,[44] and superhydrophobic sand [45] (Figure 1.10).

13

Figure 1.10: Real-life applications of superhydrophobic surfaces.

Superhydrophobic surfaces have been prepared using a wide range of fabrication techniques, materials, resultant properties to target wide range of target applications but still these surfaces impact on daily use materials is inadequate. There are many limitations for utilizing these superhydrophobic surfaces for numerous applications and these limitations can be categorized two main categories: issues related to the scaling-up and fabrication methods and difficulties with their efficiency/durability.

1.4.1   Scaling-Up and Fabrication Methods Restrictions

Fabrication of superhydrophobic surfaces have been demonstrated successfully at the research laboratory scale but a lot of issues can arise when scaling-up for daily life use. Scaling-up is even more challenging due to most of the fabrication main module and stages like materials, fabrication process, conditions, and post-processing. The materials used, while possibly giving

14

good hydrophobicity and excellent performance, can be expensive and affect our environment. In the case of fluorinated alkyls which are well known for their superhydrophobicity and low surface energy,[46, 47] still potentially harmful to humans due to presence of long-chain fluorocarbons.[47] Another case is when the hydrophobic module of the superhydrophobic surface can be safe for environment and humans, but they may require dissolving in toxic solvents to enable the process.

The fabrication procedure can involve many issues like most of the fabrication method may require specific substrate only to make surface superhydrophobic which does not provide flexibility in term of choosing desire substrates.[48] For synthesis approaches, sometime additional heating of the substrate is required to bake the deposited coating which adds more cost and limits the choices for desired substrates.

Another issue is utilization of complex and high-tech equipment to create micro/nanoscale roughness on the specific substate which adds more complexity and leads to cost-ineffective and longtime process. There is another issue related to non-uniformity of the coating which can decrease the long-term use of the superhydrophobic surfaces due to creation of defective region that will increase chances of surface degradation in harsh environmental conditions. Uniform coating can be achieved by using high tech equipment but again it is going to hinder its use for scaling-up for daily use applications.

These issues are keep increasing and has led to new research possibilities that endeavor at making of superhydrophobic surface through more 'industrial-friendly' methods to facilitate varied range of applications.[49]

1.4.2   Durability and Reusability Concerns for Daily Life Challenges

There are various new challenges facing the surface in real-life environment. The harsh environment can affect the surface properties and can degrade its performance in term of superhydrophobicity. The surface superhydrophobicity loss can happen because of multiple reasons like physical damage, chemical damage and change in the wetting mechanism.[50]

As shown in Young's model (equation 1.2), the WCA decreases when the surface energy increases of the coating material. Surface chemistry can be changed by destroying the surface and either by hydrophobic surface functional groups removal because of exposure with harsh environmental circumstances (e.g., acid rain and extreme high temperature) or by chemical pollutants onto the surface (e.g., organic chemicals, surface fouling, and hard water staining).[51]

Physical scratches on superhydrophobic surface also are main constraint. Surface that contains micro/nanoscale features can be simply damaged by nominal physical load as little as finger wipe sometimes.[48, 52, 53] This limitation makes the use of the surface for applications where abrasion or scratching is happening comely. [54]

Superhydrophobic surface can lose their performance by moving from C-B to Wenzel wetting state (i.e., loss of trapped air). This can happen using different stimuli, like the diffusion of air into water, increasing the hydrostatic pressure or water droplet condensation inside air pockets.[55]

1.5 Thesis Outline

As mentioned in the previous section, and while the development and fabrication of new surfaces with superhydrophobicity are yet needed, the investigation of mentioned issues is critical in term of surface implementation for daily use applications. The main objective of the research work demonstrated in this thesis was to uphold the real-life applications of

superhydrophobic surfaces to protect from biological and chemical contamination, which took different routes in each chapter.

❖ Chapter 2 aims to show the development of self-sterile and reusable facemask to protection against biological contaminants (bacteria and virus) was main aim in Chapter 2, where a single-step spray-coating technique reported for the formation of a superhydrophobic layer contain nanospike-like architecture of single-walled carbon nanotubes (SWCNTs) on melt-blown polypropylene (PP) surgical mask. This CNT-coated mask showed superhydrophobicity for various body fluids (urine, tear, blood, sweat, and saliva) and water. The outstanding photothermal properties make this mask reusable and self-sterile ability against bacteria and viruses.

❖ Chapter 3 aims to show the development of facile, fluorine-free, economical, and scalable fabrication method that utilizes bio adhesive shellac and modified silica nanoparticles to create anti-droplet and durable superhydrophobic coatings. The newly developed bio adhesive based nanocoating was applied by using spray coating on to multiple solid and porous substrates such as nonwoven polypropylene fibers, glass, plastic, metal, wood, cotton, and concrete material to achieve excellent superhydrophobicity. This nanocoating creates micro/nanoscale roughness on the surface and exhibits anti-droplet effect for acid rain. Furthermore, the coated surfaces demonstrated excellent durability against abrasion and high temperature environments exposure tests while maintaining anti-droplet behavior.

❖ Chapter 4 aims to demonstrate the development of a single step method, superhydrophobic sand to prevent loss of water from topsoil in arid regions. Sea sand (SS) and regular sand was coated with silica sol, which was prepared by the hydrolysis of tetraethoxysilane (TEOS) under alkaline conditions, followed by

treatment with perfluorodecyltrichlorosilane (FDTS). The coated superhydrophobic sand grains displayed anti-droplet and self-cleaning features, and withheld water for extended periods of time, which was also further used to demonstrate oil/water separation application.

Chapter 2

Superhydrophobic Face Mask

2.1 Introduction

The outbreak of coronavirus has jeopardized the world by infecting more than 688 million and killing over 6.8 million people as of May 2023.[56] To reduce the virus spread, World Health Organization recommends the use of medical mask, and some countries have mandated the usage of medical masks in public places, especially those with a high population density.[45, 57] Airborne transmission occurs through virus containing respiratory droplets floating in the air over long distances,[58-61] and the use of masks can reduce the virus spread.[62] Although low-cost masks are currently available,[63, 64] their poor hydrophobicity increases the adherence of the droplets on the surface.[65, 66] Furthermore, the poor reusability of the currently used medical masks adversely affects the environment because improper disposal or decontamination of used masks generates 250,000 tons of wastes a day globally.[67, 68] Therefore, there is an increasing demand for low-cost and reusable surgical masks with self-sterilization capability and outstanding hydrophobicity.

We present a convenient approach for preparing a self-sterilizing and reusable mask for protection against biological contaminants (bacteria, virus etc.), by spray-coating the commercially available surgical masks with single-walled CNTs (SWCNTs) to achieve outstanding hydrophobic and photothermal properties. The coated SWCNTs form randomly oriented nanoscale needle-like architectures on the mask surface, leading to a superhydrophobic surface characteristic that causes the aqueous droplets to bounce off immediately. Upon illumination with sun light, the surface temperature of the functional mask increases instantly to more than 90 °C, confirming bactericidal and virucidal property of the CNT-coated mask. Our approach for fabricating a reusable mask is easily scalable and thus is

expected to minimize environmental impact of the daily-worn masks, while suppressing spread of the diseases transmitted by respiratory droplets.

2.2 Materials and Methods:

2.2.1 Materials: SWCNTs (HiPco SWCNTs, diameter, 0.8–1.2 nm) were purchased from Nano Integris (Canada). Benzene and isopropanol were purchased from Sigma-Aldrich and used as received.

2.2.2 Sample preparation: The as-received SWCNT was dispersed in benzene by sonication in an ultrasonic bath (BRANSON 2510, Marshall Scientific, UK) for 60 min. The concentration of the SWCNTs was optimal at 2.5 mg mL^{-1}, exhibiting a uniform surface coverage of the SWCNTs (Figure 2.1). Before spray-coating, the SWCNT suspension was vigorously stirred for 1 min on a vortex mixer (WiseMix VM-10, Germany) to redisperse any SWCNTs aggregates. The obtained suspension was uniformly coated on bare surgical masks using a manual spray-coater. The spray-coated samples were then kept in a vacuum oven maintained at constant temperature (80 °C) for 30 min. These samples were further ultrasonicated in benzene for 1 min to remove excess SWCNTs that were not directly bound to PP fibers, which helped preserve the air permeability and reduce the risk of inhaling SWCNTs while breathing. The mask was dried again in the oven to ensure the complete removal of the benzene.
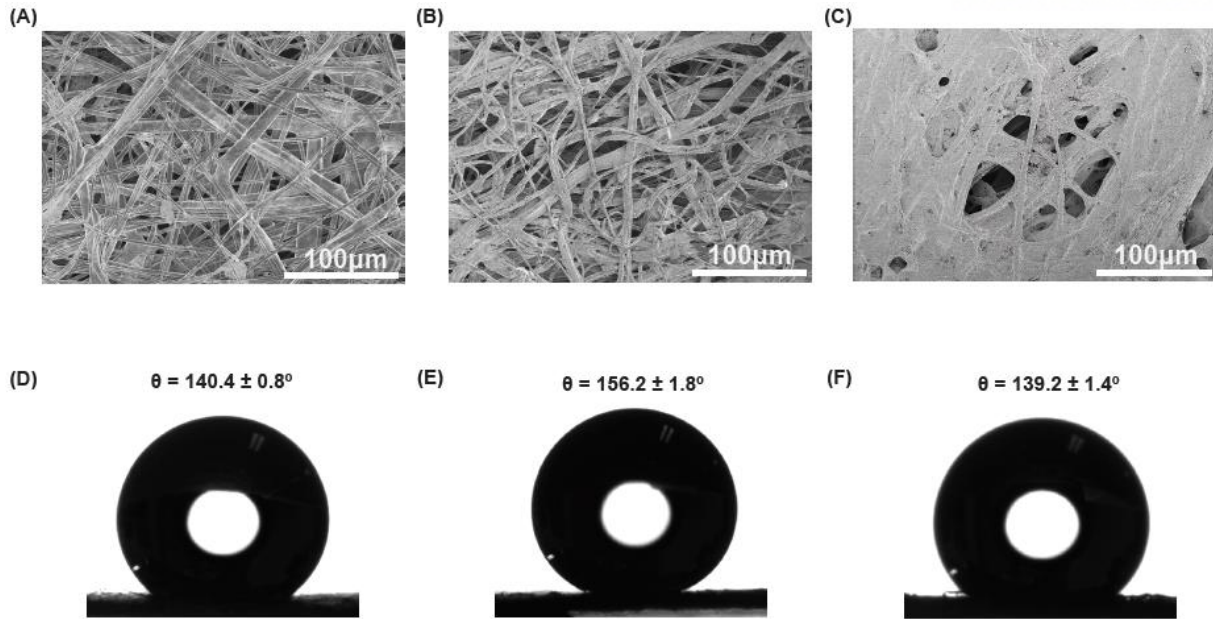
Figure 2.1: SEM images and contact angle data of different concentration of SWCNTs for coating mask (A) 1 mg per ml CNT concentration in benzene (B) 2.5 mg per ml CNT concentration in benzene (C) 5 mg per ml CNT concentration in benzene (D) Contact angle image of spray coated CNT mask with 1mg per ml CNT concentration in benzene (E) 2.5 mg per ml CNT concentration in benzene (F) 5 mg per ml CNT concentration in benzene. Reproduced with permission.[9] Copyright 2021, ACS.
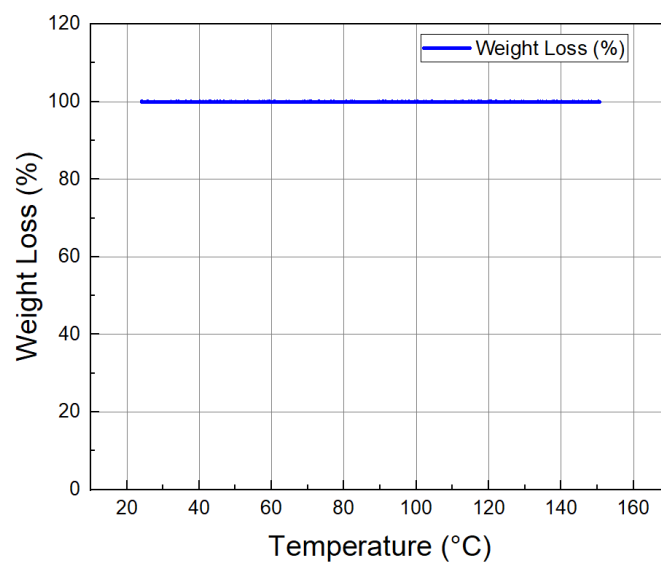
Figure 2.2: Thermo gravimetric analysis (TGA) of SWCNTs coated PP fiber sample.

Reproduced with permission.[9] Copyright 2021, ACS.

As we have mentioned that heat treatment helps to remove the benzene from the mask surface completely to prove out point, we also performed thermo gravimetric analysis (TGA) (TA Instruments Q-600, USA) of SWCNTs coated PP fiber sample. TGA graph of sample heated at 80 °C in nitrogen reveals no weight loss till 150 °C, which implies successful removal of all the benzene molecules (Figure 2.2).
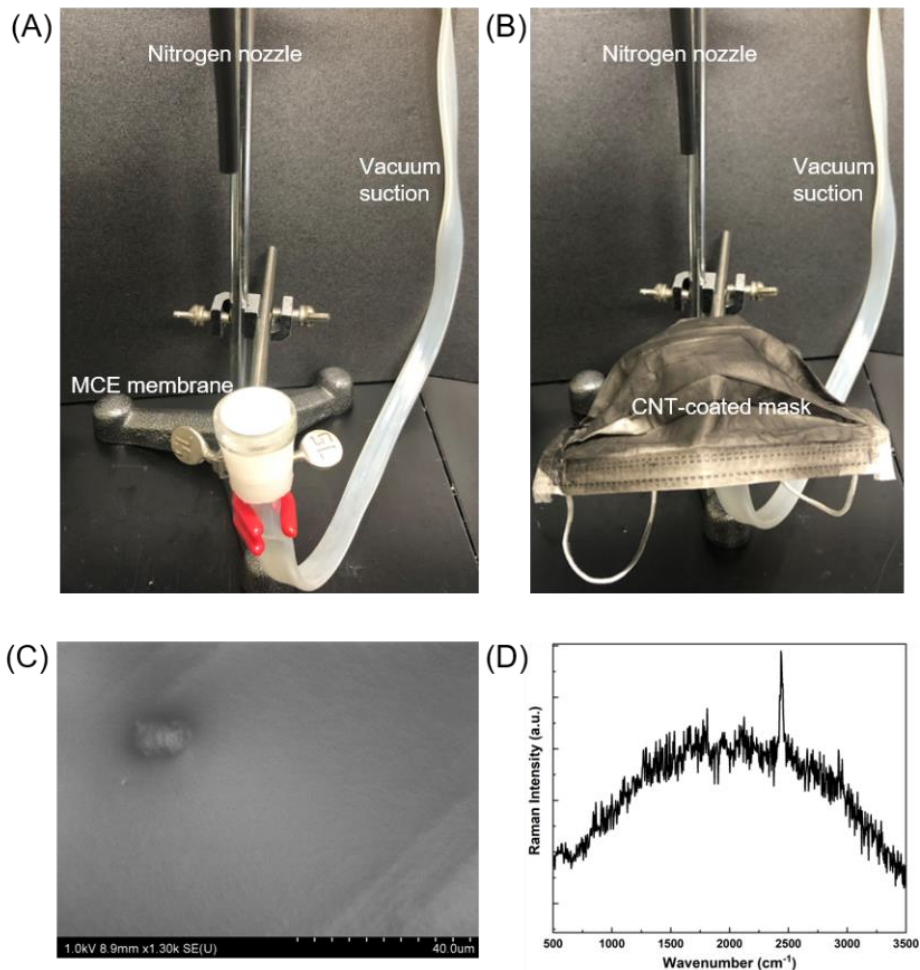
Figure 2.3: SEM analysis of SWCNTs PP attachment. (A) Optical image of experimental setup with MCE membrane (B) Optical image of experimental setup with MCE membrane and

CNT-coated mask (C) SEM image of MCE membrane after experiment (D) Raman spectra of MCE membrane after experiment. Reproduced with permission.[9] Copyright 2021, ACS.

We also performed an experiment to test whether the nanotubes are detached from the mask by a gas flow as shown in Figure 2.3. In this experiment, a CNT-coated mask was placed on a mixed cellulose esters (MCE) membrane with average pore size of 25 nm, and the mask was blown with high-pressure nitrogen gas for 1 hr while applying a vacuum suction to the MCE membrane to collect any CNTs detached from the mask. We did not find any CNTs on the membrane, by SEM inspection and Raman spectroscopy.

2.2.3 Characterization: The surface morphology of the samples was examined with a scanning electron microscope (Cold FE-SEM S-4800, Hitachi High Technologies Ltd., Japan) at 1 kV voltage and 7 µA current. The Raman spectra were recorded (ALPHA300R, WITEC, Germany) on a ultrahigh-throughput spectrometer (UHTS) over the scanning range of 100–3500 cm^{-1}. FT-IR spectroscopy (Varian, Agilent Technologies, Germany) was performed over the scanning range of 700–4000 cm^{-1} to investigate the distribution of oxygen functional groups on the samples. XPS was performed on a K-Alpha XPS system (Thermo Fisher Scientific, UK) equipped with double focusing hemispherical analyzer and monochromatic Al-$K\alpha$ source (1486.6 eV). The narrow-scan spectra were acquired in a constant analyzer energy mode with pass energy of 25 eV. Sample charging was compensated for the system flood gun, which emits low-energy electrons. The vacuum of the main chamber was maintained at 1×10^{-9} mbar during the entire measurement. The Thermo Scientific Avantage software was used for the digital acquisition and processing of data. Spectral calibration was performed by the automated calibration routine, using the internal Au, Ag, and Cu standards supplied with the K-Alpha system. The chemical characteristics of the samples were determined by deconvoluting the high-resolution XPS profiles using the XPS Peak fit 4.1 software. Diffuse

reflectance spectra of the pure and CNT-coated melt-blown PP fibers were recorded at room temperature in the range of 200–800 nm on a UV–vis spectrophotometer (Agilent Technologies Cary 5000, USA) equipped with an integrating sphere. A $BaSO_4$ pellet was used as the reference.

2.2.4 Contact Angle Measurements: To examine the wetting properties of the samples, images of sessile water drops were acquired with a Ramé-hart instrument and analyzed with the DROPimage Advanced version software. For the static contact angle measurements, 5 μL droplets of deionized water (18.2 MΩ cm) were used. For the contact angle measurements with body fluids (water, blood, sweat, tear, saliva, and urine), 10 μL droplets of the fluids were used. The contact angle on each type of surface was measured after 15 s following the casting of the drop to ensure that the droplet had reached its equilibrium position, and the values measured from different locations on the sample surface were averaged. . This blood related study was reviewed and approved by the Institutional Review Board of Ulsan National Institute of Science and Technology (UNISTIRB-19-38-C), Republic of Korea.

2.2.5 Photothermal measurements: a solar simulator (Model 10500, ABET Technologies, USA) was used as the sunlight source (1 sun intensity) at a distance of ~12 cm from the sample. The surface temperatures of the samples were measured with two Fluke TiS55 and FLIR Infrared cameras.

2.2.6 Electrothermal measurements: a DC power supply (Model N5769A, Keysight Technologies, USA) was used as the power source at a distance of ~ 10 mm on the specimen. The surface temperature of the specimens was measured using data acquisition (Model DAQ970A, Keysight Technologies, USA) and IR camera (FLIR Infrared Cameras, USA).

2.2.7 Differential pressure measurements: The differential pressure was determined using a customized experimental setup that includes a Data Acquisition (DAQ), pressure transducers, gas mass flow controllers (0-5 L min^{-1}) and a test filter assembly. The test filter assembly consists of a pipe screw setup in which the samples (10 mm diameter) were placed between the two O-rings and sealed tightly to prevent any leakage. Then, compressed air was flown at a constant rate (0–5 L min^{-1}), which is similar to that experienced during human respiration, accounting for the smaller sample cross-sectional area compared to that of a full face mask. The air flow rate was measured using a mass flow meter (SFM3300; Sensirion AG, Switzerland) and the pressure drop was measured using a Sensys Korea pressure transducer (PTBH ± 100RGPA-FC) and a DAQ system (Agilent, Keysight Technologies-34970A).

2.2.8 Analysis of the antimicrobial activity: The antibacterial effect of the CNT-coated mask was determined using *E. coli*. *E. coli* ATCC 25922 from a stock was streaked onto a Luria-Bertani (LB) agar plate (Difco Generic LABWARE, Beckton Dickinson, Seoul, Republic of Korea) and incubated at 37 °C with 5% CO_2. The isolated colony that appeared after 18 h of incubation was inoculated in 10 mL of the Luria Broth (LB) medium and incubated at 37 °C and 150 rpm until the logarithmic phase was achieved with a concentration in the range of 1.0×10^8 to 1.0×10^9 CFU mL^{-1} (CFU: colony forming unit). Approximately 100 μL of the bacterial suspension (1×10^9 CFU mL^{-1}) was placed on the outer surface of the CNT-coated mask and was treated with solar irradiation (1 sun intensity, 1 min). After the treatment, the bacterial solution on the CNT-coated mask surface was serially diluted by 10^1-10^6 folds in sterile PBS and cultured on an LB agar plate. The cultured plate was incubated at 37 °C with 5% CO_2 for 18 h. The experiment was performed in triplicate.

2.2.9 Live dead assay: The bacteria which was treated in the dark and light mode was determined by live dead assay. Bacteria was collected from the respective mask after treating

26

in the light and dark mode. SYTO9 and propidium iodide were mixed in equal volume and 3 µL of the mixture was added in the bacterial solution. It was incubated in dark at room temperature for 15 min. The cell was imaged in the confocal microscopy at excitation/ emission of SYTO9 (485/498) and Propidium iodide (490/635).

2.2.10 Cell culture: A T75 cell culture flask (Corning, NY, USA) was used to culture 5×10^6 cells in 18 mL of a Roswell Park Memorial Institute medium (RPMI, Gibco, Thermo Fisher Scientific) supplemented with 10% fetal bovine serum (FBS; Systems Biosciences Inc, CA, USA)), and 1% antibiotics/antimycotics (100 U mL^{-1} penicillin and 100 mg mL^{-1} streptomycin) and incubated at 37 °C in 5% CO_2 for the isolation of the VPs until the confluency reached 60–70%. After the confluent growth, the cell was washed with $1\times$ PBS. Then, the cell was replaced with the RPMI medium, supplemented with 10% exo-free FBS (and 1% antibiotics/antimycotics (100 U mL^{-1} penicillin and 100 mg mL^{-1} streptomycin) and incubated for 48 h at 37 °C in 5% CO_2. The cell culture supernatant (CCS) was collected for the isolation of the exosomes by the ultracentrifugation method.

2.2.11 Ultracentrifugation method: The collected CCS was centrifuged at 300 g for 10 min to remove the cellular debris. The supernatant obtained after the removal of the debris was further centrifuged at 2000 g for 20 min. The resultant supernatant was centrifuged at 20,000 g for 1 h at 4 °C using 50 mL Nalgene polypropylene high-speed centrifuge tubes. Then, the supernatant was transferred to new ultracentrifuge tubes and centrifuged at 120,000 g for 2 h at 4 °C in a Ti45 fixed angle rotor (Beckman Coulter). The supernatant was discarded, and the exosome pellet was collected and resuspended in 1 mL of prefiltered PBS, and then transferred to 1.2 mL polycarbonate ultracentrifuge tubes. It was then centrifuged at 120,000 g at 4 °C for 2 h in an MLA-130 fixed angle rotor (Beckman Coulter). Thereafter, the pellet was resuspended in prefiltered PBS (filter pore size: 200 nm) and stored either at 4 °C for immediate

use or at −80 °C for further use. Bicinchoninic acid assay (BCA) was performed for the characterization of the exosomes (see Figure 2.16).

2.2.12 Nanoparticle tracking analysis: To count the number of exosomes and determine their size distribution, NTA was performed. The exosomes were diluted in a particle-free PBS (filter pore size: 0.02 µm), and ~0.6 mL of the exosome suspension was loaded in the sample chamber of the NTA system (Malvern Analytical NanoSight N500 Instrument) equipped with a 405 nm laser. The number of particles per video was maintained between 100 and 2000. Videos of 30 s duration were recorded by adjusting the camera level to 14 and detection threshold to 7. NTA 2.1 software (NanoSight) on the automatic mode for camera focus, shutter, blur, minimum track length, minimum expected size, and maximum jump length was used for the data analysis.

2.2.13 SDS-PAGE gel electrophoresis: VPs pellet was lysed in RIPA buffer with a protease inhibitor. The VPs lysate was mixed with the nonreducing loading buffer buffer (Cell Biolabs, CA, USA) and were boiled for 15 min at 95 °C. Then, they were loaded on a 10% SDS-PAGE gel (Pierce, Rockford, IL, USA) in the Mini-Protean TGX electrophoresis apparatus (Bio-rad, CA, USA) that contains the running buffer to separate the lysates. After the completion of electrophoresis, the gel was stained with Coomassie stain to verify the protein band.

2.3 Results and Discussion:

2.3.1 Surface Modification of Surgical Masks using SWCNTs

One of the primary reasons for wearing a mask is to reduce the risk of inhaling the virus- or bacteria-containing respiratory droplets. The outer surface of the mask needs to be hydrophobic to repel those droplets, but the hydrophobicity of the currently used masks is either insufficient or temporary. Herein, we employ spray-coating of SWCNTs as a convenient and scalable method to improve the hydrophobicity of melt-blown PP filters that are commonly used in the

commercially available surgical masks. Figure 2.5A presents the schematic of our single-step

spray-coating method. SWCNTs dispersed in benzene (Figures 2.4) were sprayed onto a

commercially available surgical mask, followed by drying the coated mask in the oven. The

(A)　　　θ = 115.4 ± 2.4°　　　(B)　　　θ = 119.2 ± 0.8°　　　(C)　　　θ = 121.5 ± 1.2°

(D)　　　θ = 135.4 ± 0.2°　　　(E)　　　θ = 138.9 ± 2.4°　　　(F)　　　θ = 156.2 ± 1.8°
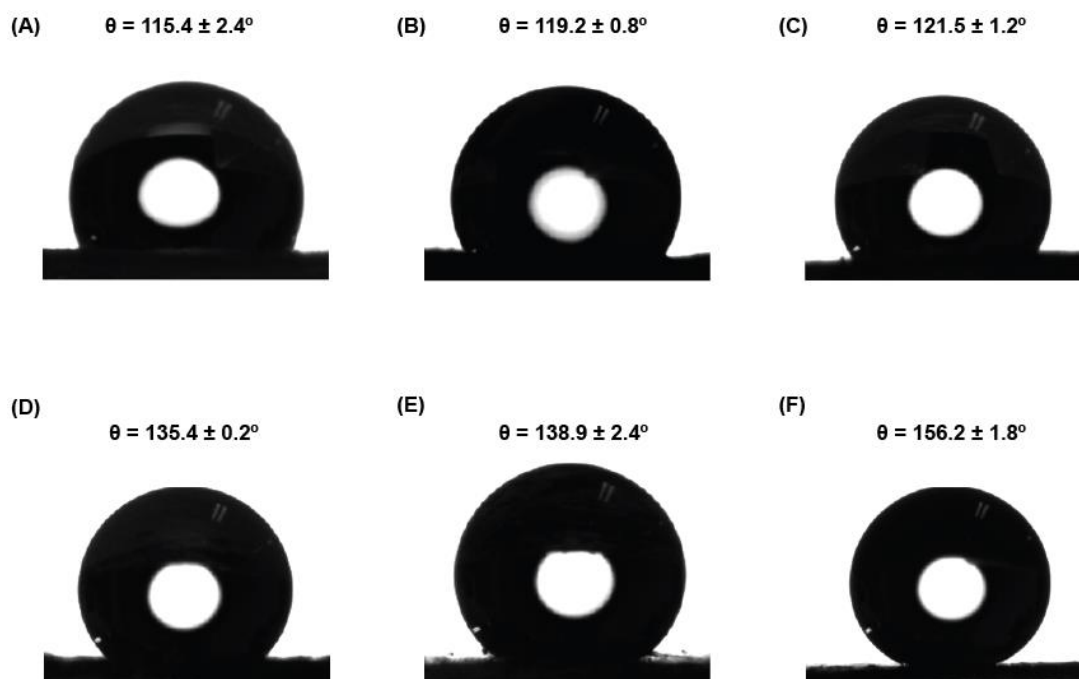
Figure 2.4: Contact angle data for different types of solvents used to spray coating on mask. (A) Pristine mask contact angle (B) Dichlorobenzene and CNT dispersion for CNT-coated mask contact angle (C) Toluene and CNT dispersion for CNT-coated mask contact angle (D) Acetone and CNT dispersion for CNT-coated mask contact angle (E) IPA and CNT dispersion for CNT-coated mask contact angle (F) Benzene and CNT dispersion for CNT-coated mask contact angle. Reproduced with permission.[9] Copyright 2021, ACS.

coated mask was bath-sonicated in benzene to remove excess SWCNTs not directly bound to

the PP fiber. The mask was then placed in the oven again to remove benzene. Here, the last

two steps, bath-sonication and heat treatment, reduce the risk of inhaling SWCNTs and

benzene, respectively while breathing and are thus critical in this approach. Thermogravimetric

analysis (TGA) of the CNT-coated PP fibers showed no weight loss (Figure 2.2), and we did

not find any evidence of CNTs detached from the mask even under a high-pressure nitrogen stream (Figure 2.3). These results do not prove but strongly support complete removal of benzene as well as the absence of CNTs detached by breathing. Figure 2.5B shows the mask before (left) and after (right) being spray-coated with the SWCNTs, with the corresponding scanning electron microscopy (SEM) images of the PP fibers shown below.
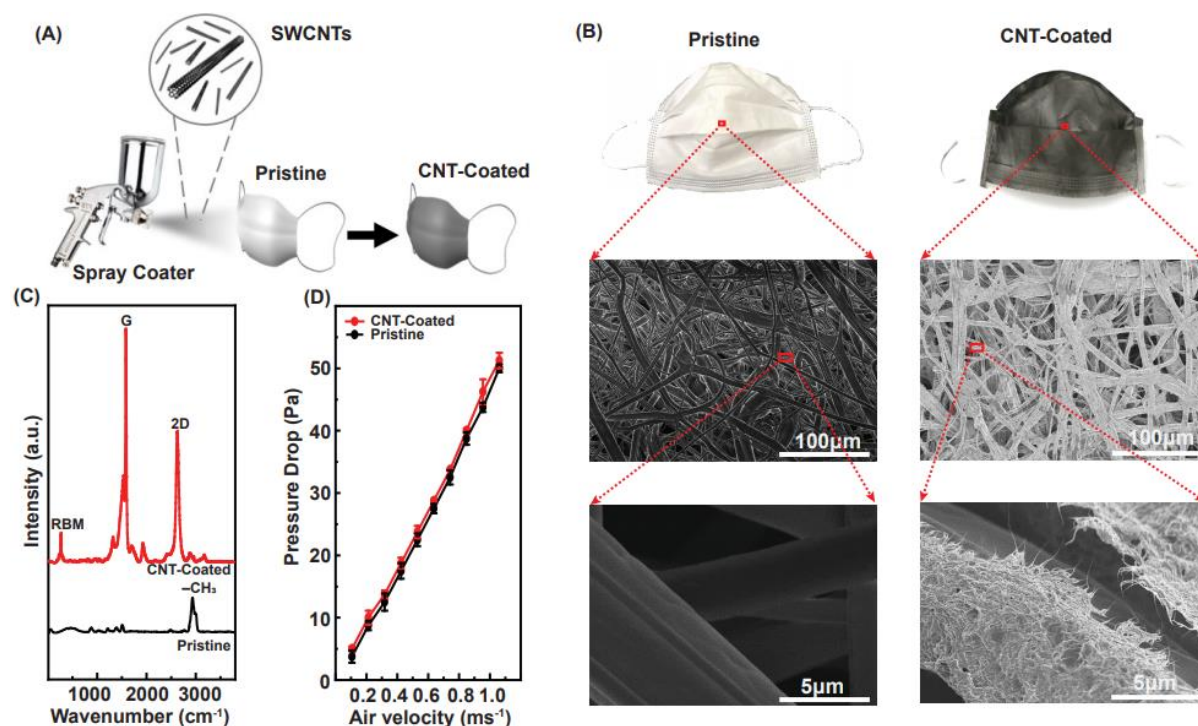
Figure 2.5: Surface modification of surgical masks using SWCNTs. (A) Schematic representation of the spray-coating of SWCNTs on the nonwoven fibers of a pristine mask. (B) Optical images of the pristine (left) and the CNT-coated (right) masks, along with their low- and high-magnification SEM images (shown below). (C) Raman spectra of the pristine (black curve) and the CNT-coated (red curve) masks. (D) Pressure drop vs. Air velocity for the pristine (black curve) and the CNT-coated (red curve) masks. Reproduced with permission.[9] Copyright 2021, ACS.

2.3.2   Chemical Characterization of the Coating on a Pristine Surgical Mask

The mask turned black after the coating, and the PP fibers with an initially smooth surface were completely covered with spiky nanostructures, which were confirmed to be bundles of SWCNTs based on the characteristic tangential (G, 1500–1600 cm^{-1}) and radial breathing modes (RBM, 160–300 cm^{-1}) of SWCNTs in the Raman spectrum (Figure 2.5C) as well as other spectroscopic measurements (Figure 2.6). Because the reduced porosity of the coated nanotubes may affect breathing, we measured the pressure drop across the pristine and CNT-coated masks over a range of air velocity (0–1.06 ms^{-1}; Figure 2.5D) using a custom-built setup (Figure 2.7). The breathability, as obtained from the slope of the graph, was almost identical in both samples: 21.92 mm s^{-1} Pa^{-1} for the pristine mask and 21.91 mm s^{-1} Pa^{-1} for the CNT-coated one. Compared to dip coating, the spray-coating methodology enables deposition of uniform and conformal coating of the SWCNTs (Figure 2.8) even on a large scale (Figure 2.9).
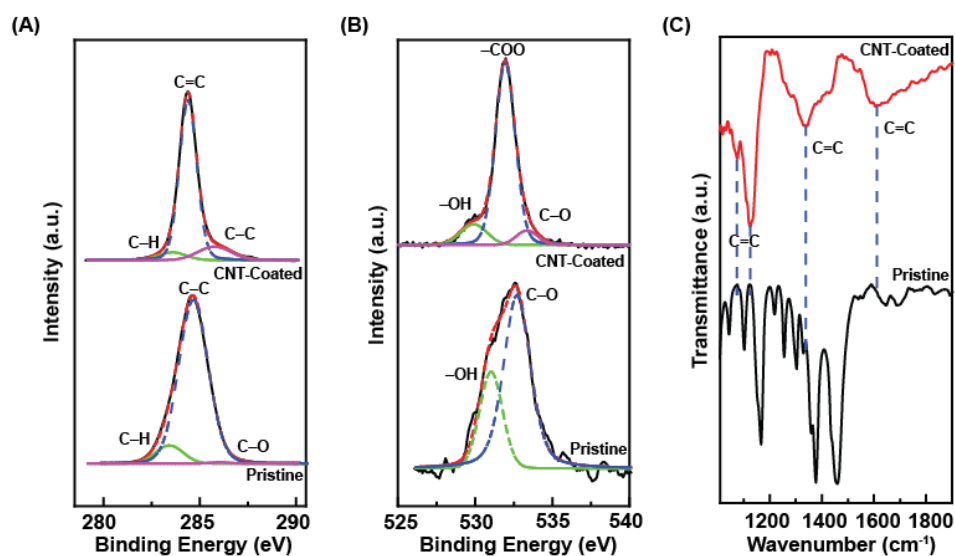
Figure 2.6: Chemical characterization of the coating on a pristine surgical mask. (A) High resolution C-1s XPS data of pristine and CNT-coated mask (B) High resolution O-1s XPS data of pristine and CNT-coated mask (C) Characterization of chemical composition using FT-IR spectroscopy of pristine and CNT-coated mask. The presence of CNTs is confirmed by the peaks labeled as C=C. Reproduced with permission.[9] Copyright 2021, ACS.
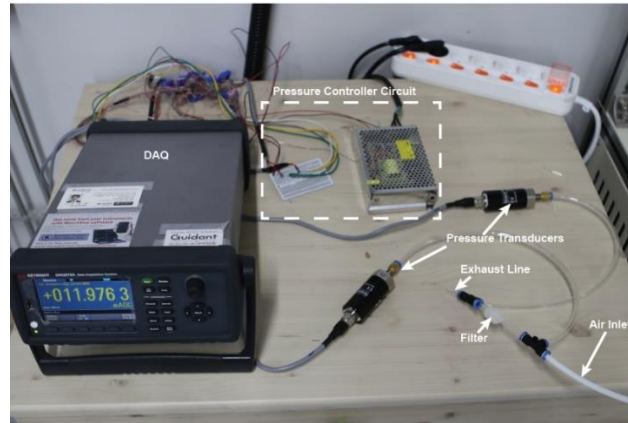
Figure 2.7: Digital photograph of air permeability setup. Reproduced with permission.[9]

Copyright 2021, ACS.
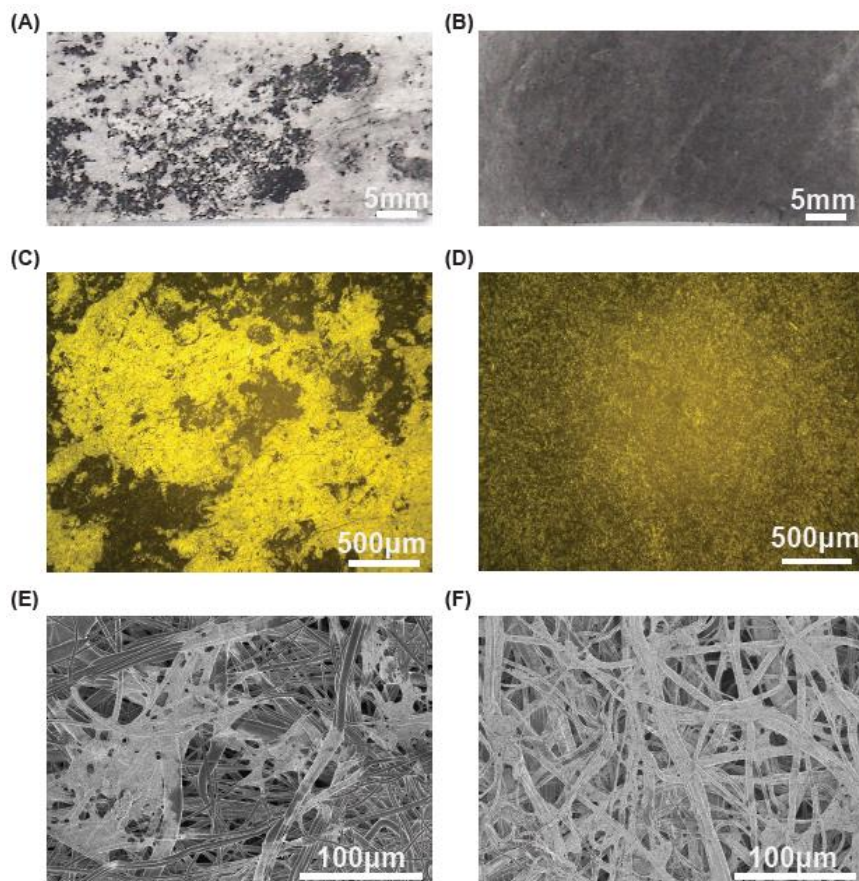
Figure 2.8: Different types of coating methods for mask. (A) Optical photograph of dip coated CNT mask (B) Optical photograph of Spray coated CNT mask (C) Bright filed image

of dip coated CNT mask (D) Bright filed image of spray coated CNT mask (E) SEM image of

dip coated CNT mask (F) SEM image of spray coated CNT mask. Reproduced with

permission.[9] Copyright 2021, ACS.

2.3.3 Wetting Behaviors of the SWCNTs Coating on a Pristine Surgical Mask

To understand the interaction of the mask with respiratory droplets, the hydrophobicity of the
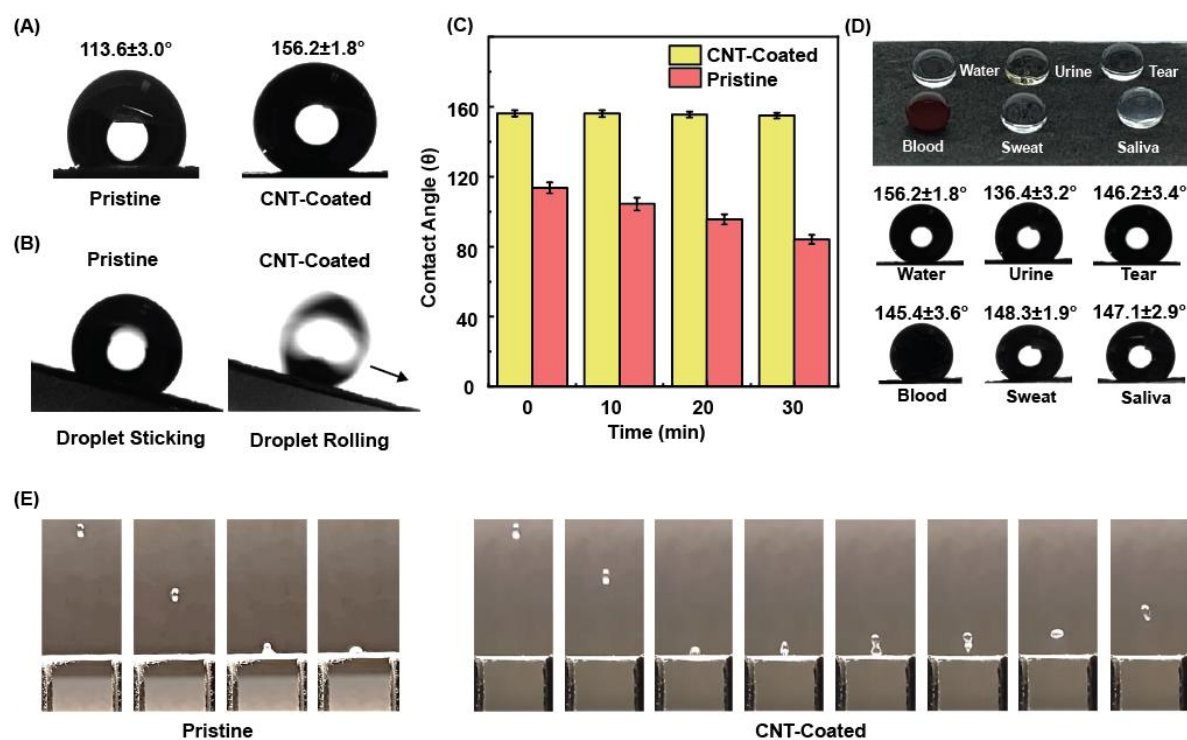
Figure 2.10: Wetting behaviors of the SWCNTs coating on a pristine surgical mask (A)
Contact angles on the pristine mask (left) and the CNT-coated mask (right). (B) Water droplet
stuck on the tilted pristine mask (left) and rolling off the tilted CNT-coated mask (right). (C)
Time-dependent variation in the contact angle of a water droplet on the pristine mask and the
CNT-coated mask. (D) Droplets of body fluids on the surface of CNT-coated masks and the
contact angle values for each fluid. (E) Time-lapse images of a water droplet falling onto a
pristine mask (left) and the CNT-coated mask (right), showing the droplet bouncing off the
latter. Reproduced with permission.[9] Copyright 2021, ACS.
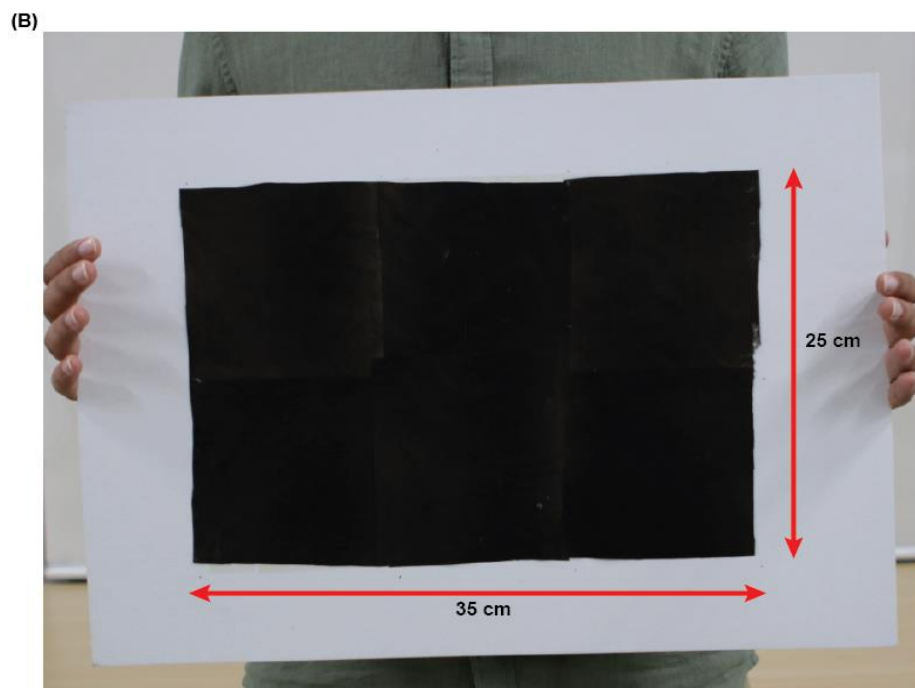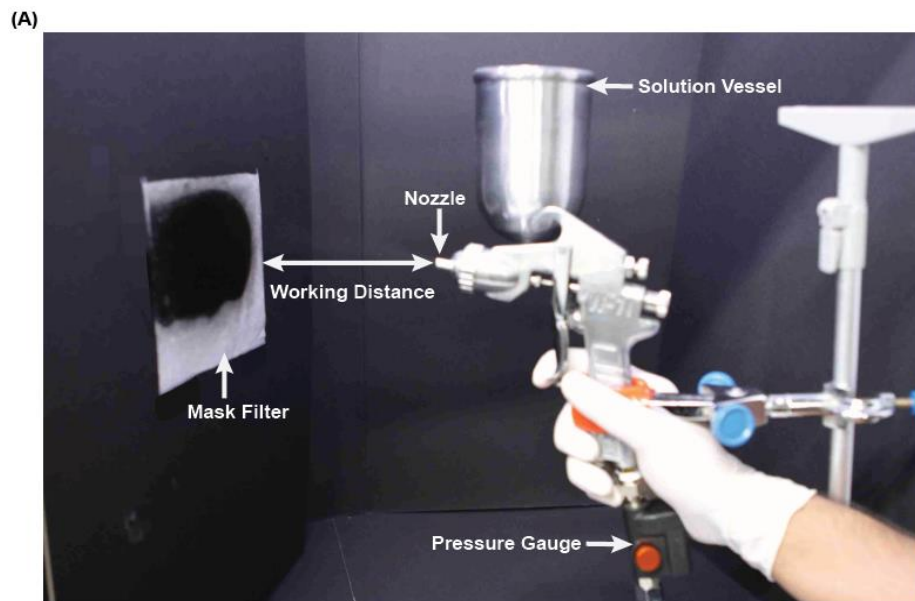
Figure 2.9: Demonstration of spray coating. (A) Digital photograph of spray coating setup

(B) Spray coating demonstration on large scale pristine mask nonwoven fiber area. Reproduced

with permission.[9] Copyright 2021, ACS.

roughness.[53, 62, 69] The rolling behavior of the water droplets was investigated by tilting the mask to validate the superhydrophobicity of the CNT-coated mask (Figure 2.10B). A 10 µL water droplet on the pristine mask did not move when the mask was tilted or even inverted, whereas on the CNT- coated mask the droplet rolled-off instantly at a sliding angle of 14°

pristine and the CNT-coated masks were examined in detail. The pristine mask showed a static water contact angle of $113.6° \pm 3.0°$, but the contact angle increased to $156.2° \pm 1.8°$ for the CNT-coated mask (Figure 2.10A). The superhydrophobicity of the CNT-coated mask is attributed to the spiky nanostructures of hydrophobic CNTs that increase the surface Furthermore, the contact angle of the water droplet on the CNT-coated mask was retained for 30 min, while that on the pristine mask decreased by more than 35% after the same time (Figure 2.10C). These results validate the robust superhydrophobicity of the CNT-coated masks, which is important for providing protection from respiratory droplets for an extended period of time. Since the transmission of virus or bacteria occurs mainly by contact with body fluids,[70-73] we measured the static contact angles of several body fluids such as blood, sweat, urine, tears, and saliva on the pristine and CNT-coated masks, as shown in Figures 2.10D and 2.11. As compared to the pristine mask, the SWCNT-coated surface displayed outstanding repellency against the tested body fluids, causing the water droplet to bounce off the surface (Figure 2.10E). Furthermore, to imitate respiratory droplets generated by sneezing or coughing, which are primary reasons for the transmission of the virus, a water jet containing small water droplets was sprayed on a human dummy wearing the mask. The water droplets fell immediately down from the CNT-coated mask, suggesting its self-cleaning property, whereas the droplets adhered on the pristine mask.

2.3.4   Photothermal Performance of the Masks

SWCNTs are known to exhibit strong photothermal effect as demonstrated in previous studies

on photothermal ablation of cancer cells and tumors.[74-76] Therefore, we investigated whether
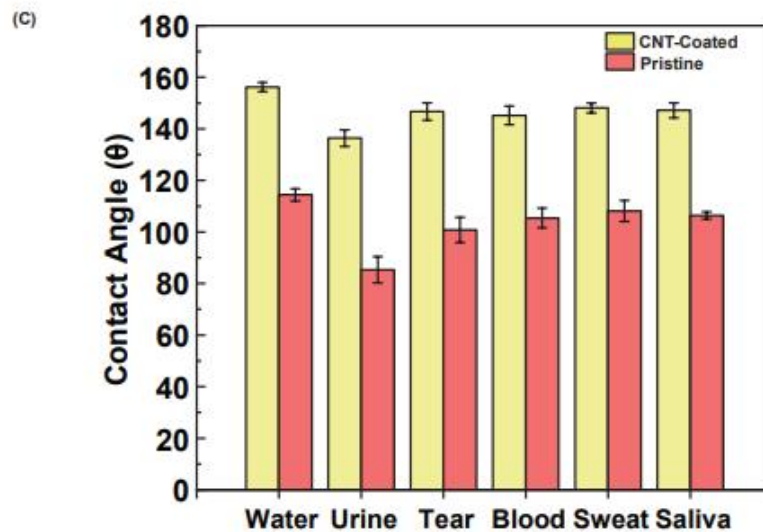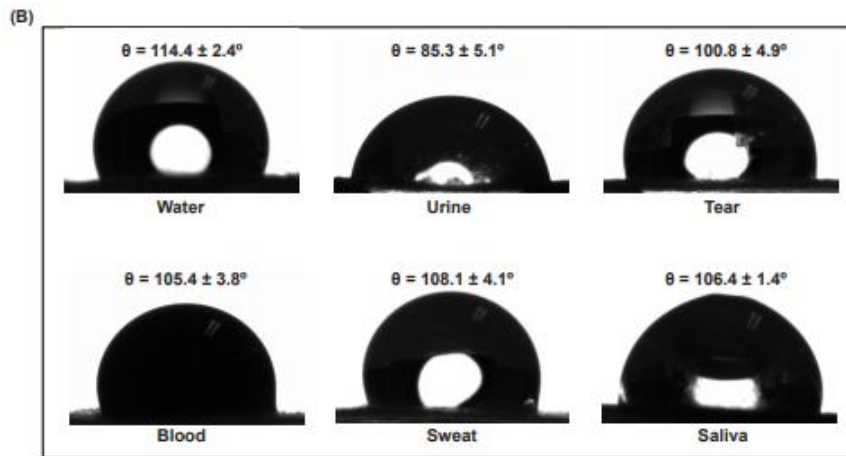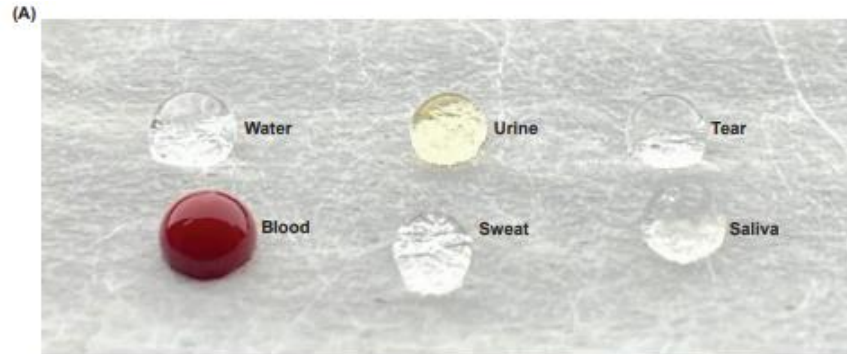
Figure 2.11: Wetting behaviors for body fluids on a pristine surgical mask. (A) Body fluid on surface of pristine mask (B) contact angle data for body fluids (C) Body fluids comparison data for pristine and CNT-coated mask. Reproduced with permission.[9] Copyright 2021, ACS.

the photothermal property of CNTs can be utilized to kill the viruses and bacteria that are not completely repelled by the superhydrophobic surface. The CNT-coated mask was placed under a solar simulator and illuminated at 1 sun intensity while imaging the mask temperature with an infrared (IR) camera as illustrated in Figure 2.12A. Upon illumination, the surface temperature of the CNT-coated mask increased rapidly to 90 °C within 30 s (Figure 2.12B). A similar result was obtained from a human dummy wearing the CNT-coated mask, as shown in Figure 2.12C**.**
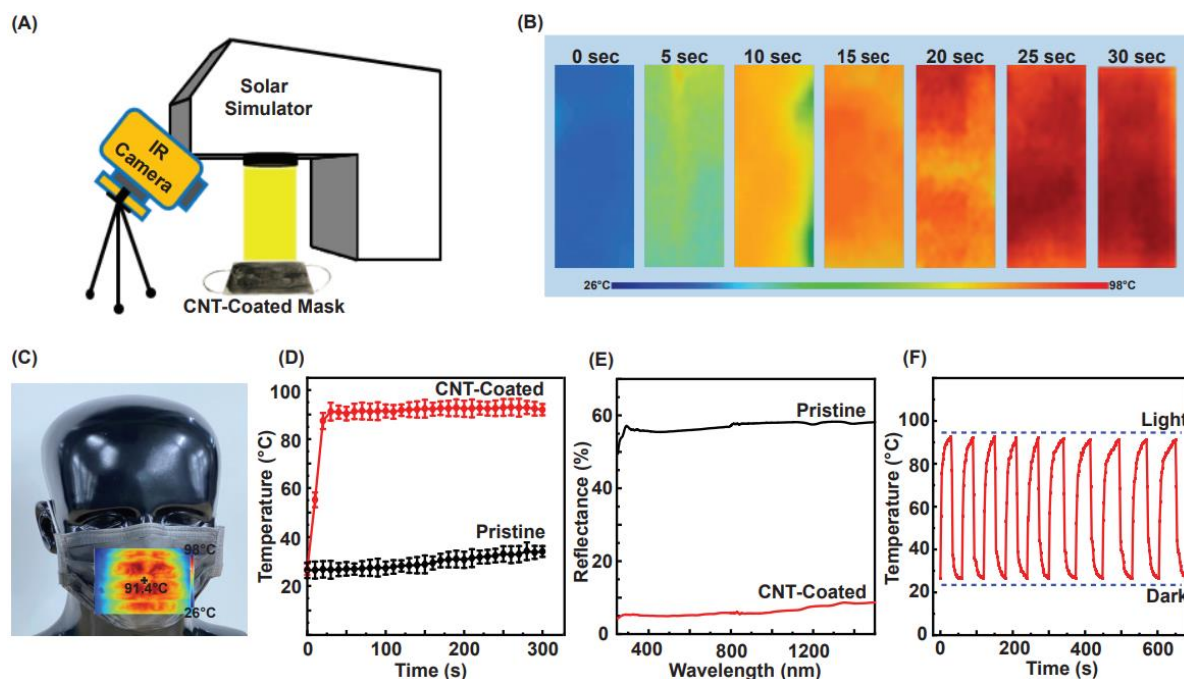
Figure 2.12: Photothermal performance of the masks (A) Schematic of the setup used for photothermal studies. (B) Time-lapse thermal images of the CNT-coated mask. (C) Human dummy wearing a CNT-coated mask showing the temperature increase at 1 sun intensity. (D) Surface temperature measured by an IR camera against time for the pristine (black curve) and

the CNT-coated (red curve) masks. (E) Reflectance spectra of the pristine (black curve) and the CNT-coated (red curve) masks. (F) Temperature of the CNT-coated mask under multiple on/off cycles of 1 sun illumination. Reproduced with permission.[9] Copyright 2021, ACS.

Figure 2.13: Solar illumination effects on CNT-coated mask surface. (A) Optical photograph of solar simulator setup (B) Contact angles measured after 10 cycles under solar

illumination (C) SEM image of CNT-coated poly propylene fibers of the mask before solar illumination (D) SEM image of CNT-coated poly propylene fibers of the mask after 10 cycles of solar illumination (E) Human wearing CNT-coated mask IR image under direct sun light at around 9 AM (F) Human wearing CNT-coated mask IR image under direct sun light at around 12 PM (G) Human wearing CNT-coated mask IR image under direct sun light at around 3 PM (H) IR image of CNT-coated mask back side under direct sun light at around 12 PM (I) IR image of CNT-coated mask kept on ground under direct sun light at around 12 PM (J) Human wearing pristine mask IR image under direct sun light at around 12 PM. Reproduced with permission.[9] Copyright 2021, ACS.

In contrast, the temperature of pristine mask remained below 40 °C even after 5 min of solar illumination (Figure 2.12D). The photothermal effect benefited from the high absorption of light as confirmed by the reflectance spectrum (Figure 2.12E). Furthermore, the photothermal effect of the CNT-coated mask displayed excellent stability and reproducibility during 10 illumination cycles (Figure 2.12F). We also confirmed that both the superhydrophobicity and the surface microstructure of the mask were preserved after the illumination cycles (Figure 2.13).

For practical applications, it is important to test the photothermal activity of the CNT-coated mask and the risk of skin burn while wearing it in the sun. The temperature of the outer surface of the mask was monitored at 9 AM, 12 PM, and 3 PM while it was worn on a sunny day (Figure 2.13). We found that the outer temperature while wearing did not exceed 45.1 °C even at 12 PM when the intensity of the sun was at its maximum. The temperature on the backside of the mask contacting the skin was around 37 °C, which confirms that there is no risk of skin burn. However, when the mask was removed and placed directly under sunlight for ~1 min,
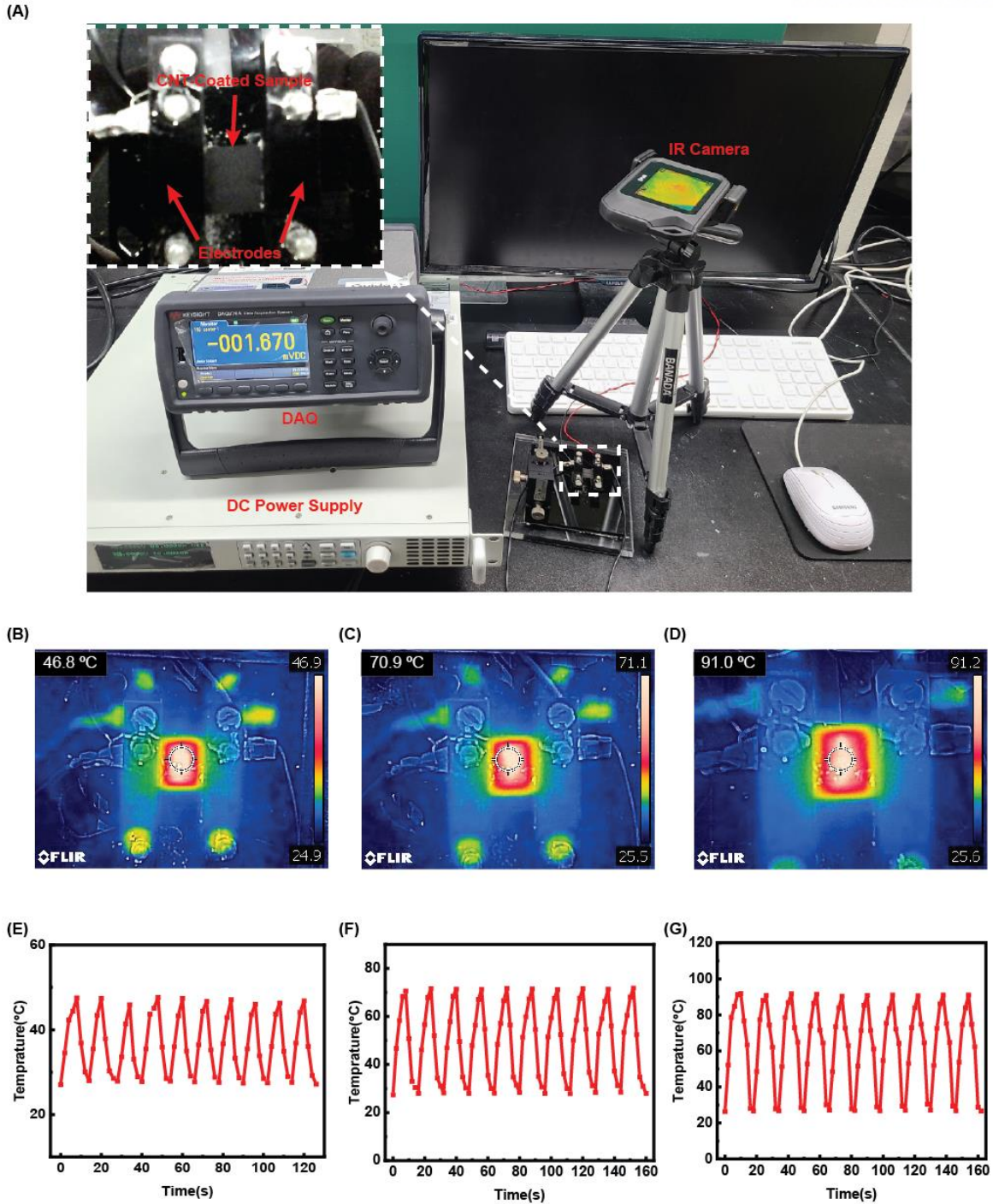
Figure 2.14: Electrothermal effect on CNT-coated mask surface. (A) Optical photograph of electrothermal setup (B) IR image of CNT-coated mask sample at 10 volts (C) IR image of CNT-coated mask sample at 20 volts (D) IR image of CNT-coated mask sample at 30 volts (E) On/Off response for CNT-coated mask at 10 volts (F) On/Off response for CNT-coated mask

at 20 volts (G) On/Off response for CNT-coated mask at 30 volts. Reproduced with permission.[9] Copyright 2021, ACS.

the temperature of the SWCNT-coated mask reached 60.9 °C, which is a sufficiently high temperature for deactivation of the SARS-CoV virus.[77-79] In contrast, the temperature of the pristine mask did not increase beyond 28.6 °C even after 5 min of exposure. Therefore, it can be concluded that the SWCNT-coated mask enables photothermal sterilization with safety and convenience. Additional sterilization may be achieved by resistive heating or electrothermal process, when the density of CNTs is high enough to form an electrically conductive layer (Figure 2.14), at the expense of reduced air permeability.

2.3.5 Antimicrobial and Antiviral Properties of Masks

We evaluated the antimicrobial activity of the CNT-coated mask facilitated by the outstanding photothermal response by counting the colony-forming units (CFUs). Figure 2.15A shows the *E. coli* ATCC 25922 present on the pristine mask and CNT-coated mask under dark (no sun

Figure 2.15: Antimicrobial and antiviral properties. (**A**) Detection of the antibacterial effect (CFU mL^{-1}) of the *E. coli* ATCC 25922 bacteria on the pristine and the CNT-coated masks under dark and light conditions. (**B**) High-resolution confocal fluorescence microscopy images of the live/dead assay of *E. coli* ATCC 25922 stained with SYTO 9 and propidium iodide. (**C**) Number of viable *E. coli* bacteria calculated from CFUs after solar illumination of the surfaces of the control (glass surface), pristine, and CNT-coated masks. Data are expressed as mean ± standard deviation values; n = 3 independent experiments. (**D**) Changes in the concentration of the VPs on the control, pristine, and CNT-coated masks under dark and light conditions. (**E**) Representative SDS-PAGE electrophoresis data for the control, pristine, and CNT-coated masks after treatment of VPs under light mode. Reproduced with permission.[9] Copyright 2021, ACS.

illumination) and light (1 sun intensity for 1 min) modes. In the case of the pristine mask, there was no change in the bacterial population in either mode (dark or light mode), whereas an effective antimicrobial activity was observed in the light mode for the CNT-coated mask. The SYTO 9 (485/498 nm) and propidium iodide (535/617 nm) fluorescence-based live/dead assay of *E. coli* ATCC 25922 further confirmed the antimicrobial properties of the mask. The high-resolution confocal fluorescence images in Figure 2.15B show the viable bacteria in the dark mode (left) and light mode (right) after 1 min of solar illumination on the pristine (top) and the CNT-coated (bottom) masks. Under illumination, many bacteria were killed in the case of the CNT-coated mask as represented by the red color. Quantitative analysis based on CFUs showed significantly reduced bacterial viability in the case of the CNT-coated mask, with an impressive ~4 log (>99.99%) for *E. coli*, while the controls showed insignificant antibacterial effects (Figure 2.15C). These results indicate that the CNT-coated mask shows a remarkable self-sterilization property under solar illumination.

We also investigated the antiviral property of the CNT-coated mask using exosomes as virus-like particles (VPs). Exosomes are extracellular vesicles that closely resemble the virus in size and content. Both the SARS-CoV-2 virus (size: ~100 nm) and the exosomes contain genetic materials, proteins, and lipids from the host cells and have similar biogenesis pathways, and they are released from the infected cells after the fusion of multivesicular bodies with the plasma membrane.[80-82] Thus, this virus-like particles could be used on the surface of the CNT-coated mask to examine its self-sterilization property and thus its reusability or recyclability.[83] First, VPs derived from breast cancer MCF-7 cells were isolated by an ultracentrifugation method and characterized by nanoparticle tracking analysis (NTA) (Figure 2.16).
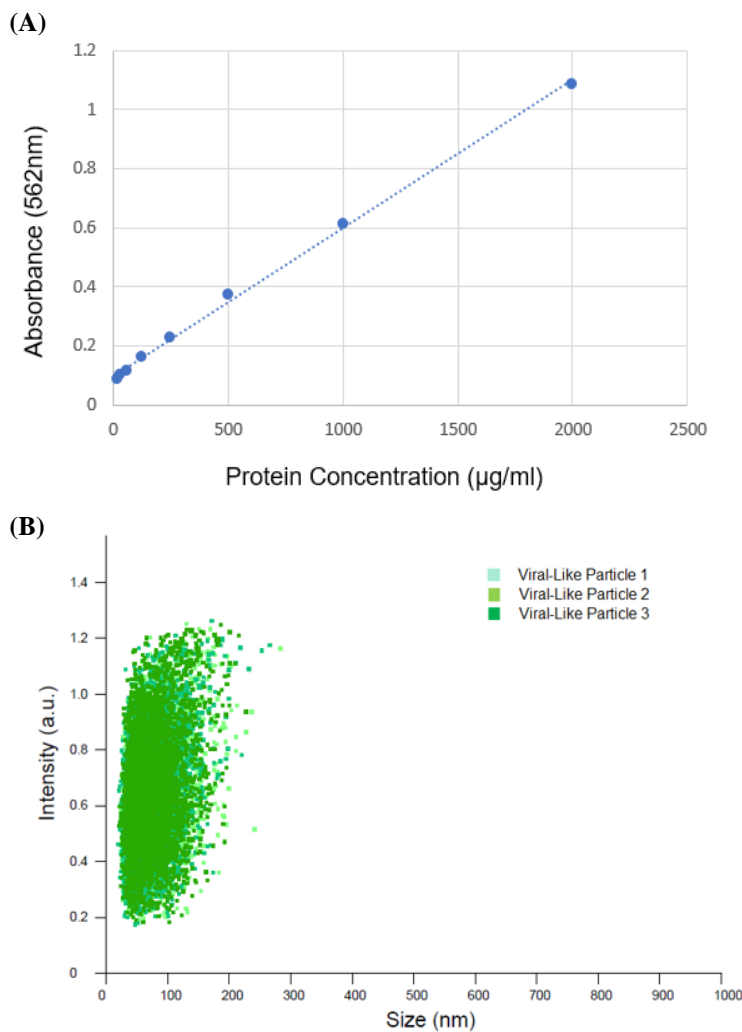
(A)

(B)

Figure 2.16: Characterization of virus-like particles (VPs). (A) Slope obtained from Bicinchoninic acid assay (BCA) of the standard protein to calculate the concentration of VPs **(B)** Size distribution of VPs. Reproduced with permission.[9] Copyright 2021, ACS.

We determined the virucidal efficiency of the CNT-coated mask and pristine mask by measuring the particle concentration (number of particles mL^{-1}) in the size range of 30 to 200 nm through NTA. Purified VPs (30 µL) were inoculated in a solution to obtain a concentration of ~10^8 particles mL^{-1} and illuminated at 1 sun intensity. As shown in Figure 2.15D, the loss of VPs on the CNT-coated mask was 99%, while the loss was not significant on the control glass surface and pristine mask. The SDS-PAGE gel electrophoresis data further confirmed the antiviral property of the CNT-coated mask (Figure 2.15E). After 1 sun illumination, the bands for proteins with molecular weight of ~53 and ~28 kDa (corresponding to CD63 and CD9, respectively) clearly showed the presence of VPs on the control and pristine mask, whereas no band was observed in the case of CNT-coated mask, suggesting removal of most of the VPs from the surface.

Chapter 3

Bio adhesive based superhydrophobic coating

Publications:

Bio-adhesive based nano-coating to make superhydrophobic and self-cleaning surfaces. Ritesh Soni, Saikat Sinha Ray, Chinna Bathula, Hyun-Seok Kim, Young-Nam Kwon and Chang Young Lee. (In preparation) 2023.

3.1 Introduction:

Real-life applications of these superhydrophobic surfaces are still encountering several challenges in terms of robustness, cost, complexity, uniformity, and durability.[84, 85] Various fabrication techniques have been utilized to create essential low surface energy and micro/nano-hierarchical roughness for artificial superhydrophobic surfaces.[86] Low surface energy polymers like epoxy resin,[87] polydimethylsiloxane (PDMS),[88] silicone,[89] and fluoroacrylic copolymers[90] have been used to make surface superhydrophobic but most of these polymers have limitation in terms of high cost, environment hazards, low biocompatibility, strength and stiffness.[91] To overcome these limitations we have used shellac, a natural hydrophobic [83] bio adhesive polymer secreted on various host tress by the insect named *Kerria lacca*. Shellac is a resinous material consisting of a complex mixture of polycarboxylic esters, polyhydroxy, lactones, and anhydrides. Shellac has been extensively utilized as an outstanding polymeric coating material due to its biocompatibility, low cost (~$2/kg), eco friendliness, and strong binding ability.[92, 93] For reducing the surface energy of silica nanoparticles, a well-known organosilane derivative named octadecyltricholosilane (OTS) has been applied which strongly binds and modifies SiO2 substrates. OTS is widely known for surface modification of numerous solid substrates by forming self-assembled monolayers (SAM).[94, 95]

In the current study, a facile, versatile, cost effective, ecofriendly, and durable bio-adhesive based superhydrophobic nanocoating was developed for creating self-cleaning surfaces for protection against acid rain and water-soluble organic pollutants. Protective treatment or coating for protection from acid rain is necessary because when building materials get exposed in an extreme environment then these materials show negligible decay resistance and can be

damage and degraded which shortens the services life and minimize the value. In this experiment, shellac and Octadecyltricholosilane (OTS) modified silica nanoparticles (SSO) based coating applied on multiple substrates like polypropylene (PP), glass, polyethylene terephthalate (PET), cotton, wood, metal, and building material to obtain superhydrophobicity. These overall outputs indicate that SSO coating is eco-friendly, robust, uniform, fluorine-free, and versatile. It can be applied by using various coating methods like spray, dip, painting, and sonication methods as well. To the best of our knowledge, the combination of shellac, silica nanoparticles, and OTS has not been explored before. The average contact angle, sliding angle, and contact angle hysteresis were reported to understand wetting behavior of the SSO-coated substrates. Durability of the SSO-coated substrates was examined by performing abrasion test under aggressive mechanical conditions. This study demonstrates a facile and potential approach for producing multiple superhydrophobic substrates. This SSO coating can be potentially used as a fundamental study for generating superhydrophobic surfaces to protect against acid rain and organic pollutants.

3.2 Materials and Methods:

3.2.1 Materials

Shellac flakes were purchased from Shellac Shack, USA. Octadecyltricholosilane (OTS) and ammonium hydroxide (NH$_4$OH) was acquired from Alfa Aesar, South Korea. Tetraethyl orthosilicate (TEOS) and ethanol was obtained from Sigma, South Korea respectively and have been used with no additional purification.

3.2.2 Preparation of Silica Nanoparticles

47

In this study, synthesis of silica nanoparticles has been achieved by alkaline hydrolysis of TEOS using NH_4OH and ethanol. Specifically, 2.5 mL of NH_4OH was added to ethanol (50 mL) and stirred vigorously at 60ºC for 1 h. After that, 5 ml of TEOS was added dropwise to the former solution and vigorously mixed for 2 h to produce silica nanoparticles.

3.2.3   Preparation of SSO coating

Hydrophobic silica nanoparticles were produced by adding OTS (4% v/v) to former silica nanoparticles solution then vigorously mixed at room temperature for 3 h to obtained formation of self-assembly monolayers (SAM) on the silica nanoparticles surface. Therefore, SSO coating was prepared by addition of shellac (5% v/v) ethanol solution at room temperature into the hydrophobic silica nanoparticles solution.

3.2.4 SSO Coating on Different Substrates

This SSO coating solution then further spray coated on the surface of polypropylene (PP), glass, polyethylene terephthalate (PET), cotton, wood, metal, and concrete block. Our SSO coating can also be applied on these substrates by using different methods like dip coating, paint brushing and sonication bath to obtain similar results like spray coating. After spray coating of SSO solution on these substrates, it was further heat treated in hot air oven at 70º C for 2 h to harden the shellac biopolymer and removal of the moisture from the surfaces. Schematic 1 shows synthesis of SSO and coating technique.

3.2.5 Characterization of Materials

First, the Si-NPs particles size and size distribution results were obtained using Zetasizer (Nano ZS, Malvern, UK) via dynamic light scattering. The high-quality mobile camera was used to capture images and slow-motion videos. Cold Field Emission Scanning Electron Microscope

Cold FE-SEM (SU8220, Hitachi High-Technologies, Japan) was used for obtaining surface morphology of the pristine and SSO coated samples at 10 kV accelerating voltage 7 µA current. Fourier transformed infrared spectroscopy FTIR (Varian, Agilent Technologies, USA) was performed to confirm the presence of various organic functional groups in SSO coating solution. Thermogravimetric analysis (TGA) (TA Instruments Q-600) was performed in air to measure the thermal stability of shellac and SSO coating shown in supplementary Fig. S3. X-ray photoelectron spectroscopy (XPS) was used for elemental identification in SSO coating on K-Alpha XPS system (Thermo Fisher Scientific, USA) equipped with double focusing hemispherical analyzer and monochromatic Al Kα source (1486.6 eV).

3.2.6 Analysis of Contact Angle

To examine the wetting properties of these SSO coated samples, images of the sessile water droplets were acquired with a Rime-hart instrument and analyzed with DROPimage Advanced version software. 5 µL droplets of deionized water (18.2 MΩ cm) were used for static contact angle measurements. Synthetic acid rainwater was prepared by mixing sulphuric and nitric acid in deionized water (18.2 MΩ cm) while maintaining the pH of 4.2 to mimic the environmental hazardous acid rain conditions. The contact angle values were measured from different locations on the SSO coated samples surface after 30 s following the casting of the drop to make sure that droplet had reached its equilibrium position.

3.2.7 Analysis of Contact Angle Hysteresis

The sessile drop methodology for evaluating wetting and hydrophobic behavior of the SSO coated and pristine substrates was performed by using a Phoenix 300 Plus instrument (Surface & Electro Optics Co., Ltd., South Korea). In this study, the dynamics of wetting behavior was understood by performing contact angle hysteresis (CAH) analysis. Both the maximum

advancing contact angle (θ_A) and minimum receding contact angle (θ_R) has been recorded for a smaller droplet (1 µL/sec) over 30 frames with 1 sec intervals. Finally, the CAH was calculated as mentioned in Equation 1.1.[26]

3.2.8 Durability Tests

The sandpaper (600 mesh) was used for abrasion analysis to test the durability of SSO coated substrates. The definition for 1 cycle of abrasion in our study is when these SSO coated substrates samples were subjected below the 200g of load and faced down to the sandpaper and moved for 10 cm along the ruler. The water contact angle was measured after every 5 cycles to evaluate the retained hydrophobicity of these coated samples. High temperature effect on SSO coated substrates was measured by placing these samples on hot plate for 2h, with temperatures varying from 50 to 150 ˚ C with increments of 25 ˚ C.

3.3 Results and Discussion:

3.3.1 Surface Morphology Analysis of Uncoated and SSO coated Substrates

The facile stepwise approach for synthesizing superhydrophobic SSO coating has been illustrated in Figure 3.1. The first step entails the synthesis of silica nanoparticles using TEOS and ammonium water by sol-gel method. Hydrophobic silica nanoparticles are prepared by additional functionalization of these silica nanoparticles by mixing with hydrolyzed octadecyltricholosilane (OTS), which is a fluorine free alkylated silane. Shellac biopolymer solution in ethanol was then added into the hydrophobic silica nanoparticles solution at room temperature.
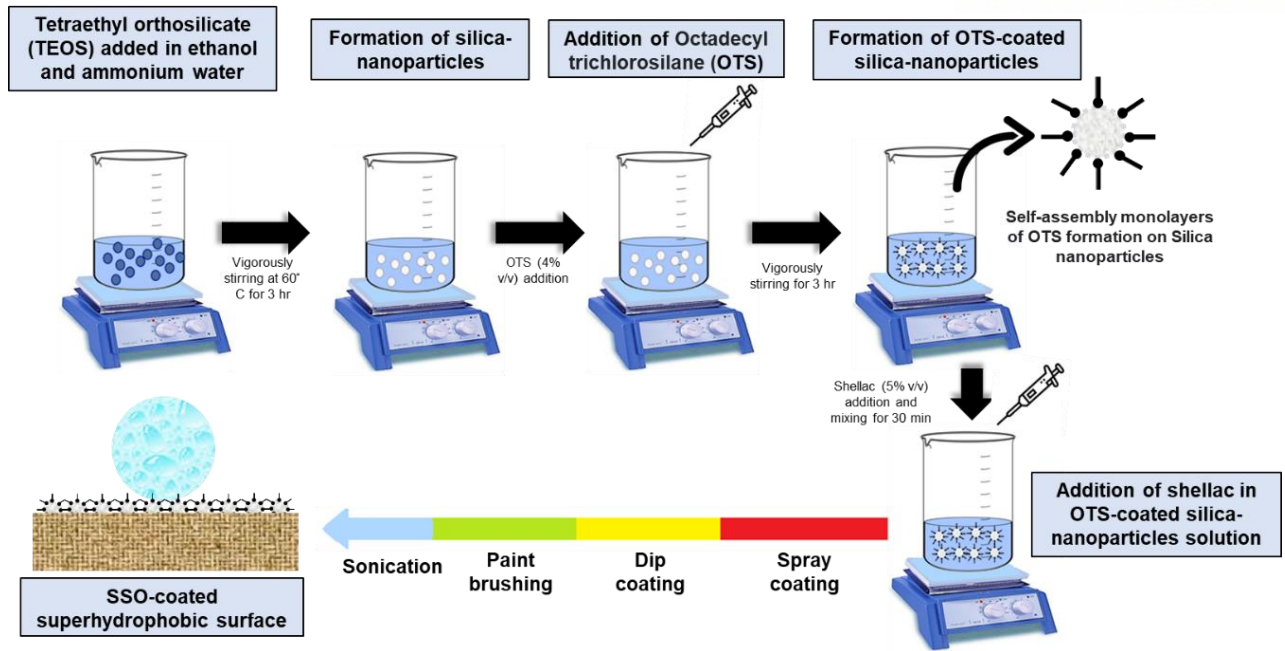
Figure 3.1: Schematic representation of making process of SSO coating solution.

Shellac acts as a bio adhesive for strong binding of these hydrophobic silica nanoparticles onto any given substrates. This resulting SSO coating suspension is now ready for one step spray coating. This combination of shellac, silica nanoparticles modified with octadecyltricholosilane has shown the best outcome in terms of non-wetting behavior as compared with other combination of these chemicals (Figure 3.2). Interestingly, this SSO coating can be applied to different by using dip coating, paint brushing, and sonication bath as well to obtain similar superhydrophobic wetting behavior. This SSO coating suspension sprayed coated on multiple substrates like polypropylene (PP), glass, and polyethylene terephthalate (PET), to obtain excellent non-wetting and durable characteristics.
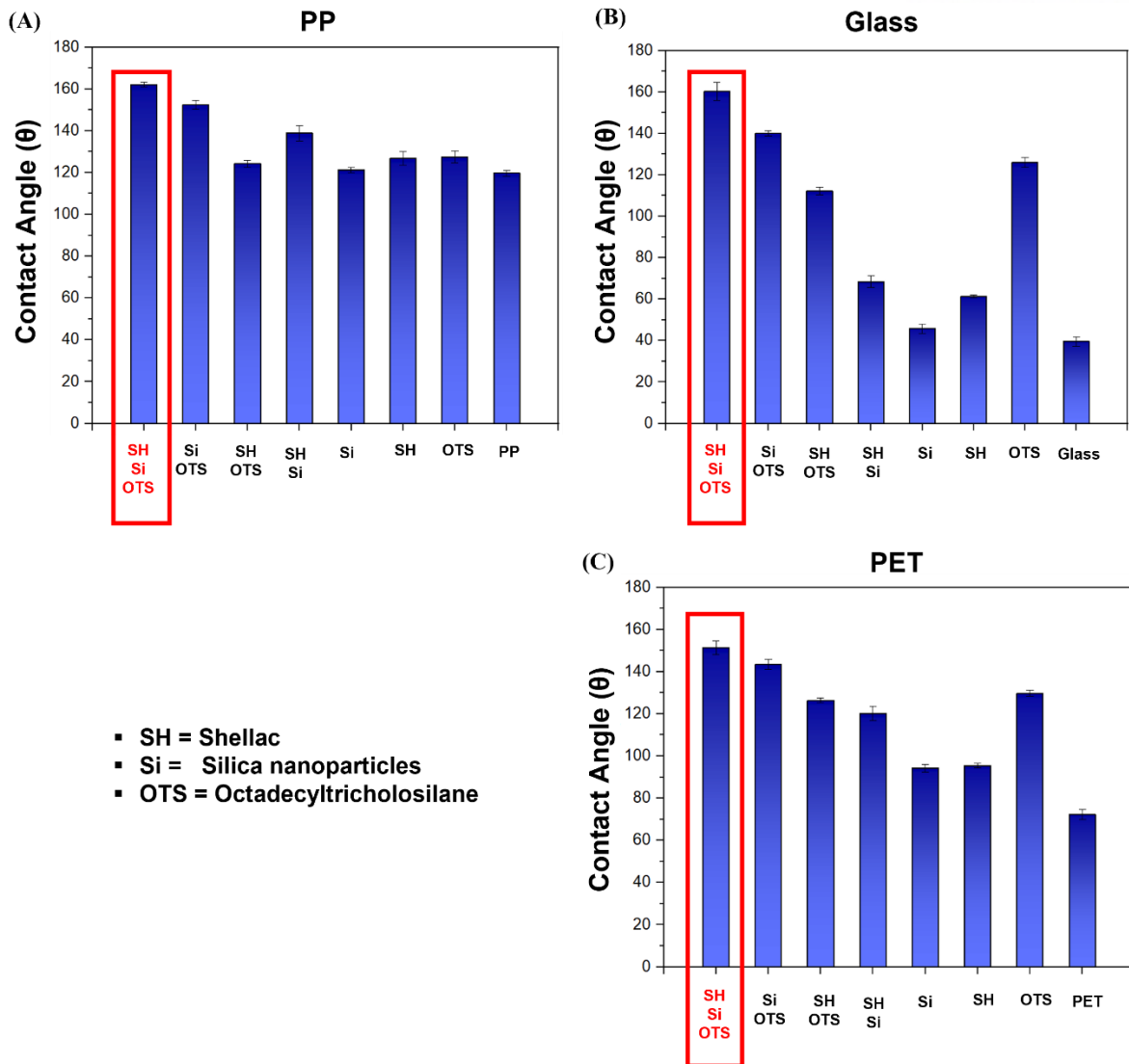
Figure 3.2: Different type of coatings (A) multiple types of coating combination contact angle data for pp (B) multiple types of coating combination contact angle data for glass (C) multiple types of coating combination contact angle data for pet.

The surface morphology and hierarchical structure of the SSO coated and smooth pristine surface substrates were analyzed by cold FE-SEM as shown in Figure 3.3. As can be seen from high and low magnification SEM images in the Figure 3.3 (A, C, E) the pristine polypropylene (PP), glass, and polyethylene terephthalate (PET) respectively shows smooth surfaces as

52
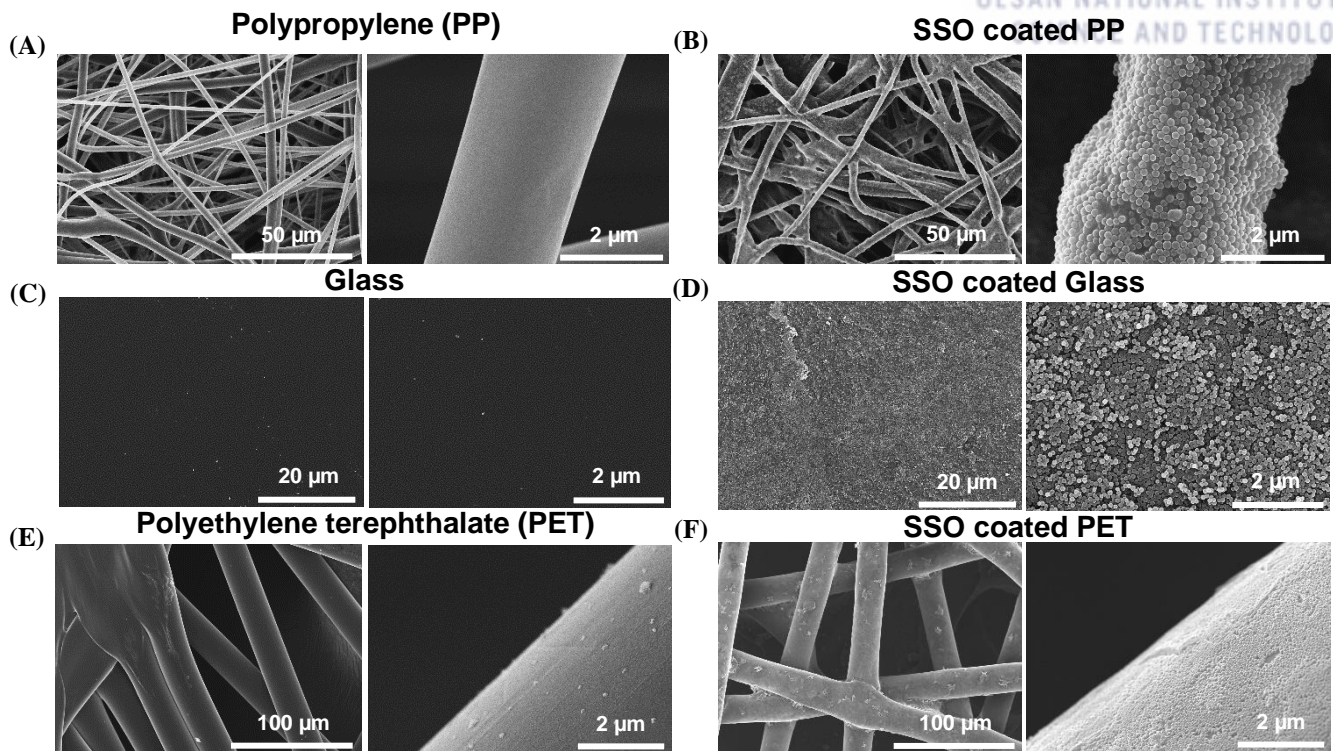
Figure 3.3: Surface morphology analysis of uncoated and SSO coated substrates (A) polypropylene (B) SSO coated PP (C) glass (D) SSO coated glass (E) polyethylene terephthalate (F) SSO coated PET.

compared to the rough surfaces of SSO coated PP, glass, PET in high and low magnification images of Figure 3.3 (A, C, E). The low magnification images in the Figure 3.3 (B, D, F) of SSO coated PP, glass, and PET showed that the hydrophobic silica nanoparticles are uniformly distributed and close-packed all over these coated surfaces due to the presence of bio adhesive polymer shellac. Some silica nanoparticles modified with OTS in the high magnification SEM image in Figure 3.3 (B, D, F) showed that aggregated into micro features which results in hierarchical roughness. It can be well observed that these SEM images smooth surfaces of (a) pp, (c) glass, (e) pet along with modified surfaces of SSO coated (b) pp, (d) glass and (f) pet.

3.3.2   Chemical and Elemental Characterization

Micro/nano features are composed of hydrophobic silica nanoparticles bound together by the shellac biopolymer as well as due to presence of long chain alkyl group on the surface of OTS modified silica nanoparticles. It is evident that microscale and nanoscale roughness is essential for the super hydrophobicity of the resulting materials. The silica nanoparticle size was successfully measured by using dynamic light scattering (DLS) technique based Zetasizer. The mean hydrodynamic diameter of synthesized silica nanoparticles was found to be 118.7 nm as shown in (Figure 3.4A) and high-resolution FE-SEM image for showing the size and shape of these silica nanoparticles (Figure 3.4B).
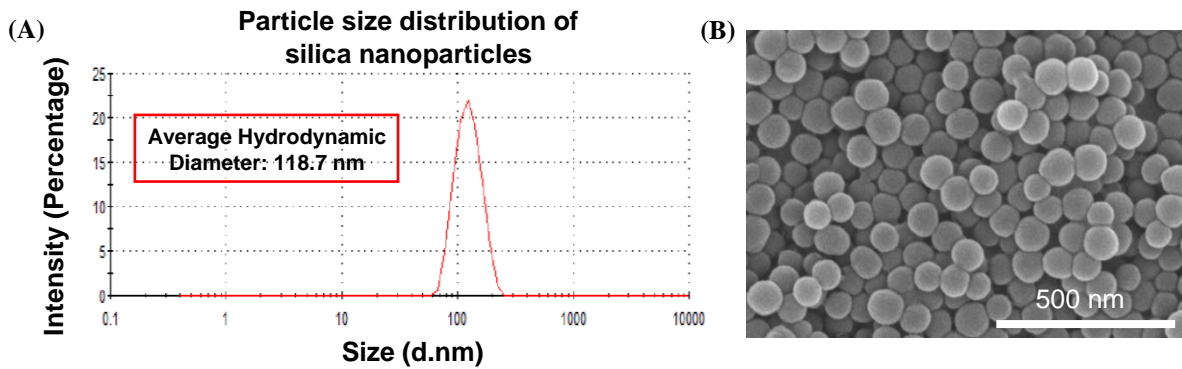
Figure 3.4: Dynamic light scattering and SEM data of silica nanoparticles (A) average particle size (B) SEM image of silica nanoparticles.
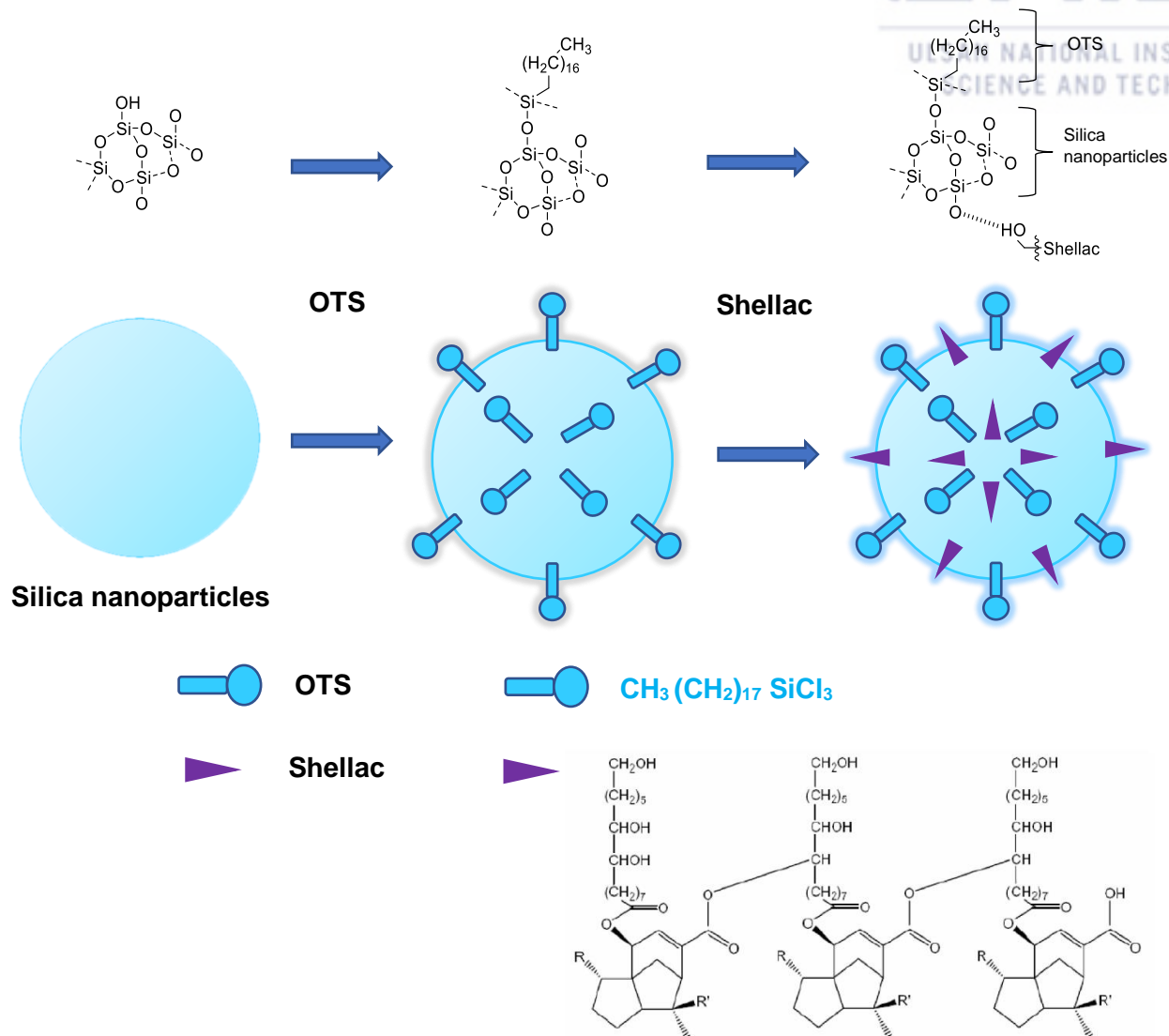
Figure 3.5: Schematic representation of chemical modification of silica nanoparticles surface.

Demonstrated the possible chemical reaction involved in synthesis of SSO coating material is shown in Figure 3.5. The attachment of the hydrophobic long chain alkyl silane on to the surface of silica nanoparticles as shown in Figure 3.5. To confirm the presence of organic functional groups in the shellac and SSO coating nanocomposite material FTIR spectroscopy (Figure 3.6 A, C) was performed. The C-H vibration at 2910 cm^{-1}and ester linkage of shellac moiety confirm with peat at 1100 cm^{-1} as shown in Fig. 2a. Fig. 2c indicates the stretching vibration of Si-O-Si at 1095 cm^{-1} and Si-OH stretching at 3200 to 3600 cm-1.

(A)

(B)

(C)

(D)
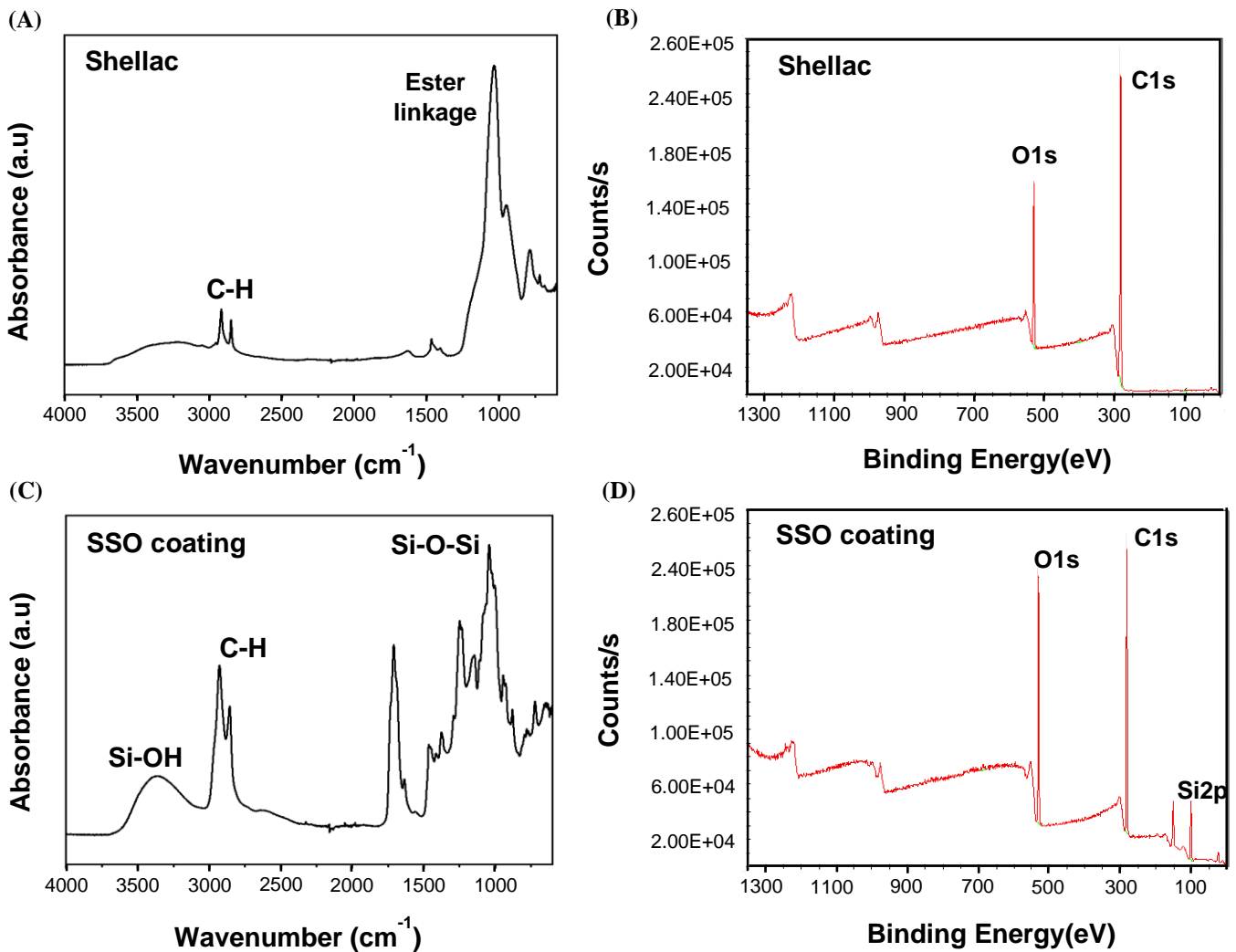
Figure 3.6: Elemental composition (A, C) FTIR spectrum of shellac and SSO coating solution respectively; XPS spectra of (B, D) shellac and SSO coating powder.

The two peaks at 2920 and 2855 cm^{-1} represent the C-H functional group. The presence of C-H and Si-O functional groups exhibit the attachment of the hydrophobic OTS tail to the surface of silica nanoparticles. High resolution XPS spectroscopy has been used for identification of elemental composition of the shellac and bio adhesive based SSO coating nanocomposite material. As represented in Figure 3.6B, the high-resolution spectrum of shellac consists of two important peaks at 284.5 and 532eV, which corresponds to C1s and O1$_S$ respectively. On the other hand, in Figure 3.6D the results indicate for SSO coating nanocomposite material the

presence of C, O, and Si which confirms the successful modification with silica nanoparticles

and OTS. Thus, SSO coating nanocomposite material showed three prominent peaks at 282.3,

530.3 and 101.1eV, that corresponds to C1s, O1s and Si2p respectively.

3.3.3   Creation of Superhydrophobicity on Various Type of Surfaces

Formation of superhydrophobic surfaces is not always same for different type of substrate

materials by many fabrication techniques. As shown in Figure 3.7 the SSO coating exhibited

excellent water repellency characteristics for various types (solid and porous) of substrates

materials regardless of their rigidity, composition, and roughness like pp (nonwoven

facemask), glass (glass slide), pet (plastic), wood (pine wood), metal (aluminum block), cotton

(cotton shirting fabric), and concrete materials (portland cement). Additionally, a water droplet

test demonstrates complete rolling-off behavior of droplet for SSO coated substrates and

droplet sticking or spreading behavior for pristine substrates.

Figure 3.7A shows, UNIST name has been written by using methylene blue dyed water droplets

on SSO coated glass slides. The static contact angles (θ_{CA}) and sliding angle (θ_{SA}) values as

shown in Figure 3 (B, C) after SSO coating on various substrates were found to be in the range

of 151° to 162° and 4° to 8° respectively. Water droplets (5.0 µl) dyed with methylene blue

on different SSO coated substrates are shown in Figure 3.7D. Furthermore, a water jet

experiment demonstrates self-cleaning ability against organic pollutants like methylene blue

(MB) for SSO coated substrates and strong sticking or spreading behavior of MB for pristine

substrates after interaction with water. Therefore, these results agree with the prior studies in

which water droplets instantly rolled off nanoparticles-based structures, which reduced the

surface energy by forming micro/nano scale roughness and nanoscale air pockets.[27]
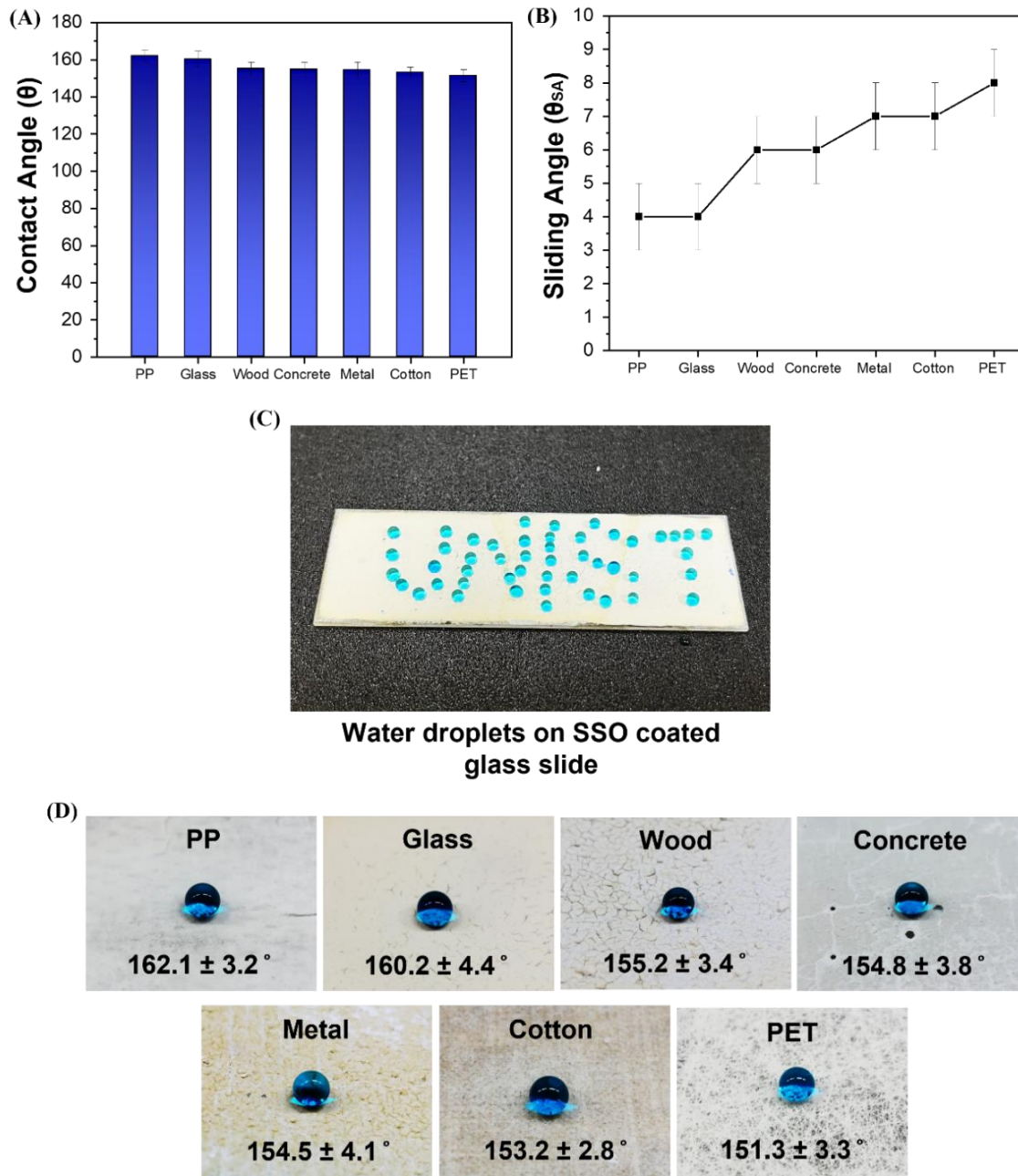
Figure 3.7: Creation of Superhydrophobicity on various types of surfaces. (A) Optical picture of dyed water droplets on SSO coated glass (B) histogram representation of contact angle values of various substrates (C) sliding angle values of various substrates (D) optical pictures of dyed water droplet on multiple substrates.

3.3.4 Wettability Behavior for Water and Acid Rain on Different Surfaces

The SSO coated substrates like pp, glass, and pet were also studied further for wetting behavior of water and acid rain. The pristine surface of pp, glass, and pet showed static contact angle (θ_{CA}) of 119.7±1.5 °, 39.6±2.3 °, 72.3±2.3 ° but the contact angle increased to 162.1±3.2 °, 160.2±4.4°, 151.3±3.3° respectively after SSO coating shown in Figure 3.8 (A, B). Acid rain
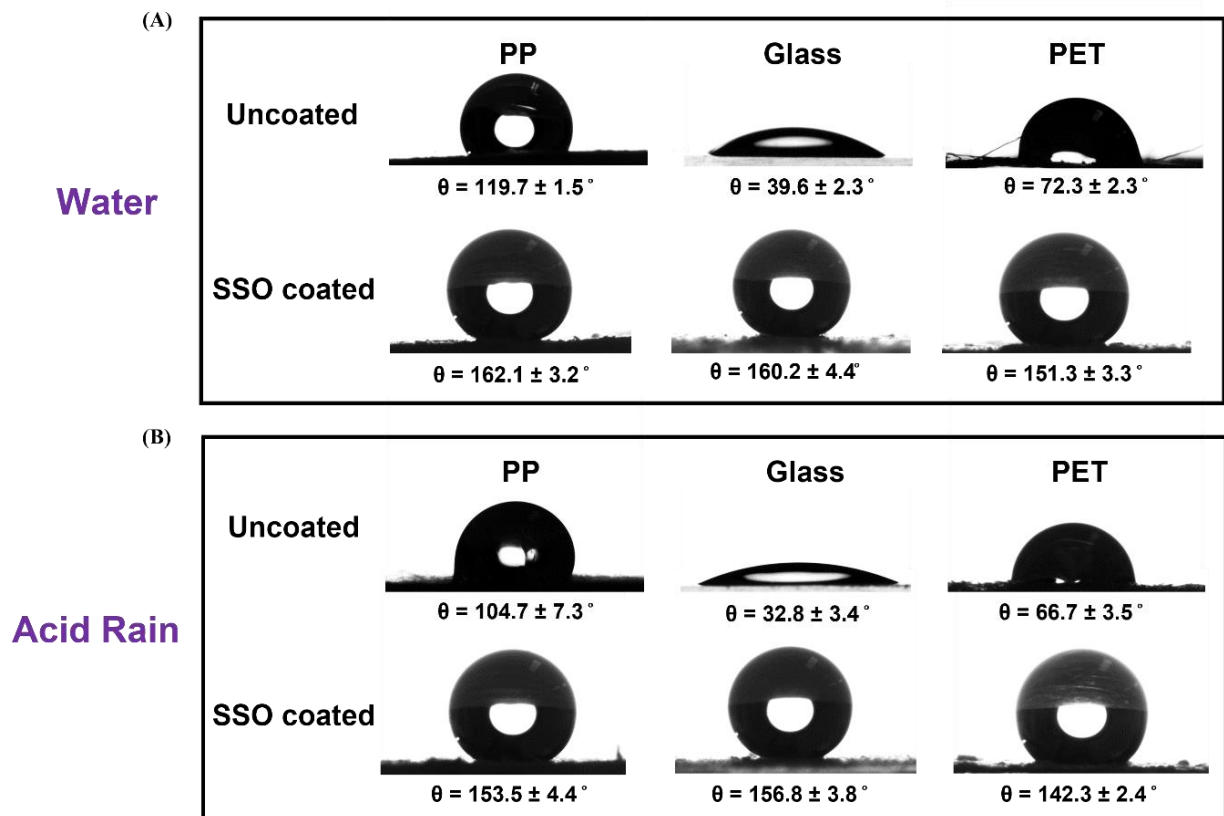
Figure 3.8: Wettability behavior for water and acid rain on different surfaces (A) water contact angle for uncoated (pp, glass, and pet) and SSO coated (pp, glass, and pet) (B) contact angle for acid rain for uncoated (pp, glass, and pet) and SSO coated (pp, glass, and pet).

is environmental hazards colors due to air pollution which can damage and decrease the services life of the surfaces comes in continuous contact with it.[14] Acid rain was prepared by mixing nitic and sulphuric acid in deionized water at the pH around 4.2 to imitate the

environmental acid rain. As shown in Fig. 4a, the static contact angle (θ_{CA}) for acid rain of

pristine pp, glass, and pet are 104.7±7.3 ᵒ, 32.8±3.4 ᵒ, 66.7±3.5 ᵒexhibit poor wetting behavior

against acid rain but in the case of SSO coated pp, glass and pet the contact angle increased to

153.5±4.4 ᵒ, 156.8±3.8 ᵒ, 142.3±2.4 ᵒshows excellent non-wetting behavior shown on Fig. 4b.

This anti-corrosive behavior for acid rain of SSO coated surfaces is due to the presence of silica

nanoparticles and shellac because this biopolymer cannot be ionized in pH < 7 and stays in

solid state.[93]
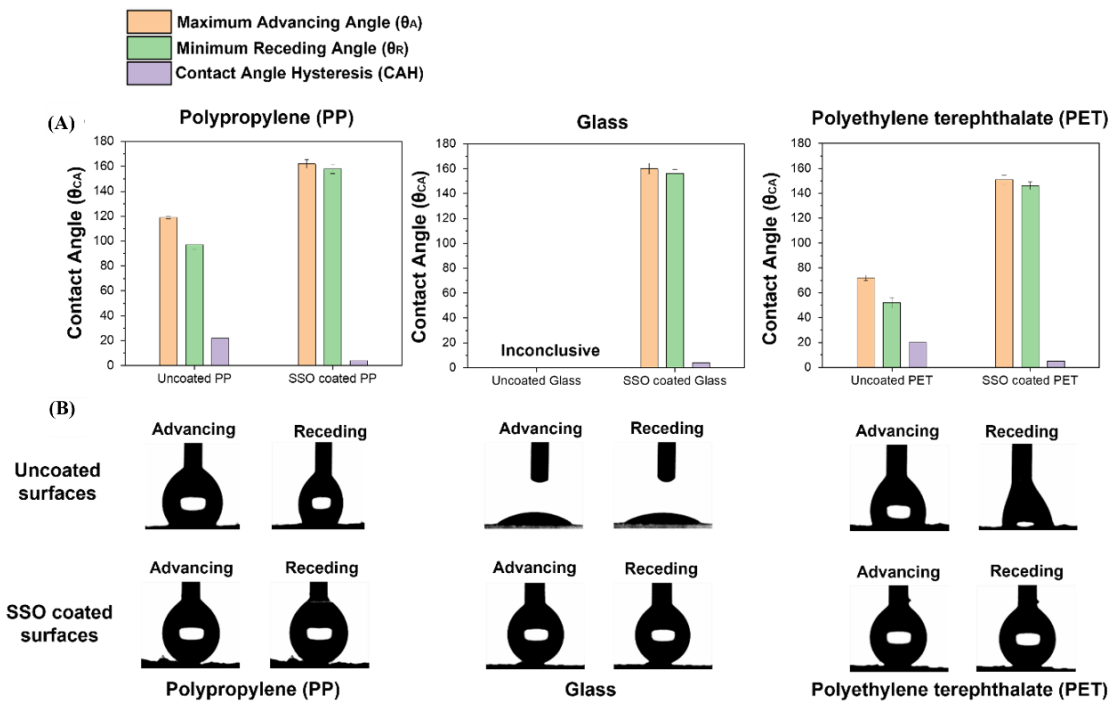
Figure 3.9: Contact angle hysteresis measurement. (a) histogram representation of contact

angle hysteresis for uncoated pp, glass, pet and SSO coated pp, glass, and pet (b) advancing

and receding angle images of pristine pp, glass, pet and SSO coated pp, glass, and pet.

3.3.5 Contact Angle Hysteresis Measurement

To understand water droplet adhesion on pristine and SSO coated surfaces contact angle

hysteresis (CAH) test has been performed. Contact angle hysteresis is one of the prominent

factors in surface chemistry to understand sticky or non-sticky behavior of substrates. It is defined as the difference between the maximum advancing contact angle (θ_A) and minimum receding contact angle (θ_R) which is usually used to analysis the wetting tendency of the surface.[26] Typically, θ_A shows the maximum contact angle, whereas θ_R exhibit the minimum contact angle for water droplet on a surface. Intriguingly, it was observed that a higher contact angle hysteresis value provides higher degree of water droplet adhesion and have higher tendency of corrosion for a surface. Mostly, superhydrophobic surfaces are non-adhesive, anti-corrosive and show exceptionally low water contact angle hysteresis. In other words, lower contact angle hysteresis value of superhydrophobic surfaces corresponds to high wetting stability against Cassie-Baxter to Wenzel transition.

A similar phenomenon can be observed in Figure 3.9 where the contact angle hysteresis was measured for pristine and SSO coated pp, glass, and pet. The SSO coated pp, glass, pet demonstrates non-sticky and slippery surface with extremely low contact angle hysteresis values 4°, 4°, 5° respectively as compared to the pristine material substrates shown in Figure 3.9A. However, contact angle hysteresis of pristine glass could not be easily determined due to extremely high hydrophilicity. In Figure 3.9B, water droplet advancing and receding condition on pp, glass, and pet has shown.

3.3.6 Durability Test of SSO Coated Surfaces

The non-wetting capability of superhydrophobic surfaces can be deteriorated by mechanical forces which can damage its surface morphology and chemistry. Therefore, it is important to evaluate the durability of the coated substrates to ensure the sustainability for real life applications. The abrasion test adopted in this current study is schematically shown in Figure 3.10A and the static water contact angle measurements through the 50 abrasion cycles for SSO

coated pp, glass and pet are shown in Figure 3.10B. It can be observed that abraded samples were able to maintain their non-wetting behavior even after 50 cycles, which indicates excellent durability for the developed SSO coating. After 50 cycles, the contact angle values for pp, glass and pet were 156.7±3.4˚, 154.8±3.5˚, and 144.7±2.5˚ respectively. This insignificant decline
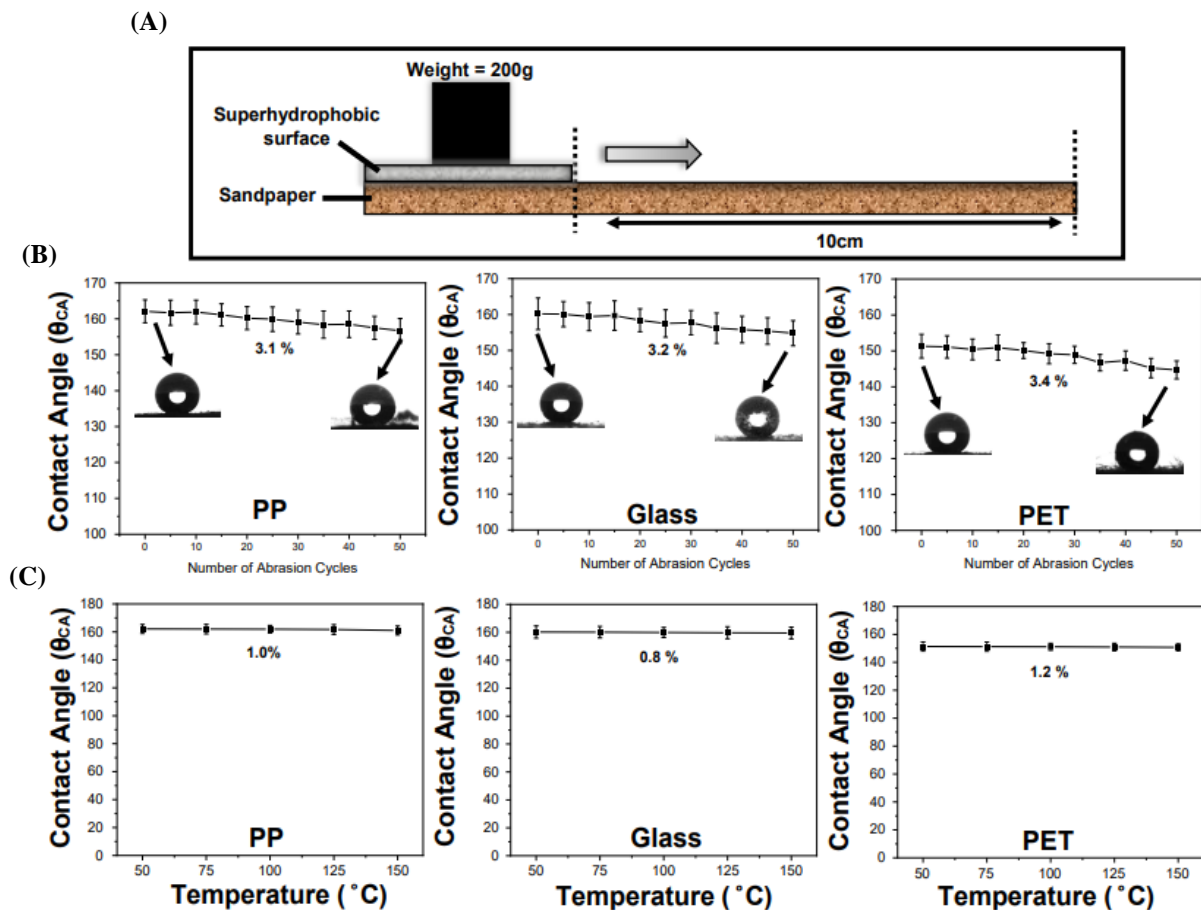
Figure 3.10: Durability test of SSO coated surfaces (A) schematic representation of abrasion test (B) contact angle values for SSO coated pp, glass, and pet after 50 cycles of abrasion test (C) contact angle values for SSO coated pp, glass, and pet till 150˚ C temperature treatment.

in contact angle due to the removal of small amount of hydrophobic silica nanoparticles from the substrates. The above abrasion test demonstrated that the SSO coated samples have excellent robustness and durability. This robustness could be attributed due to presence of shellac bio adhesive which helps these hydrophobic silica nanoparticles fixed and embedded

in the fibers and solid surface strongly. Thermogravimetric analysis (TGA) of shellac and SSO

coating powder data shown in Figure Additionally, the SSO coating has demonstrated thermal

stability by maintaining non-wetting behavior even after treatment with high temperature till

150˚C after exposure for 2h as shown in Figure 3.10C.
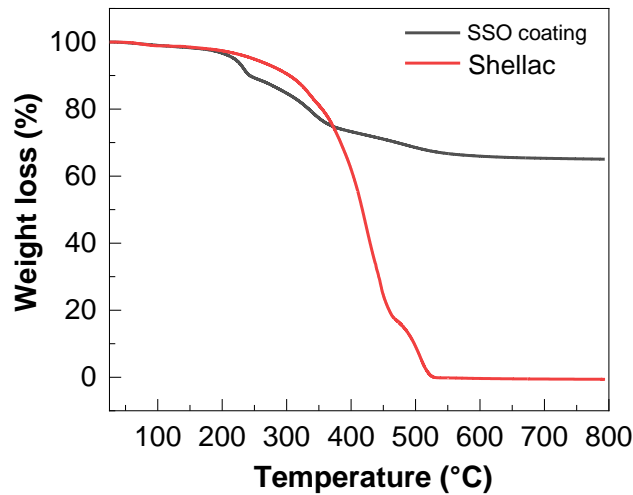
Figure 3.11: Thermogravimetric analysis (TGA) of shellac and SSO coating powder.

Several techniques were used previously to fabricate self-cleaning and hydrophobic surfaces

with non-wetting behavior and addressed the challenges of surface wetting and fouling. Thus,

important milestones were reviewed to correlate the former studies with feature enhancements

relative to current superhydrophobic surface fabrication and adhesive based coating methods.

Table 3.1 presents the detailed comparative studies on the sophisticated superhydrophobic

coatings to different substrates or materials reported earlier.

Coating Materials	Coated Substrates	Contact Angle (Maximum)	Durability Test (Total cycles)	Coating Methods	Reference
SiO_2-g-(PGMA-co-P12FMA) core-shell structure	Glass	119°	30	Film casting method	[96]
Polyurethane/amino silicon oil/perfluorodecyltriethoxy silane-MWCNT composite	Glass, aluminum, iron, wood	156.9±2.7°	-	Spray coating	[97]
SiO_2 /perfluorodecyltriethoxysilane (FAS)/epoxy resin (EP)/dark NIR-reflective pigments nanocomposite	Aluminum plate	153.4±0.4°	-	Spray coating	[98]
Alpha®SI30 resin and TIO_2 nanoparticles	Marble stones	155±2°	-	Dip coating	[99]
PDMS basecoat and PMC/Silica nanoparticles composite	Wood, filter paper, cotton	150°	20	Spray coating	[100]
Bio-adhesive shellac and Copper nanoparticles composite	Nonwoven	143.4±3.9°	-	Microfluidic based spray coating	[83]
PDMS/carbon particles composite	Glass, aluminum, titanium	151.6±1.3°	-	Drop-casting process	[101]
Gelatin adhesive-based carbon nanofibers incorporated with hydrophobic SiO2 nanoparticles	Glass, microfiber filter papers, poly bag,	141°	10	Dip coating of hydrophobic nanoparticles onto adhesive spray coated substrate	[27]
Bio-adhesive shellac and silica nanoparticles hydrophobized with OTS (SSO) coating	Nonwoven, glass, plastic, wood, metal, cotton, concrete	162.1±3.2°	50	SSO coating can be applied by spray, dip, painting, sonication method	This study

Table 3.1: Comparison studies between previous and this work.

Chapter 4

Superhydrophobic sand

Publications:

Surface innovation for fabrication of superhydrophobic sand grains with improved water holding capacity for various environmental applications. Saikat Sinha Ray[1], Ritesh Soni[1], In-Chul Kim, You-In Park, Chang Young Lee, and Young-Nam Kwon. Environmental Technology and Innovation, vol. 28, pp. 102849-102861, 2022. ([1] contributed equally)

4.1 Introduction

Water sources in arid and desert regions are extremely limited, complicating water supply to domestic, agricultural, and industrial sectors. Furthermore, water pollution in arid and desert regions is a significant, unacceptable, and irreversible threat.[102] Furthermore, a substantial amount of water supplied to soil/sand is lost due to evaporation and percolation.[103] Layers impermeable to water have been studied to minimize water loss through evaporation and percolation. For example, plastic mulches have been used to wrap the soil surface to minimize percolation and evaporation. Plastic mulches have been commercially used for both small fruit crops and vegetables. However, the installation of plastic mulches is expensive, labor-intensive, and unsustainable due to plastic pollution.[104] As an alternative, the use of engineered nanomaterials has been shown to improve water-usage efficiency in agricultural applications, as exemplified by "superhydrophobic sand", which is obtained by modification using nanomaterials, and can tackle the issue of desertification and enhance plant growth in arid environment.[105] Superhydrophobic sand also reduces diffusion of underground salts and affects plant growth.[106, 107] Therefore, harnessing the superhydrophobic characteristics of various nanomaterials is a key research area of global significance. Additionally, superhydrophobic materials can be utilized for effective oil/water separation. [108]

In this study, superhydrophobic sand surfaces with anti-wetting and self-cleaning properties were produced for various purposes, such as improved agricultural productivity and oil/water separation. The facile approach entails the hydrolysis of tetraethyl orthosilicate (TEOS) in ethanol to produce a silane sol, and subsequently, fluoroalkyl silane was hydrolyzed in ethanol to produce alkylsilanol. Fluoroalkyl silane was used to lower the surface energy of the coated silica nanoparticles. Sea sand (SS) grains were functionalized with silica nanoparticles (Si-

NPs), followed by 1H,1H,2H,2H-perfluorooctyl-trichlorosilane (FDTS) to impart superhydrophobic characteristics, as illustrated in Figure 4.1. To the best of our knowledge, the combination of TOES and FDTS has not been explored before, and this study presents and
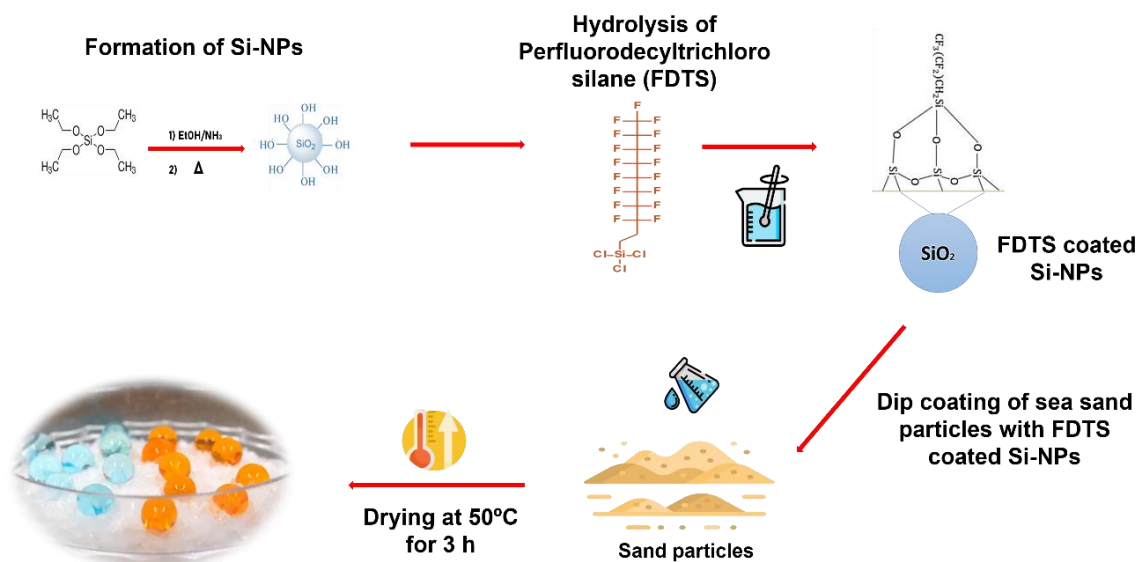
Figure 4.1: Chemical mechanism involved in modifying sea sand particles using silica nanoparticles (Si-NPs) coated with perfluorodecyltrichlorosilane (FDTS). Reproduced with permission.[45] Copyright 2022, Elsevier.

evaluates a novel approach for coating of sand grains in a single step to enhance water-use efficiency in agriculture. The average contact angle, rolling-off angle, and contact angle hysteresis were recorded to understand the dynamics of wetting resistance of the produced sea sand grains. The functionalized sea sand grains were impermeable to water, suppressing water loss through percolation or evaporation. Although superhydrophobic materials or filters are widely utilized for efficient oil/water separation, very few are energy conservative and inexpensive. Additionally, a similar approach was applied to modify regular sand (RS) using Si-NPs/FDTS to create a natural filter for oil/water separation. Our study demonstrates a simple and facile approach for generating superhydrophobic sand without the need for complicated

facilities. The modified sand could potentially be applied to improve agricultural productivity under arid conditions.

4. 2 Materials and Methods

4.2.1 Starting Materials

SS grains of 15-20 mesh size were acquired from Daejung Chemicals, South Korea. FDTS was obtained from Alfa Aesar. Ethanol was obtained from Daejung Chemicals (Seoul, South Korea). TEOS and ammonium hydroxide (reagent grade) were purchased from Sigma and Alfa Aesar, respectively, and were used without further purification.

4.2.2 Preparation of Silica Sol

TEOS was hydrolyzed under alkaline conditions using ammonia hydroxide in ethanol. Specifically, 5 mL of ammonium hydroxide was added to ethanol (100 mL) and stirred vigorously at 60 °C for 1 h. Then, 5 ml of TEOS was added to the solution and vigorously mixed for 6 h to generate a silica sol. Meanwhile, FDTS was added to ethanol (3%v/v) and vigorously mixed for 6 h to produce an alkylsilanol solution. Then the FDTS solution was added to the silica sol solution to produce the modified silica sol (Si/FDTS).

4.2.3 Sand Grain Coating

Initially, SS was sonicated in Si/FDTS for 1 h to achieve a uniform coating. The coated SS (SS-Si/FDTS) samples were then filtered, dried overnight, and kept in a hot-air oven at 50 °C for 3 h to remove moisture. Figure 4.1 shows a complete process of the anti-droplet sand coating.

4.2.4 Characterization

Images and slow-motion videos were captured using a high-quality mobile camera. The average water contact angle was evaluated using a Phoenix 300 Plus instrument (Surface & Electro Optics Co., Ltd., Korea). Initially, the Si-NP particles were subjected to nanoparticle analysis to evaluate their size and size distribution using a Zetasizer Nano (ZS, UK). In this study, three samples were analyzed under the same conditions in. The morphologies of the unmodified and functionalized sand particles were imaged using a field-emission scanning electron microscope (FE-SEM; 200 FEG Quanta, FEI company). In addition, elemental mapping was performed using an energy-dispersive X-ray spectroscopy (EDS) detector equipped with FE-SEM. Fourier transform infrared spectroscopy (FTIR) was performed to confirm the presence of various organic functional groups in the functionalized sand particles. Elemental identification was performed using X-ray photoelectron spectroscopy (XPS) (Thermo Fisher Scientific, K-Alpha, USA).

4.2.5 Analysis of Contact Angle Hysteresis (CAH)

The hydrophobicity and wetting phenomena of the functionalized SS grains were evaluated using sessile drop methodology. Herein, the contact angle hysteresis (CAH) was determined to understand the dynamics of the wetting tendency. The maximum advancing contact angle (Θ_A) was recorded for a small droplet (1 µL/sec) over 30 frames with 1 sec intervals. Subsequently, the minimum receding contact angle (Θ_R) was recorded by gently absorbing a droplet at 1 µL/s. Finally, the CAH was determined according to Equation 1.1. [109]

4.3 Results and Discussion

4.3.1 Particle Size Distribution of Si-NPs

The silica particle size was successfully recorded using a Zetasizer Nano device following the working principle of dynamic light scattering (DLS) technique. DLS was used to evaluate the

particle size of the prepared nanomaterials. The mean hydrodynamic diameter of the nano-silica particles was found to be 131.7 nm, as shown in Figure 4.2A. Furthermore, the polydispersity index (PDI), which indicates the average uniformity of nanoparticle dispersion [110, 111], was 0.109. Typically, PDI values > 0.8 indicate lower stability for a nano-delivery/drug delivery/colloidal system. A uniform and smooth distribution was confirmed based on the SEM images shown in Figure 4.2B.
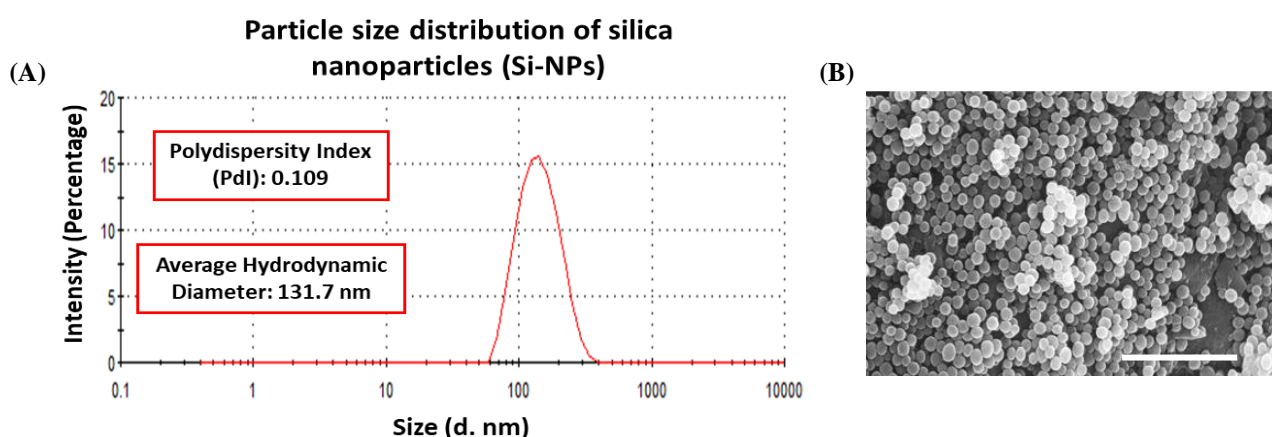
Figure 4.2: Dynamic light scattering and SEM data of silica nanoparticles (Si-NPs) (A) Particle size distribution of Si-NPs (B) SEM image of prepared Si-NPs. Reproduced with permission.[45] Copyright 2022, Elsevier.

4.3.2 Elemental Composition of Modified Sea Sand Grains

FTIR spectra confirmed the presence of the desired functional groups. Figure 4.3A shows the FTIR spectrum of the coated silica (Si-NPs/FDTS), indicating the stretching vibration of Si-O-Si at 1096 cm^{-1},[112] as well as the Si-OH stretching at 880 cm^{-1} and 3200-3600 cm^{-1}. The peak at 1199 cm^{-1} corresponds to C-F functional groups. The presence of Si-O and C-F functional groups indicate the attachment of the hydrophobic FDTS tail to the surface of silica nanoparticle.[113]

The elemental composition of the unmodified and modified sea sand particles was characterized using XPS spectroscopy. As indicated in Figure 4.3(B, C), the scanning spectra of the unmodified SS particles contain three prominent peaks at 103, 284.5, and 531.5 eV, which.
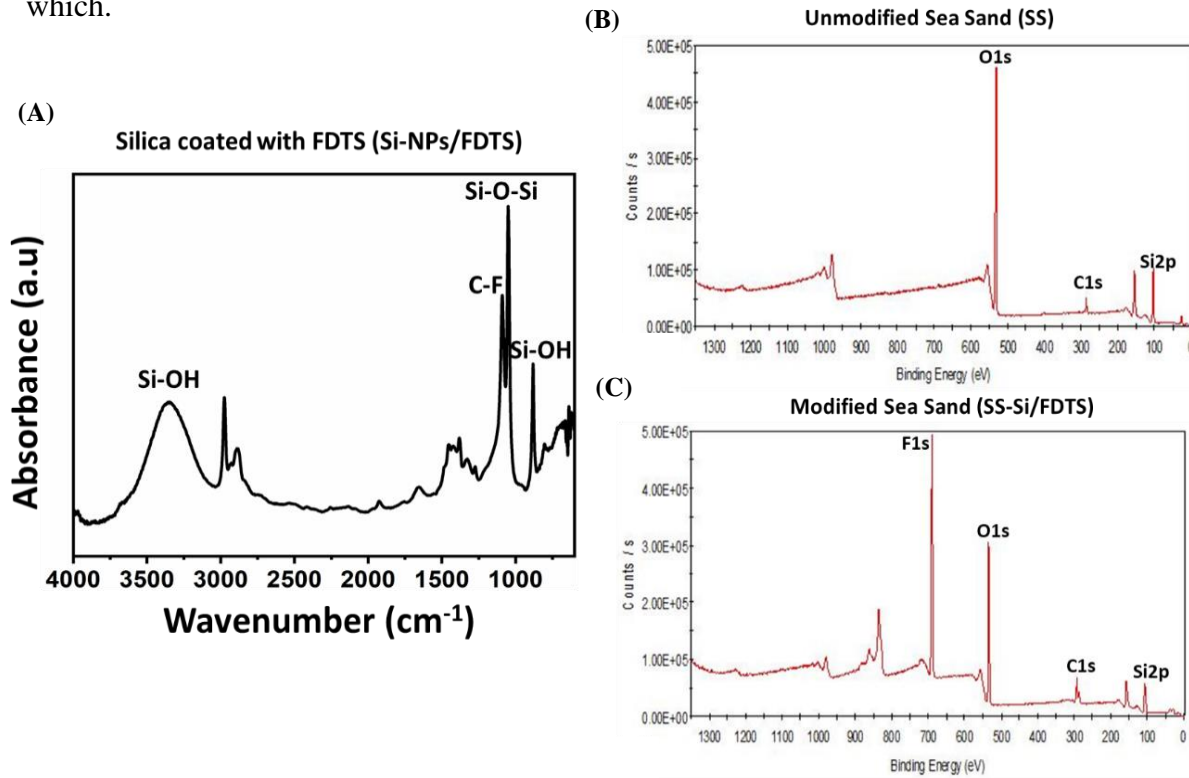
Figure 4.3: Elemental composition of unmodified and modified sea sand (A) FTIR spectrum of coated silica (Si-NPs/FDTS); XPS spectra of (B) unmodified sea sand (SS) and (C) modified SS (SS-Si/FDTS). Reproduced with permission.[45] Copyright 2022, Elsevier.

correspond to Si2p, C1s, and O1s, respectively. The results indicate the presence of Si, C, and O and confirm that the primary component of sand is silica (SiO_2) in the form of quartz. After successful treatment with FDTS-coated Si-NPs, the modified SS particles (SS-Si/FDTS) gave rise to five intense peaks at 104, 292.5, 284.5, 533.5, and 688 eV, which are associated with Si2p, C1s, C1s, O1s, and F1s respectively, confirming the presence of Si, C, O, and F

4.3.3 Morphological Study

The SEM images in Figure 4.4A show that most of the unmodified SS grains are angular or

(A)   (B)
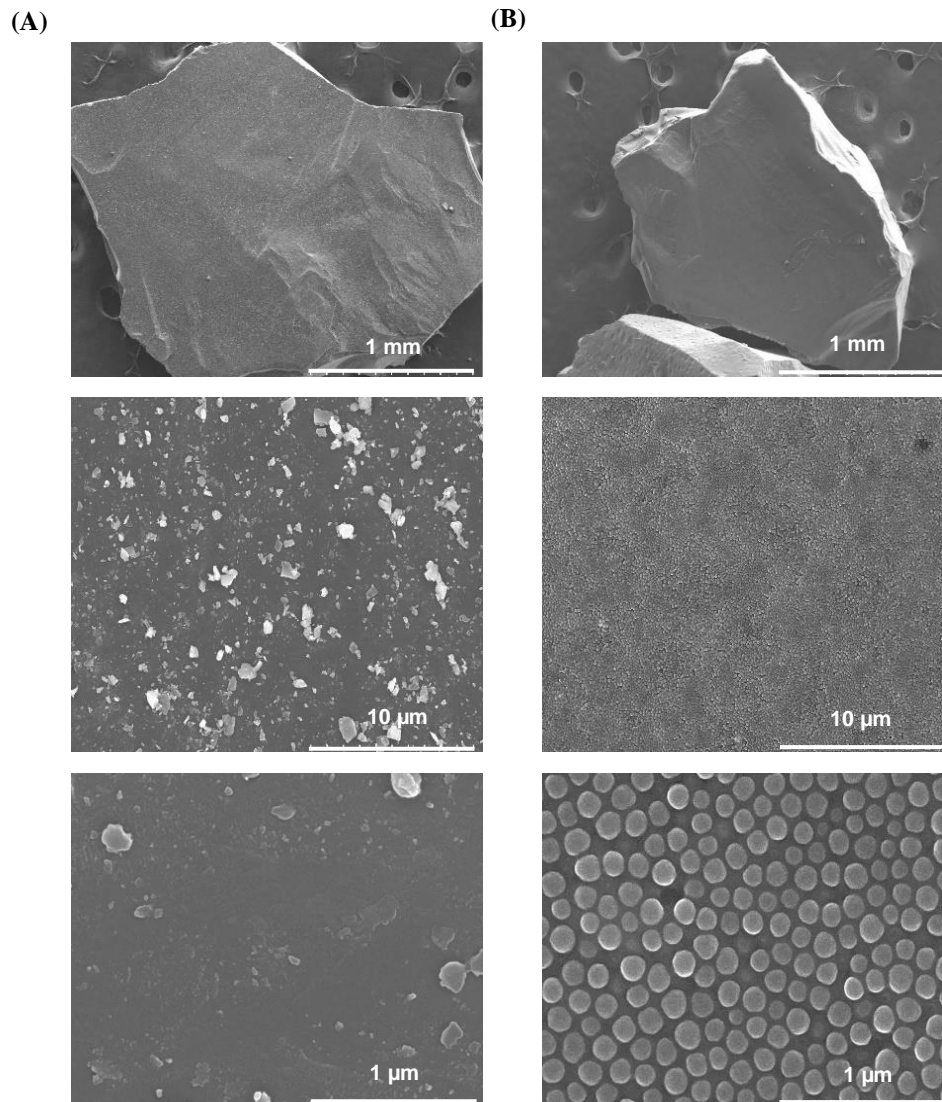
Figure 4.4: Surface morphology of unmodified and modified sea sand (A) unmodified SS grains for different magnification (B) SS-Si/FDTS) grains for different magnification. Reproduced with permission.[45] Copyright 2022, Elsevier.

subangular with sizes ranging between 750 and 1000 µm. After modification with Si-NPs/FDTS, the SS was uniformly coated with the nanoparticles to form SS-Si/FDTS, as confirmed by the SEM images in Figure 4.4B. The silica nanoparticles were mostly spherical with diameters in the range of 100 to 150 nm, as supported by the DLS results in Figure 4.2.

(A)   **Uncoated Sea Sand (SS)**

Element	Weight %	Atomic %
C K	0.56	0.95
O K	49.87	63.24
Si K	49.57	35.81

(B)   **Modified Sea Sand (SS-Si/FDTS)**

Element	Weight %	Atomic %
C K	16.13	24.70
O K	31.68	36.40
F K	15.13	14.64
Si K	37.06	24.26
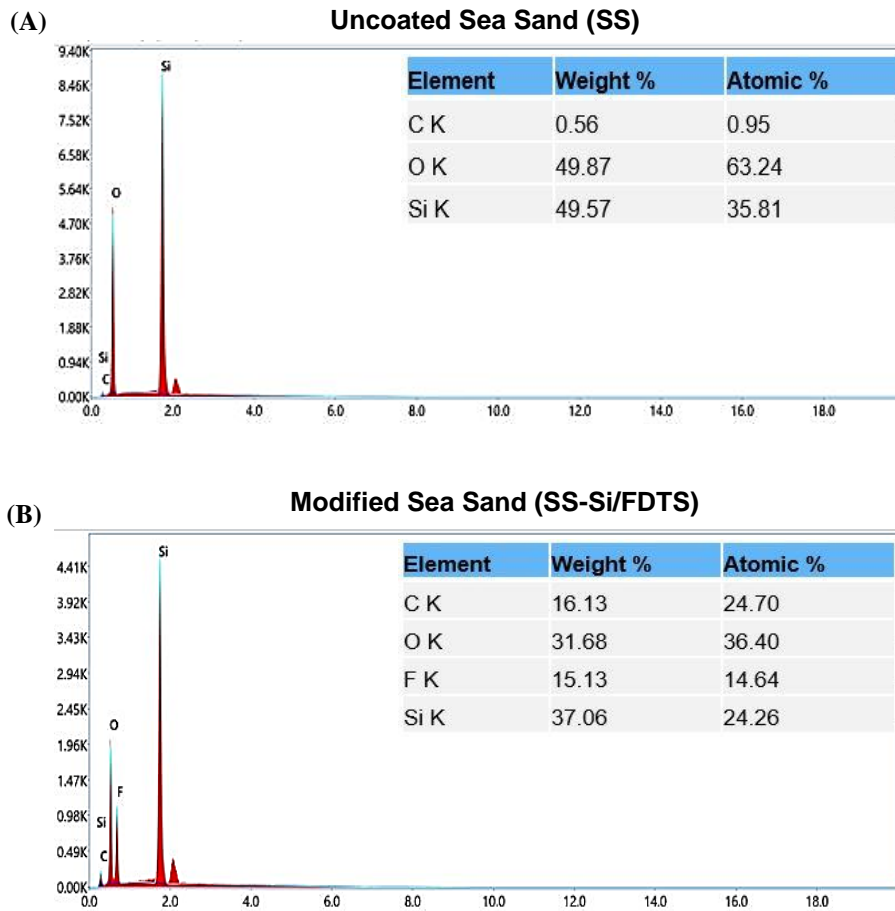
The successful modification of SS with Si-NP/FDTS was further confirmed by EDS analysis. The EDS spectra in Figure 4.5 (A, B) show that the unmodified sand grains consist mostly of Si and O, corresponding to the composition of quartz. In the case of SS-Si/FDTS, Si and O mapping indicated that the entire SS grain surface was covered by Si-NPs. The consistent distribution of Si, F, and C confirms successful surface modification with Si-NPs/FDTS, as shown in Figure 4.5 (C, D) EDS elemental mapping indicated a stable dispersion representing C and F signals from the -CF3, -CF2, and -CH3 moieties in hydrolyzed FTDS.

(C) **Uncoated Sea Sand (SS)**   **(D)** **Modified Sea Sand (SS-Si/FDTS)**
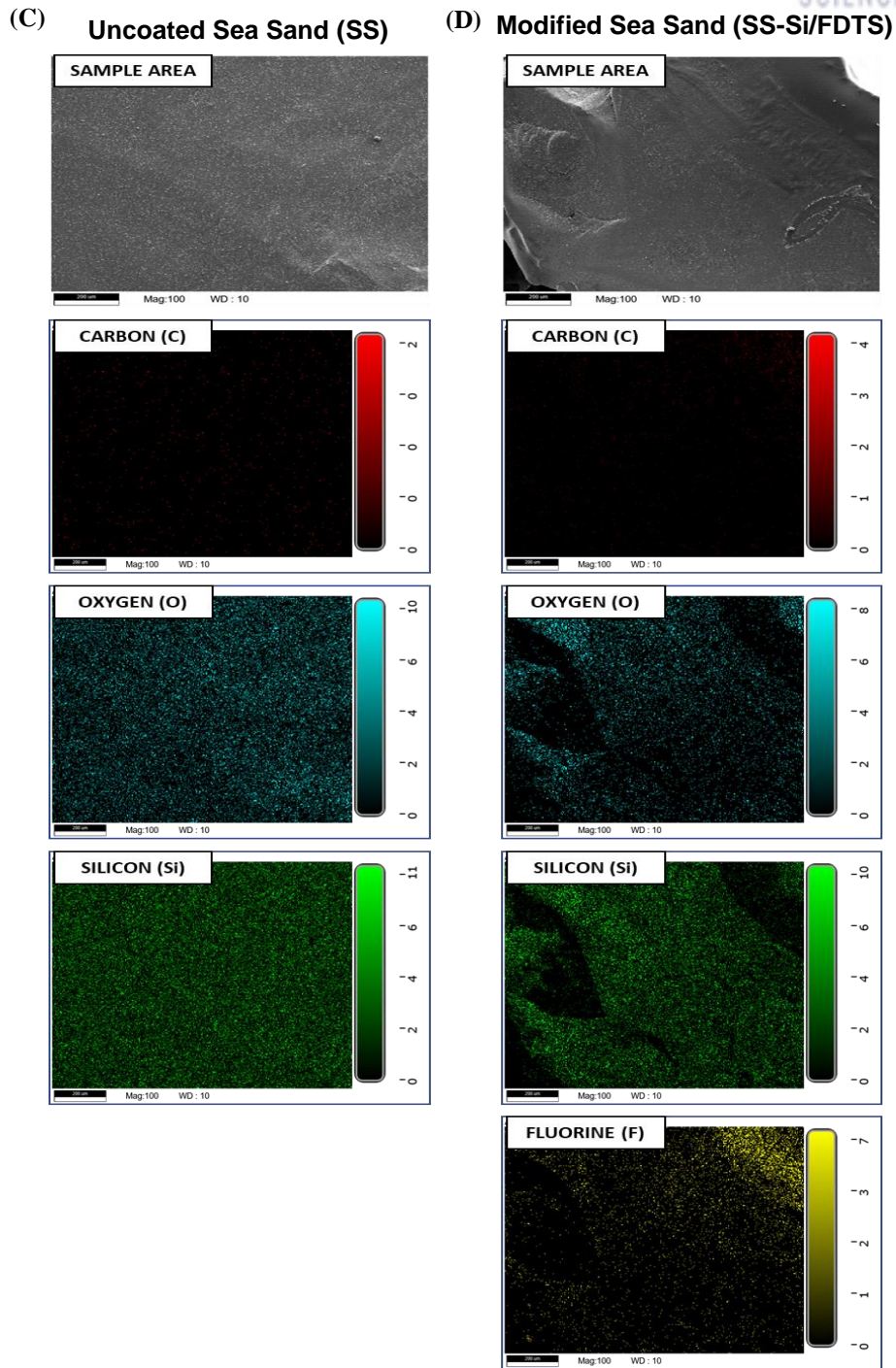
Figure 4.5: EDS spectra confirming the elemental composition of unmodified and modified sea sand (A) unmodified SS and (B) modified SS; and EDS mapping (C) unmodified SS and (D) SS-Si/FDTS confirming the uniform deposition of surface modifiers on the latter. Reproduced with permission.[45] Copyright 2022, Elsevier.

74

4.3.4 Wetting Tendency of Modified Sea Sand Grains

The superhydrophobic surfaces of the coated sand grains were evaluated based on the average water contact angle and rolling-off angle, as shown in Figure 4.6 (A, B) The unmodified sand grains readily absorbed water, giving a water contact angle of 0° because the polar oxygen atoms in silica form hydrogen bonds with water molecules. Coating the sand with Si-NPs/FDTS rendered the surface superhydrophobic, and a mean contact angle of 151° was obtained.   Subsequently, to evaluate the self-cleaning nature of the modified sand, the rolling-off angle was measured. SS-Si/FDTS showed a rolling-off angle of 9.5°, whereas the value for unmodified SS could not be determined because the water droplet was readily absorbed.
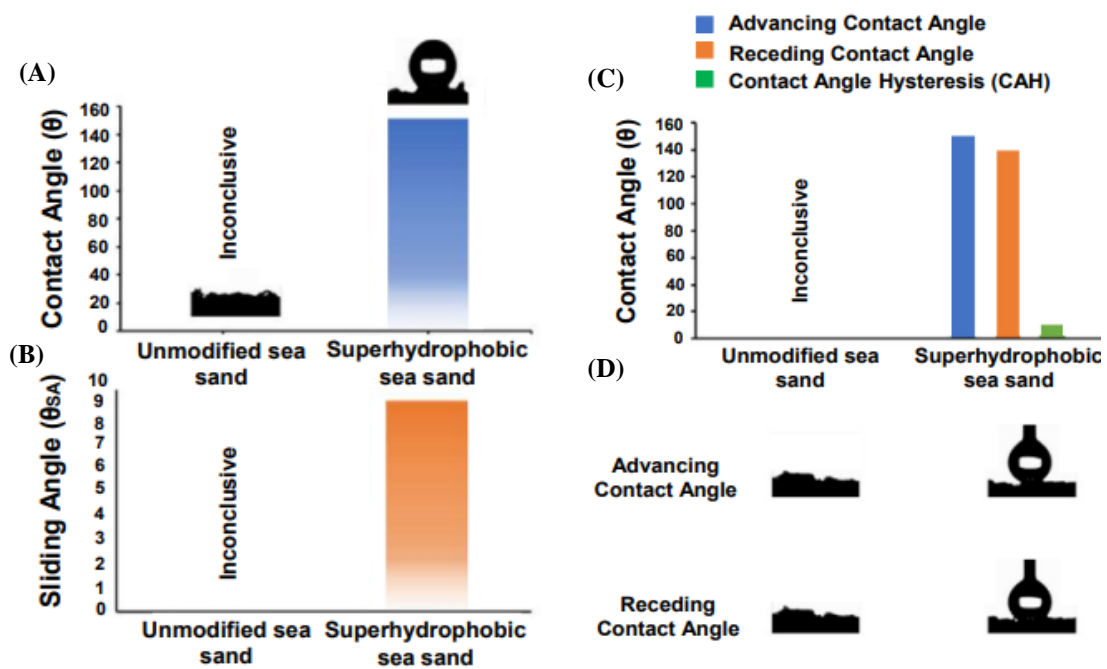
Figure 4.6: Analysis of wettability of unmodified and modified sea sand (A) the water contact angle (B) rolling-off angle (C) histogram representation of contact angle hysteresis of unmodified and modified sea sand (D) advancing and receding contact angles were measured applying the sessile drop technique. Reproduced with permission.[45] Copyright 2022, Elsevier.

75

Thus, the outcomes agree with those of previous studies in which water droplets immediately rolled off nanostructured surfaces, which lowered the surface energy by forming nanoscale air pocket.

Typically, the maximum contact angle is referred to as the advancing contact angle of a material, whereas the smallest contact angle is known as the receding contact angle.[114] The difference between the advancing and receding contact angles indicates contact angle hysteresis. Recent studies have demonstrated that the key sources of contact angle hysteresis are heterogeneity, surface roughness, and metastable surface states.[115, 116] In general, a superhydrophobic surface is non-adhesive and demonstrates extremely low water contact angle hysteresis. [28] A similar phenomenon can be observed in Figure 4.6 (C, D), where the contact angle hysteresis was measured for unmodified and modified SS. The modified SS showed an extremely low contact angle hysteresis value (11º), indicative of non-sticky and slippery surfaces. Furthermore, it is directly correlated with the rolling-off angle. Superhydrophobic SS with a minimum contact angle hysteresis possesses a self-cleaning tendency, whereby water droplets can readily slide off it. However, the contact angle hysteresis of unmodified SS, which absorbs water droplets, could not be readily determined.

4.3.5 Water Holding Capacity of Modified Sea Sand Grains

Toward addressing the concern of water loss in arid regions, the water-holding capacity of unmodified SS and SS-Si/FDTS was thoroughly investigated. As shown in Figure 4.7A, 3 mL of dyed water was immediately absorbed by the unmodified sand (left), whereas the colored water formed a stable water marble on the SS-Si/FDTS sand pit. This result indicates that superhydrophobic sand is impermeable to water and can thus potentially be utilized to reduce water loss from open water sources or stores in deserts and arid regions.
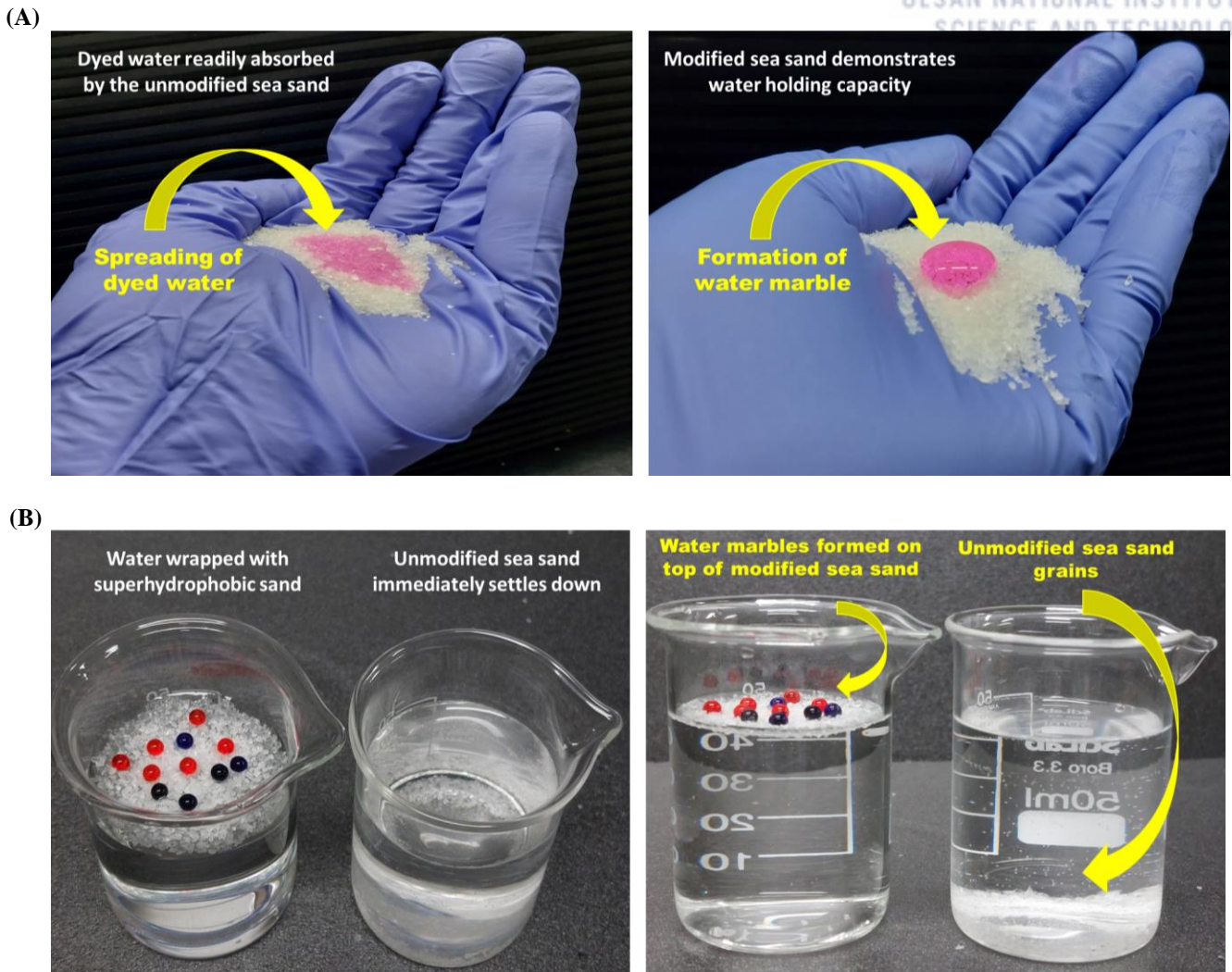
Figure 4.7: Experimental analysis of water holding and storage capacity: (A) Demonstration of water storage capacity of unmodified SS and SS-Si/FDTS. (B) Illustration of water holding and wrapping capacity of unmodified and modified SS. Reproduced with permission.[45] Copyright 2022, Elsevier.

Next, a simulated water source was well covered by superhydrophobic sea sand grains, as demonstrated in Figure 4.7B, to evaluate their ability to minimize evaporative water loss in arid and desert areas. A beaker was filled with 25 mL of deionized (DI) water, and the upper surface was covered with a thin layer of SS-Si/FDTS, which floated on the water because of its superhydrophobicity. In the other beaker, unmodified sand was added to the same amount of water, immediately settling to the bottom. Both beakers were kept undisturbed in while

measuring evaporative water loss. The results summarized in Table 4.1 show that water loss was negligible (12%) for the water source covered by the superhydrophobic sand. However, significant water loss (28.4%) was observed in the unmodified SS case. Thus, the overall outcomes suggest that water loss due to evaporation and percolation can be addressed by functionalized sand particles, and that this approach could be a fundamental research topic for improving agricultural productivity and water storage in desert areas.

In arid regions, acquiring fresh water is a major challenge because deep wells must be dug for underwater uptake.[117] Therefore, it is necessary to develop a sustainable method that allows the water source to remain on the sand surface. The production of hydrophobic sand is useful for both fundamental research and practical applications. Additionally, to obtain reliable water storage in desert regions, superhydrophobic modified sand can play a key role during water transportation. Thus, to confirm the flow-dragging mechanism of the fabricated sand, a simple experiment was conducted as a simulation of real conditions, whereby water droplets were poured onto unmodified and modified SS, and it showed that water holding and storage capacity of the modified SS, where water droplets remained smooth. However, the water droplets were immediately absorbed by the unmodified SS. Fundamentally, SS/desert sand is superhydrophilic in nature; thus, water storage and transportation are impractical. Therefore, the movie indicates the significance of superhydrophobic sand for applications such as water storage and transportation under harsh conditions in arid areas.

Thus, the overall outcomes suggest that water loss due to evaporation and percolation can be addressed by functionalizing sand particles in arid or desert areas.

Sand type	Status of sand	Initial volume of water at	Final volume of water at	Reduction in volume (mL)	% Volume evaporated

		DAY 1 (mL)	DAY 4 (mL)		
Unmodified Sand (SS)	Settled down immediately	25	17.9	7.1	28.4%
Modified sand (SS-Si/FDTS)	Formed a layer on top of the water source	25	22	3.0	12%

Table 4.1: Water storage capacity of modified sea sand. [Note: Conditions maintained: Temperature: 22ºC]. Reproduced with permission.[45] Copyright 2022, Elsevier.

Typically, sand particles and SS are exposed to various foulants and acid rain. Thus, the effectiveness of the hydrophobic coating may be minimized owing to fouling and the gradual loss of hydrophobic functional groups. Therefore, the robustness of the modified SS coating was carefully analyzed using an ultra-slow-motion camera and it showed a water droplet immediately rolling off the chemically functionalized SS particles, demonstrating their water repellence and superhydrophobic properties. Furthermore, self-cleaning behavior was evaluated by sliding a water droplet propelled by gravitational action over the modified sand. Dyed water droplets were dispensed onto SS-Si/FDTS, which were kept at a certain angle. Interestingly, the dyed water slid off immediately owing to the low-adhesion superhydrophobic surface of the modified SS, demonstrating an excellent lotus-like effect. Therefore, it can be concluded that the modified SS particles had a slippery surface and demonstrated antiwetting behavior.

4.3.6 Application of Superhydrophobic Engineered Nanomaterials on Regular Sand

A similar procedure was applied to regular sand (RS), which has the advantages of low cost, easy availability, and extremely high chemical stability, and its superhydrophobicity and water repellence properties were then evaluated. Dyed water droplets poured onto unmodified RS

were immediately absorbed by the sand surface, leading to a water contact angle of 0º. Thus,

unmodified RS demonstrated a low water holding capacity and water storage capacity.

However, contrasting effects were observed for modified RS (RS-Si/FDTS), where the dripped

(A) Unmodified Regular Sand (RS)

(B) Modified Regular Sand (RS-Si/FDTS)

Sand surface was remained dry indicating anti-wetting behavior

Water droplets permeate immediately indicating superhydrophilicity

Water droplets maintained spherical shaped marbles indicating superhydrophobicity
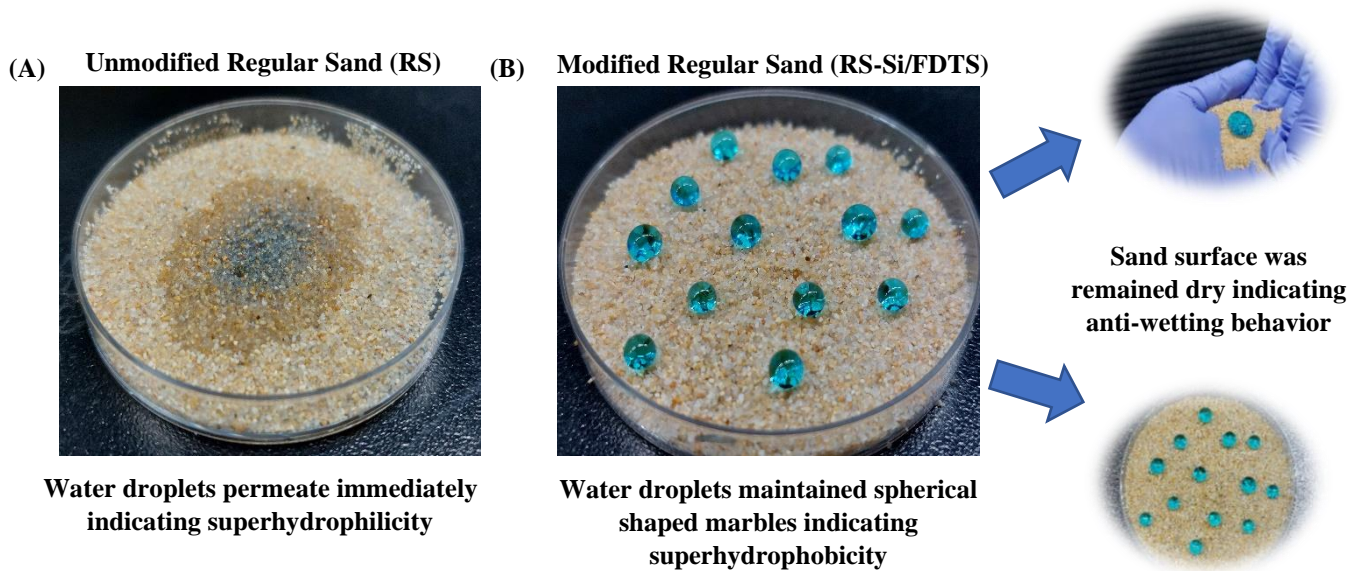
Figure 4.8: Superhydrophobic properties of regular sand (RS) (A) wetting of unmodified regular sand (B) anti-wetting properties of modified regular sand. Reproduced with permission.[45] Copyright 2022, Elsevier.

water droplets remained spherical. Furthermore, anti-wetting features can be observed in

Figure 4.8 because the sand layer remained dry without wetting the sand surface. The graphical

demonstration indicates durable water spheres capable of minimizing percolation and

evaporation rates in arid and semi-arid regions. Therefore, the overall results demonstrate the

effectiveness of superhydrophobic engineered nanomaterials (Si-NPs/FDTS) on various

(A)

Chloroform
(Absorbs immediately
demonstrating permeation)

Dyed Water
(Formation of water marbles
indicating capability of retaining
water)

(B)

STAGE -1

Dyed water

Chloroform

RS-Si/FDTS

Cotton

Time: 30 seconds

STAGE -2

Dyed water

RS-Si/FDTS

Cotton

Chloroform

Dyed water
maintained above
the filter

Cotton still maintained its
original colour indicating
no permeation of dyed
water

Clear chloroform can be
well observed

Time: 60 minutes

Figure 4.9: Oil/water separation application of superhydrophobic sand (A) Chloroform/water separation using RS-Si/FDTS as a filter (B) representation of retention of water droplets and permeation of chloroform using modified RS. Reproduced with permission.[45] Copyright 2022, Elsevier.

surfaces such as RS, which is commonly available worldwide. It is worth noting that Si-NP/FDTS can change the surface texture, providing a high-water contact angle and low rolling-

off angle. This combination of silica nanoparticles functionalization with FDTS can be used to transform a superhydrophilic surface to a superhydrophobic one.

4.3.7 Oil/water Separation Application

Overall, the experiments revealed that SS-Si/FDTS and RS-Si/FDTS are superhydrophobic and are suitable candidates for oil/water separation. The modified sand can readily repel water but becomes wet by oil. As shown in Figure 4.9, oil/water separation was performed for a mixture of chloroform and dyed water using 1 g of modified regular sand (RS-Si/FDTS) as a filter. As soon as the mixture of water and chloroform was poured into the funnel, chloroform started permeating immediately through the modified RS filter. This process was observed over 1 h. During the separation process, the chloroform permeated completely after 13 min. However, the dyed water did not permeate, as confirmed by the absence of color change in the cotton or by the transparent chloroform at the bottom of the conical flask. Therefore, the results indicate that a small amount of RS-Si/FDTS can effectively separate water and oil mixtures.

4.3.8 Abrasion test

The abrasion test with vigorous stirring of coated sand grains (SS-Si/FDTS and RS-Si/FDTS) in water has been performed for modified sand grains for evaluating the mechanical and chemical stability. The stirring continued for 120 min and then the sand grains were filtered and dried overnight. The modified sand grains were subjected to contact angle analysis to evaluate the change in hydrophobicity. However, negligible change in contact angle (0.99% and 0.72% respectively) has been observed indicating high mechanical and chemical stability of superhydrophobic coating of modified sea sand. Table 4.2 indicates the change in contact angle of the modified sea sand after the abrasion test.

Sand type	Duration of vigorous stirring (min)	Initial contact angle (θ)	Final contact angle after abrasion test (θ)	% Reduction of contact angle
Modified sea sand (SS-Si/FDTS)	120	151°	149.5°	0.993%
Modified regular sand (RS-Si/FDTS)	120	152.1°	151°	0.723%

Table 4.2: Abrasion test in terms of change in contact angle and sliding angle after vigorous stirring of sand grains. Reproduced with permission.[45] Copyright 2022, Elsevier.

Chapter 5

Conclusion and future work

5.1 Conclusion

In the first part of the thesis, our study demonstrates a technological advancement in the development of reusable surgical masks during pandemic times. The present study shows that the commercially available surgical masks have poor hydrophobicity and low capacity to kill bacteria and viruses. We developed a simple method of coating SWCNTs on the pristine PP fibers of surgical masks. The CNT-coated mask exhibits outstanding superhydrophobicity and striking photothermal response, and hence antimicrobial and antiviral properties. The present study demonstrates the excellent photothermal response and superhydrophobicity of CNT-coated masks, which can provide better protection from incoming virus- or bacteria-containing respiratory droplets and enable rapid sterilization of the surface containing viruses and bacteria under solar illumination. To the best of our knowledge, there are no previous studies that utilize the spray coating of SWCNTs on the PP fibers of the surgical mask, which makes the mask surface superhydrophobic, photothermal, bactericidal, virucidal, and electrothermal. According to the World Health Organization, discarded masks can become a source for rapid spread of viral infection. Therefore, reusable masks that can be easily decontaminated or have antimicrobial and virucidal properties can serve as a sustainable prevention tool against the rapid spread of viruses while abating the economic and environmental costs.

In the second part of the thesis, a superhydrophobic coating that possesses high durability and anti-droplet behavior and can be applied using various techniques on different substrate materials. The SSO coating has been successfully developed by using facile, eco-friendly,

versatile, economical, and scalable methods. The nanocoating was prepared by using shellac bio adhesive and silica nanoparticles modified with octadecyltricholosilane. This simple approach eliminated many limitations of present waterproof coating methods, such as expensive materials, environmental hazardous, and time-consuming preparation processes. Furthermore, the versatility of the SSO coating enables the possibility of utilizing the uniform surface coating over various solid and porous substrates, regardless of their different surface morphology and sample dimension. It was found that the bio adhesive based nanocoating successfully increases the contact angle from 119.7±1.5 ˚, 39.6±2.3 ˚, 72.3±2.3 ˚ to 162.1±3.2 ˚, 160.2±4.4 ˚, 151.3±3.3 ˚ for pp, glass, and pet respectively. Contact angle hysteresis studies prove the low water droplet adhesion behavior for SSO coated surfaces. The coating shows anti-wetting behavior for acid rain and exhibits self-cleaning properties against organic pollutants such as methylene blue. More interestingly, the SSO coated substrates exhibited excellent mechanical durability against strong abrasion cycles and maintained superhydrophobic under high temperature conditions also. This outstanding performance accomplished encourages the widespread utilization of superhydrophobic surface for various applications.

In the third part of the thesis, the functionalization of sand grains with stable superhydrophobic coatings is a prominent challenge. Sand grains were modified with a well-adhered and durable superhydrophobic coating. Thus, superhydrophobic sand grains offer a revolutionary solution for arid land agriculture with inadequate water resources. The coating was derived from hydrophobic Si NPs modified with hydrolyzed FDTS. Si/FDTS-coated sand grains demonstrated highly stable superhydrophobic features with an average contact angle of 151° Interestingly, and water droplets rolled off the functionalized sea sand grains and were not absorbed. The treatment of sand grains with Si/FDTS resulted in a lower sliding angle of 9.5°,

imparting self-cleaning capabilities and higher hydrophobic efficiency. The modified sea sand grains demonstrated excellent water holding and storage capabilities in long-term experiments, which could be harnessed to improve agriculture in arid regions. Herein, superhydrophobic sand grains were fabricated via a one-step dip coating technique with advantages of manual application and low operational costs. Thus, it can be concluded that the present research study can play a key role in expanding sustainable agricultural technology relying on limited water sources, including China, India, African countries, and Middle East countries.

5. 2 Future Work

The wide range of superhydrophobic surface coatings topics covered in this thesis research gives the potential for more studies to enhance the outcome of the research. Additionally, other factors can be considered for feasible use of the superhydrophobic coatings for real-life applications.

There is a need to develop a low-cost, highly durable and transparent superhydrophobic materials-based coating to have a wide range of possible daily use applications. We intend to further this study and development for a transparent, low-cost, with high durability to use it for anti-icing properties energy (solar panels, wind turbine), aircraft, sea ships, and automobile (cars) based industrial applications.

Healthcare is another area of interest where these bio-compatible superhydrophobic coatings can be used for encapsulation of soft robots to advancement of medical surgeries. Soft robotics is a very popular field now days due to many potential applications for betterment of humanity and there is a huge scope to use these kinds of protective coatings. We are interested in further development of biomaterials-based coatings to make it feasible to use for smart medical surgical applications.

References

(1) Camaiti, M.; Brizi, L.; Bortolotti, V.; Papacchini, A.; Salvini, A.; Fantazzini, P. An Environmental Friendly Fluorinated Oligoamide for Producing Nonwetting Coatings with High Performance on Porous Surfaces. *ACS Appl Mater Interfaces* **2017**, *9* (42), 37279-37288. DOI: 10.1021/acsami.7b09440

(2) Gerasopoulos, K.; Luedeman, W. L.; Olceroglu, E.; McCarthy, M.; Benkoski, J. J. Effects of Engineered Wettability on the Efficiency of Dew Collection. *ACS Appl Mater Interfaces* **2018**, *10* (4), 4066-4076. DOI: 10.1021/acsami.7b16379

(3) Mondal, B.; Mac Giolla Eain, M.; Xu, Q.; Egan, V. M.; Punch, J.; Lyons, A. M. Design and Fabrication of a Hybrid Superhydrophobic-Hydrophilic Surface That Exhibits Stable Dropwise Condensation. *ACS Appl Mater Interfaces* **2015**, *7* (42), 23575-23588. DOI: 10.1021/acsami.5b06759

(4) Yasmin A. Mehanna, E. S., Rebekah L. Upton, Andrew G. Kempchinsky, Yao Lu c and Colin R. Crick The challenges, achievements and applications of submersible superhydrophobic materials. *Chem. Soc. Rev* **2021**, *50*, 6569–6612. DOI: 10.1039/d0cs01056a

(5) Liu, Y.; Chen, J.; Guo, D.; Cao, M.; Jiang, L. Floatable, Self-Cleaning, and Carbon-Black-Based Superhydrophobic Gauze for the Solar Evaporation Enhancement at the Air-Water Interface. *ACS Appl Mater Interfaces* **2015**, *7* (24), 13645-13652. DOI: 10.1021/acsami.5b03435

(6) Sun, K.; Yang, H.; Xue, W.; He, A.; Zhu, D.; Liu, W.; Adeyemi, K.; Cao, Y. Anti-biofouling superhydrophobic surface fabricated by picosecond laser texturing of stainless steel. *Applied Surface Science* **2018**, *436*, 263-267. DOI: 10.1016/j.apsusc.2017.12.012

(7) Bixler, G. D.; Bhushan, B. Fluid Drag Reduction with Shark-Skin Riblet Inspired Microstructured Surfaces. *Advanced Functional Materials* **2013**, *23* (36), 4507-4528. DOI: 10.1002/adfm.201203683

(8) Jamil, M. I.; Ali, A.; Haq, F.; Zhang, Q.; Zhan, X.; Chen, F. Icephobic Strategies and Materials with Superwettability: Design Principles and Mechanism. *Langmuir* **2018**, *34* (50), 15425-15444. DOI: 10.1021/acs.langmuir.8b03276

(9) Soni, R.; Joshi, S. R.; Karmacharya, M.; Min, H.; Kim, S.-K.; Kumar, S.; Kim, G.-H.; Cho, Y.-K.; Lee, C. Y. Superhydrophobic and Self-Sterilizing Surgical Masks Spray-Coated with Carbon Nanotubes. *ACS Applied Nano Materials* **2021**, *4* (8), 8491-8499. DOI: 10.1021/acsanm.1c01082

(10) Sun, Z.; Liao, T.; Liu, K.; Jiang, L.; Kim, J. H.; Dou, S. X. Fly-eye inspired superhydrophobic anti-fogging inorganic nanostructures. *Small* **2014**, *10* (15), 3001-3006. DOI: 10.1002/smll.201400516

(11) de Leon, A. C.; Pernites, R. B.; Advincula, R. C. Superhydrophobic colloidally textured polythiophene film as superior anticorrosion coating. *ACS Appl Mater Interfaces* **2012**, *4* (6), 3169-3176. DOI: 10.1021/am300513e

(12) Yue, X.; Li, J.; Zhang, T.; Qiu, F.; Yang, D.; Xue, M. In situ one-step fabrication of durable superhydrophobic-superoleophilic cellulose/LDH membrane with hierarchical structure for efficiency oil/water separation. *Chemical Engineering Journal* **2017**, *328*, 117-123. DOI: 10.1016/j.cej.2017.07.026

(13) Zhang, P.; Lv, F. Y. A review of the recent advances in superhydrophobic surfaces and the emerging energy-related applications. *Energy* **2015**, *82*, 1068-1087. DOI: 10.1016/j.energy.2015.01.061

(14) Manoudis, P. N.; Tsakalof, A.; Karapanagiotis, I.; Zuburtikudis, I.; Panayiotou, C. Fabrication of super-hydrophobic surfaces for enhanced stone protection. *Surface and Coatings Technology* **2009**, *203* (10-11), 1322-1328. DOI: 10.1016/j.surfcoat.2008.10.041

(15) Gallo, A.; Odokonyero, K.; Mousa, M. A. A.; Reihmer, J.; Al-Mashharawi, S.; Marasco, R.; Manalastas, E.; Morton, M. J. L.; Daffonchio, D.; McCabe, M. F.; et al. Nature-Inspired Superhydrophobic Sand Mulches Increase Agricultural Productivity and Water-Use Efficiency in Arid Regions. *ACS Agricultural Science & Technology* **2022**, *2* (2), 276-288. DOI: 10.1021/acsagscitech.1c00148

(16) Amabili, M.; Giacomello, A.; Meloni, S.; Casciola, C. M. Unraveling the Salvinia Paradox: Design Principles for Submerged Superhydrophobicity. *Advanced Materials Interfaces* **2015**, *2* (14). DOI: 10.1002/admi.201500248

(17) Barthlott, W.; Schimmel, T.; Wiersch, S.; Koch, K.; Brede, M.; Barczewski, M.; Walheim, S.; Weis, A.; Kaltenmaier, A.; Leder, A.; et al. The salvinia paradox: superhydrophobic surfaces with hydrophilic pins for air retention under water. *Adv Mater* **2010**, *22* (21), 2325-2328. DOI: 10.1002/adma.200904411

(18) Feng, X. J.; Jiang, L. Design and Creation of Superwetting/Antiwetting Surfaces. *Advanced Materials* **2006**, *18* (23), 3063-3078. DOI: 10.1002/adma.200501961

(19) Xuefeng Gao, L. J. Water-repellent legs of water striders. *Nature* **2004**, *432*, 1.

(20) Bhushan, B.; Jung, Y. C. Natural and biomimetic artificial surfaces for superhydrophobicity, self-cleaning, low adhesion, and drag reduction. *Progress in Materials Science* **2011**, *56* (1), 1-108. DOI: 10.1016/j.pmatsci.2010.04.003

(21) Koch, K.; Bhushan, B.; Barthlott, W. Multifunctional surface structures of plants: An inspiration for biomimetics. *Progress in Materials Science* **2009**, *54* (2), 137-178. DOI: 10.1016/j.pmatsci.2008.07.003

(22) Carbone, G.; Mangialardi, L. Hydrophobic properties of a wavy rough substrate. *Eur Phys J E Soft Matter* **2005**, *16* (1), 67-76. DOI: 10.1140/epje/e2005-00008-y From NLM Medline.

(23) Avramescu, R. E.; Ghica, M. V.; Dinu-Pirvu, C.; Prisada, R.; Popa, L. Superhydrophobic Natural and Artificial Surfaces-A Structural Approach. *Materials (Basel)* **2018**, *11* (5). DOI: 10.3390/ma11050866

(24) Verplanck, N.; Coffinier, Y.; Thomy, V.; Boukherroub, R. Wettability Switching Techniques on Superhydrophobic Surfaces. *Nanoscale Research Letters* **2007**, *2* (12). DOI: 10.1007/s11671-007-9102-4

(25) Ueda, E.; Levkin, P. A. Emerging applications of superhydrophilic-superhydrophobic micropatterns. *Adv Mater* **2013**, *25* (9), 1234-1247. DOI: 10.1002/adma.201204120

(26) Eral, H. B.; 't Mannetje, D. J. C. M.; Oh, J. M. Contact angle hysteresis: a review of fundamentals and applications. *Colloid and Polymer Science* **2012**, *291* (2), 247-260. DOI: 10.1007/s00396-012-2796-6

(27) Sinha Ray, S.; Lee, H. K.; Huyen, D. T. T.; Park, Y.-I.; Park, H.; Nam, S.-E.; Kim, I.-C.; Kwon, Y.-N. Fluorine-free anti-droplet surface modification by hexadecyltrimethoxysilane-modified silica nanoparticles-coated carbon nanofibers for self-cleaning applications. *Progress in Organic Coatings* **2021**, *153*. DOI: 10.1016/j.porgcoat.2021.106165

(28) Zhu, J.; Dai, X. A new model for contact angle hysteresis of superhydrophobic surface. *AIP Advances* **2019**, *9* (6). DOI: 10.1063/1.5100548

(29) Murakami, D.; Jinnai, H.; Takahara, A. Wetting transition from the Cassie-Baxter state to the Wenzel state on textured polymer surfaces. *Langmuir* **2014**, *30* (8), 2061-2067. DOI: 10.1021/la4049067

(30) BAXTER, A. B. D. C. A. S. Wettabilty of Porous Surfaces *Trans. Faraday Soc.* **1944**, 6.

(31) Callies, M.; Quéré, D. On water repellency. *Soft Matter* **2005**, *1* (1). DOI: 10.1039/b501657f

(32) Xiao Wang, C. F., Chunlai Zhang, Zhengyao Qiu and Bo Wang. A Comprehensive Review of Wetting Transition Mechanism on the Surfaces of Microstructures from Theory and Testing Methods. *Materials (Basel)* **2022**, *15*, 4747-4767. DOI: https://doi.org/10.3390/ma15144747

(33) WENZEL, R. N. Resistane of Solid Surfaces to Wetting by Water. *INDUSTRIAL AND ENGINEERING CHEMISTRY* **1936**, 7.

(34) CASSIE, A. B. D. Contact Angles. **1948**, 6.

(35) Pozzato, A.; Zilio, S. D.; Fois, G.; Vendramin, D.; Mistura, G.; Belotti, M.; Chen, Y.; Natali, M. Superhydrophobic surfaces fabricated by nanoimprint lithography. *Microelectronic Engineering* **2006**, *83* (4-9), 884-888. DOI: 10.1016/j.mee.2006.01.012

(36) Feng, J.; Tuominen, M. T.; Rothstein, J. P. Hierarchical Superhydrophobic Surfaces Fabricated by Dual-Scale Electron-Beam-Lithography with Well-Ordered Secondary Nanostructures. *Advanced Functional Materials* **2011**, *21* (19), 3715-3722. DOI: 10.1002/adfm.201100665

(37) Roach, P.; Shirtcliffe, N. J.; Newton, M. I. Progess in superhydrophobic surface development. *Soft Matter* **2008**, *4* (2), 224-240. DOI: 10.1039/b712575p

(38) Zhang, Y.; Zhang, Z.; Yang, J.; Yue, Y.; Zhang, H. A Review of Recent Advances in Superhydrophobic Surfaces and Their Applications in Drag Reduction and Heat Transfer. *Nanomaterials (Basel)* **2021**, *12* (1). DOI: 10.3390/nano12010044

(39) Kim, J.-H.; Mirzaei, A.; Kim, H. W.; Kim, S. S. Facile fabrication of superhydrophobic surfaces from austenitic stainless steel (AISI 304) by chemical etching. *Applied Surface Science* **2018**, *439*, 598-604. DOI: 10.1016/j.apsusc.2017.12.211

(40) Kang, B.; Sung, J.; So, H. Realization of Superhydrophobic Surfaces Based on Three-Dimensional Printing Technology. *International Journal of Precision Engineering and Manufacturing-Green Technology* **2019**, *8* (1), 47-55. DOI: 10.1007/s40684-019-00163-9

(41) JOHN M. BLOCHER, J. Chemical Vapor Deposition for Surface Conditioning: Opportunities and Cautions*. *Materials Science and Engineering* **1988**, 435-441.

(42) YI ZHANG, L. Z., CHONGWU ZHOU. Review of Chemical Vapor Deposition of Graphene and Related Applications. *ACCOUNTS OF CHEMICAL RESEARCH* **2012**, *46*, 2329–2339.

(43) Huang, X.; Sun, M.; Shi, X.; Shao, J.; Jin, M.; Liu, W.; Zhang, R.; Huang, S.; Ye, Y. Chemical vapor deposition of transparent superhydrophobic anti-Icing coatings with tailored polymer nanoarray architecture. *Chemical Engineering Journal* **2023**, *454*. DOI: 10.1016/j.cej.2022.139981

(44) Saikat Sinha Ray, P. R. T. P., Ritesh Soni, Byungmin Kim, You-In Park, In-Chul Kim, Chang Young Lee and Young-Nam Kwon Effectiveness of nanoparticles-based ultrahydrophobic coating for concrete materials. *Journal of Building Engineering* **2023**, *66*, 105799-105814.

(45) Saikat Sinha Ray, R. Soni, In-Chul Kim, You-In Park, Chang Young Lee and Young-Nam Kwon. Surface innovation for fabrication of superhydrophobic sand grains with improved water holding capacity for various environmental applications. *Environmental Technology & Innovation* **2022**, *28*, 102849-102861.

(46) Bayer, I. On the Durability and Wear Resistance of Transparent Superhydrophobic Coatings. *Coatings* **2017**, *7* (1). DOI: 10.3390/coatings7010012

(47) Wang, H.; Xue, Y.; Ding, J.; Feng, L.; Wang, X.; Lin, T. Durable, self-healing superhydrophobic and superoleophobic surfaces from fluorinated-decyl polyhedral oligomeric

silsesquioxane and hydrolyzed fluorinated alkyl silane. *Angew Chem Int Ed Engl* **2011**, *50* (48), 11433-11436. DOI: 10.1002/anie.201105069

(48) Zen Yoshimitsu, A. N., Toshiya Watanabe, Kazuhito Hashimoto. Effects of Surface Structure on the Hydrophobicity and Sliding Behavior of Water Droplets. *Langmuir* **2002**, *18*, 5818-5822.

(49) Mehanna, Y. A.; Sadler, E.; Upton, R. L.; Kempchinsky, A. G.; Lu, Y.; Crick, C. R. The challenges, achievements and applications of submersible superhydrophobic materials. *Chem Soc Rev* **2021**, *50* (11), 6569-6612. DOI: 10.1039/d0cs01056a

(50) Yao Lu, S. S., Jinlong Song, Colin R. Crick, Claire J. Carmalt, Ivan P. Parkin. Robust self-cleaning surfaces thatfunction when exposed to eitherair or oil. *Science* **2015**, *347*, 1132-1135.

(51) Li, J.; Sun, J.; Li, P. Exposure routes, bioaccumulation and toxic effects of per- and polyfluoroalkyl substances (PFASs) on plants: A critical review. *Environ Int* **2022**, *158*, 106891. DOI: 10.1016/j.envint.2021.106891

(52) Jafari, R.; Cloutier, C.; Allahdini, A.; Momen, G. Recent progress and challenges with 3D printing of patterned hydrophobic and superhydrophobic surfaces. *The International Journal of Advanced Manufacturing Technology* **2019**, *103* (1-4), 1225-1238. DOI: 10.1007/s00170-019-03630-4.

(53) Kim, S.; Lee, J. W.; Hwang, W. One-Step Eco-Friendly Superhydrophobic Coating Method Using Polydimethylsiloxane and Ammonium Bicarbonate. *ACS Appl Mater Interfaces* **2020**, *12* (25), 28869-28875. DOI: 10.1021/acsami.0c06697

(54) Zao Chen, X. L., Yan Wang, Jun Li, Zisheng Guan. Highly transparent, stable, and superhydrophobic coatings based on gradient structure design and fast regeneration from physical damage. *Applied Surface Science* **2015**, *359*, 826–833. DOI: 10.1016/j.apsusc.2015.10.150

(55) Sotoudeh, F.; Mousavi, S. M.; Karimi, N.; Lee, B. J.; Abolfazli-Esfahani, J.; Manshadi, M. K. D. Natural and synthetic superhydrophobic surfaces: A review of the fundamentals, structures, and applications. *Alexandria Engineering Journal* **2023**, *68*, 587-609. DOI: 10.1016/j.aej.2023.01.058

(56) *WORLDOMETER*.

(57) WHO.

(58) Lai, C. C.; Shih, T. P.; Ko, W. C.; Tang, H. J.; Hsueh, P. R. Severe acute respiratory syndrome coronavirus 2 (SARS-CoV-2) and coronavirus disease-2019 (COVID-19): The epidemic and the challenges. *Int J Antimicrob Agents* **2020**, *55* (3), 105924. DOI: 10.1016/j.ijantimicag.2020.105924

(59) Wang, H.; Wang, Z.; Dong, Y.; Chang, R.; Xu, C.; Yu, X.; Zhang, S.; Tsamlag, L.; Shang, M.; Huang, J.; et al. Phase-adjusted estimation of the number of Coronavirus Disease 2019 cases in Wuhan, China. *Cell Discov* **2020**, *6*, 10. DOI: 10.1038/s41421-020-0148-0

(60) Workman, A. D.; Welling, D. B.; Carter, B. S.; Curry, W. T.; Holbrook, E. H.; Gray, S. T.; Scangas, G. A.; Bleier, B. S. Endonasal instrumentation and aerosolization risk in the era of COVID-19: simulation, literature review, and proposed mitigation strategies. *Int Forum Allergy Rhinol* **2020**, *10* (7), 798-805. DOI: 10.1002/alr.22577

(61) Wu, F.; Zhao, S.; Yu, B.; Chen, Y. M.; Wang, W.; Song, Z. G.; Hu, Y.; Tao, Z. W.; Tian, J. H.; Pei, Y. Y.; et al. A new coronavirus associated with human respiratory disease in China. *Nature* **2020**, *579* (7798), 265-269. DOI: 10.1038/s41586-020-2008-3

(62) Alam, Q.; Schollbach, K.; Rijnders, M.; van Hoek, C.; van der Laan, S.; Brouwers, H. J. H. The immobilization of potentially toxic elements due to incineration and weathering of bottom ash fines. *J Hazard Mater* **2019**, *379*, 120798. DOI: 10.1016/j.jhazmat.2019.120798

(63) El-Atab, N.; Qaiser, N.; Badghaish, H.; Shaikh, S. F.; Hussain, M. M. Flexible Nanoporous Template for the Design and Development of Reusable Anti-COVID-19 Hydrophobic Face Masks. *ACS Nano* **2020**, *14* (6), 7659-7665. DOI: 10.1021/acsnano.0c03976

(64) Leung, N. H. L.; Chu, D. K. W.; Shiu, E. Y. C.; Chan, K. H.; McDevitt, J. J.; Hau, B. J. P.; Yen, H. L.; Li, Y.; Ip, D. K. M.; Peiris, J. S. M.; et al. Respiratory virus shedding in exhaled breath and efficacy of face masks. *Nat Med* **2020**, *26* (5), 676-680. DOI: 10.1038/s41591-020-0843-2

(65) Hongqing Shen, K. K. L. Study of Repellent Finish of Filtration Ability of Surgical Face Masks. *INJ* **2005**, 1-10.

(66) Leung, C. C.; Lam, T. H.; Cheng, K. K. Mass masking in the COVID-19 epidemic: people need guidance. *Lancet* **2020**, *395* (10228), 945. DOI: 10.1016/S0140-6736(20)30520-1

(67) Majchrzycka, K.; Okrasa, M.; Szulc, J.; Jachowicz, A.; Gutarowska, B. Survival of Microorganisms on Nonwovens Used for the Construction of Filtering Facepiece Respirators. *Int J Environ Res Public Health* **2019**, *16* (7). DOI: 10.3390/ijerph16071154

(68) Megan L. Ranney, Valerie Griffeth, Ashish K. Jha. Critical Supply Shortages - The Need for Ventilators and Personal Protective Equipment During the Covid-19 Pandemic. *The NEW ENGLAND JOURNAL of MEDICINE* **2020**, e41(41).

(69) Journet, C.; Moulinet, S.; Ybert, C.; Purcell, S. T.; Bocquet, L. Contact angle measurements on superhydrophobic carbon nanotube forests: Effect of fluid pressure. *Europhysics Letters (EPL)* **2005**, *71* (1), 104-109. DOI: 10.1209/epl/i2005-10068-4

(70) Chang, D.; Xu, H.; Rebaza, A.; Sharma, L.; Dela Cruz, C. S. Protecting health-care workers from subclinical coronavirus infection. *Lancet Respir Med* **2020**, *8* (3), e13. DOI: 10.1016/S2213-2600(20)30066-7

(71) Kidd-Ljunggren, K.; Holmberg, A.; Blackberg, J.; Lindqvist, B. High levels of hepatitis B virus DNA in body fluids from chronic carriers. *J Hosp Infect* **2006**, *64* (4), 352-357. DOI: 10.1016/j.jhin.2006.06.029

(72) Mohseni, A. H.; Taghinezhad, S. S.; Xu, Z.; Fu, X. Body fluids may contribute to human-to-human transmission of severe acute respiratory syndrome coronavirus 2: evidence and practical experience. *Chin Med* **2020**, *15*, 58. DOI: 10.1186/s13020-020-00337-7

(73) Tarantola, A.; Abiteboul, D.; Rachline, A. Infection risks following accidental exposure to blood or body fluids in health care workers: a review of pathogens transmitted in published cases. *Am J Infect Control* **2006**, *34* (6), 367-375. DOI: 10.1016/j.ajic.2004.11.011

(74) Huang, N.; Wang, H.; Zhao, J.; Lui, H.; Korbelik, M.; Zeng, H. Single-wall carbon nanotubes assisted photothermal cancer therapy: animal study with a murine model of squamous cell carcinoma. *Lasers Surg Med* **2010**, *42* (9), 638-648. DOI: 10.1002/lsm.20968

(75) Meng, L.; Xia, W.; Liu, L.; Niu, L.; Lu, Q. Golden single-walled carbon nanotubes prepared using double layer polysaccharides bridge for photothermal therapy. *ACS Appl Mater Interfaces* **2014**, *6* (7), 4989-4996. DOI: 10.1021/am406031n

(76) Zhou, F.; Xing, D.; Ou, Z.; Wu, B.; Resasco, D. E.; Chen, W. R. Cancer photothermal therapy in the near-infrared region by using single-walled carbon nanotubes. *J Biomed Opt* **2009**, *14* (2), 021009. DOI: 10.1117/1.3078803

(77) Huang, L.; Xu, S.; Wang, Z.; Xue, K.; Su, J.; Song, Y.; Chen, S.; Zhu, C.; Tang, B. Z.; Ye, R. Self-Reporting and Photothermally Enhanced Rapid Bacterial Killing on a Laser-Induced Graphene Mask. *ACS Nano* **2020**, *14* (9), 12045-12053. DOI: 10.1021/acsnano.0c05330

(78) Yang, P.; Wang, X. COVID-19: a new challenge for human beings. *Cell Mol Immunol* **2020**, *17* (5), 555-557. DOI: 10.1038/s41423-020-0407-x

(79) Zhou, P.; Yang, X. L.; Wang, X. G.; Hu, B.; Zhang, L.; Zhang, W.; Si, H. R.; Zhu, Y.; Li, B.; Huang, C. L.; et al. A pneumonia outbreak associated with a new coronavirus of probable bat origin. *Nature* **2020**, *579* (7798), 270-273. DOI: 10.1038/s41586-020-2012-7

(80) Nolte-'t Hoen, E.; Cremer, T.; Gallo, R. C.; Margolis, L. B. Extracellular vesicles and viruses: Are they close relatives? *Proc Natl Acad Sci U S A* **2016**, *113* (33), 9155-9161. DOI: 10.1073/pnas.1605146113

(81) Panigaj, M.; Johnson, M. B.; Ke, W.; McMillan, J.; Goncharova, E. A.; Chandler, M.; Afonin, K. A. Aptamers as Modular Components of Therapeutic Nucleic Acid Nanotechnology. *ACS Nano* **2019**, *13* (11), 12301-12321. DOI: 10.1021/acsnano.9b06522

(82) Raab-Traub, N.; Dittmer, D. P. Viral effects on the content and function of extracellular vesicles. *Nat Rev Microbiol* **2017**, *15* (9), 559-572. DOI: 10.1038/nrmicro.2017.60

(83) Kumar, S.; Karmacharya, M.; Joshi, S. R.; Gulenko, O.; Park, J.; Kim, G. H.; Cho, Y. K. Photoactive Antiviral Face Mask with Self-Sterilization and Reusability. *Nano Lett* **2021**, *21* (1), 337-343. DOI: 10.1021/acs.nanolett.0c03725

(84) Jeevahan, J.; Chandrasekaran, M.; Britto Joseph, G.; Durairaj, R. B.; Mageshwaran, G. Superhydrophobic surfaces: a review on fundamentals, applications, and challenges. *Journal of Coatings Technology and Research* **2018**, *15* (2), 231-250. DOI: 10.1007/s11998-017-0011-x.

(85) Martin, S.; Brown, P. S.; Bhushan, B. Fabrication techniques for bioinspired, mechanically-durable, superliquiphobic surfaces for water, oil, and surfactant repellency. *Adv Colloid Interface Sci* **2017**, *241*, 1-23. DOI: 10.1016/j.cis.2017.01.004

(86) Allione, M.; Limongi, T.; Marini, M.; Torre, B.; Zhang, P.; Moretti, M.; Perozziello, G.; Candeloro, P.; Napione, L.; Pirri, C. F.; et al. Micro/Nanopatterned Superhydrophobic Surfaces

Fabrication for Biomolecules and Biomaterials Manipulation and Analysis. *Micromachines (Basel)* **2021**, *12* (12). DOI: 10.3390/mi12121501

(87) Elzaabalawy, A.; Meguid, S. A. Development of novel superhydrophobic coatings using siloxane-modified epoxy nanocomposites. *Chemical Engineering Journal* **2020**, *398*. DOI: 10.1016/j.cej.2020.125403

(88) Li, K.; Zeng, X.; Li, H.; Lai, X.; Ye, C.; Xie, H. Study on the wetting behavior and theoretical models of polydimethylsiloxane/silica coating. *Applied Surface Science* **2013**, *279*, 458-463. DOI: 10.1016/j.apsusc.2013.04.137

(89) Elzaabalawy, A.; Verberne, P.; Meguid, S. A. Multifunctional Silica-Silicone Nanocomposite with Regenerative Superhydrophobic Capabilities. *ACS Appl Mater Interfaces* **2019**, *11* (45), 42827-42837. DOI: 10.1021/acsami.9b15445

(90) Bayer, I. S.; Steele, A.; Loth, E. Superhydrophobic and electroconductive carbon nanotube-fluorinated acrylic copolymer nanocomposites from emulsions. *Chemical Engineering Journal* **2013**, *221*, 522-530. DOI: 10.1016/j.cej.2013.01.023

(91) Su, B.; Tian, Y.; Jiang, L. Bioinspired Interfaces with Superwettability: From Materials to Chemistry. *J Am Chem Soc* **2016**, *138* (6), 1727-1748. DOI: 10.1021/jacs.5b12728

(92) Patel, A. R. Functional and Engineered Colloids from Edible Materials for Emerging Applications in Designing the Food of the Future. *Advanced Functional Materials* **2018**, *30* (18). DOI: 10.1002/adfm.201806809

(93) Yuan, Y.; He, N.; Dong, L.; Guo, Q.; Zhang, X.; Li, B.; Li, L. Multiscale Shellac-Based Delivery Systems: From Macro- to Nanoscale. *ACS Nano* **2021**, *15* (12), 18794-18821. DOI: 10.1021/acsnano.1c07121

(94) Sagiv, J. Formation and Structure of Oleophobic Mixed Monolayers on Solid-Surfaces. *Journal of the American Chemical Society* **1978**, 92-98. DOI: 10.1021/ja00521a016

(95) Zhang, L.; Zhou, A. G.; Sun, B. R.; Chen, K. S.; Yu, H. Z. Functional and versatile superhydrophobic coatings via stoichiometric silanization. *Nat Commun* **2021**, *12* (1), 982. DOI: 10.1038/s41467-021-21219-y

(96) Wang, J.; He, L.; Pan, A.; Zhao, Y. Hydrophobic and Durable Adhesive Coatings Fabricated from Fluorinated Glycidyl Copolymers Grafted on SiO2 Nanoparticles. *ACS Applied Nano Materials* **2018**, *2* (1), 617-626. DOI: 10.1021/acsanm.8b02283

(97) Shen, Y.; Wu, Z.; Tao, J.; Jia, Z.; Chen, H.; Liu, S.; Jiang, J.; Wang, Z. Spraying Preparation of Eco-Friendly Superhydrophobic Coatings with Ultralow Water Adhesion for Effective Anticorrosion and Antipollution. *ACS Appl Mater Interfaces* **2020**, *12* (22), 25484-25493. DOI: 10.1021/acsami.0c06074

(98) Zhang, J.; Lin, W.; Zhu, C.; Lv, J.; Zhang, W.; Feng, J. Dark, Infrared Reflective, and Superhydrophobic Coatings by Waterborne Resins. *Langmuir* **2018**, *34* (19), 5600-5605. DOI: 10.1021/acs.langmuir.8b00929

(99) Cappelletti, G.; Fermo, P.; Camiloni, M. Smart hybrid coatings for natural stones conservation. *Progress in Organic Coatings* **2015**, *78*, 511-516. DOI: 10.1016/j.porgcoat.2014.05.029

(100) Tu, K.; Wang, X.; Kong, L.; Guan, H. Facile preparation of mechanically durable, self-healing and multifunctional superhydrophobic surfaces on solid wood. *Materials & Design* **2018**, *140*, 30-36. DOI: 10.1016/j.matdes.2017.11.029

(101) Wang, Y.; Kang, L.; Li, Z.; Su, Q.; Pang, S.; Liang, L.; Wang, D.; Cao, S. Preparation and Self-Cleaning Performance of Carbon-Based Superhydrophobic Coatings Based on Non-Fluorine and Non-Toxic Corn Straw. *Molecules* **2021**, *26* (21). DOI: 10.3390/molecules26216401

(102) Heyns, P. Water conservation in arid and semi-arid regions. *WATER RESOURCES MANAGEMENT 1*, 1-10.

(103) Gong, D.; Mei, X.; Hao, W.; Wang, H.; Caylor, K. K. Comparison of ET partitioning and crop coefficients between partial plastic mulched and non-mulched maize fields. *Agricultural Water Management* **2017**, *181*, 23-34. DOI: 10.1016/j.agwat.2016.11.016

(104) Salem, M. A.; Al-Zayadneh, W.; Cheruth, A. J. Water Conservation and Management with Hydrophobic Encapsulation of Sand. *Water Resources Management* **2010**, *24* (10), 2237-2246. DOI: 10.1007/s11269-009-9549-4

(105) González-Peñaloza, F. A.; Zavala, L. M.; Jordán, A.; Bellinfante, N.; Bárcenas-Moreno, G.; Mataix-Solera, J.; Granged, A. J. P.; Granja-Martins, F. M.; Neto-Paixão, H. M. Water repellency as conditioned by particle size and drying in hydrophobized sand. *Geoderma* **2013**, *209-210*, 31-40. DOI: 10.1016/j.geoderma.2013.05.022

(106) Atta, A.; Abdullah, M.; Al-Lohedan, H.; Mohamed, N. Coating Sand with New Hydrophobic and Superhydrophobic Silica/Paraffin Wax Nanocapsules for Desert Water Storage and Transportation. *Coatings* **2019**, *9* (2). DOI: 10.3390/coatings9020124

(107) Mitzel, M. R.; Sand, S.; Whalen, J. K.; Tufenkji, N. Hydrophobicity of biofilm coatings influences the transport dynamics of polystyrene nanoparticles in biofilm-coated sand. *Water Res* **2016**, *92*, 113-120. DOI: 10.1016/j.watres.2016.01.026

(108) Mosayebi, E.; Azizian, S.; Noei, N. Preparation of Robust Superhydrophobic Sand by Chemical Vapor Deposition of Polydimethylsiloxane for Oil/Water Separation. *Macromolecular Materials and Engineering* **2020**, *305* (12). DOI: 10.1002/mame.202000425

(109) Sinha Ray, S.; Dommati, H.; Wang, J.-C.; Lee, H. K.; Park, Y.-I.; Park, H.; Kim, I.-C.; Chen, S.-S.; Kwon, Y.-N. Facile approach for designing a novel micropatterned antiwetting

membrane by utilizing 3D printed molds for improved desalination performance. *Journal of Membrane Science* **2021**, *637*. DOI: 10.1016/j.memsci.2021.119641

(110) Clayton, K. N.; Salameh, J. W.; Wereley, S. T.; Kinzer-Ursem, T. L. Physical characterization of nanoparticle size and surface modification using particle scattering diffusometry. *Biomicrofluidics* **2016**, *10* (5), 054107.

(111) Shajari, M.; Rostamizadeh, K.; Shapouri, R.; Taghavi, L. Eco-friendly curcumin-loaded nanostructured lipid carrier as an efficient antibacterial for hospital wastewater treatment. *Environmental Technology & Innovation* **2020**, *18*, 100703.

(112) Zhang, X.; Sun, Y.; Mao, Y.; Chen, K.; Cao, Z.; Qi, D. Controllable synthesis of raspberry-like PS-SiO(2) nanocomposite particles via Pickering emulsion polymerization. *RSC Adv* **2018**, *8* (7), 3910-3918. DOI: 10.1039/c7ra13086d

(113) Tudu, B. K.; Sinhamahapatra, A.; Kumar, A. Surface Modification of Cotton Fabric Using TiO(2) Nanoparticles for Self-Cleaning, Oil-Water Separation, Antistain, Anti-Water Absorption, and Antibacterial Properties. *ACS Omega* **2020**, *5* (14), 7850-7860. DOI: 10.1021/acsomega.9b04067

(114) Deng, X.; Zhou, X.; Kamal, M. S.; Hussain, S. M. S.; Mahmoud, M.; Patil, S. A Modified Contact Angle Measurement Process to Suppress Oil Drop Spreading and Improve Precision. *Molecules* **2022**, *27* (4). DOI: 10.3390/molecules27041195

(115) Li, D. Drop size dependence of contact angles and line tensions of solid-liquid systems. *Colloids and Surfaces A: Physicochemical and Engineering Aspects* **1996**, *116*, 1-23.

(116) Wang, J.; Wu, Y.; Cao, Y.; Li, G.; Liao, Y. Influence of surface roughness on contact angle hysteresis and spreading work. *Colloid and Polymer Science* **2020**, *298* (8), 1107-1112. DOI: 10.1007/s00396-020-04680-x

(117) Ju, J.; Bai, H.; Zheng, Y.; Zhao, T.; Fang, R.; Jiang, L. A multi-structural and multi-functional integrated fog collection system in cactus. *Nat Commun* **2012**, *3*, 1247. DOI: 10.1038/ncomms2253

List of Publications

1. **Ritesh Soni**, Saikat Sinha Ray*, Chinna Bathula, Hyun-Seok Kim, Young-Nam Kwon*, and Chang Young Lee*, "Bio-adhesive based nanocoating to make superhydrophobic and self-cleaning surfaces", (In preparation) 2023.

2. Saikat Sinha Ray†, **Ritesh Soni**†, In-Chul Kim, You-In Park, Chang Young Lee*, and Young-Nam Kwon*, "Surface innovation for fabrication of superhydrophobic sand grains with improved water holding capacity for various environments applications", *Environmental Technology and Innovation*, vol. 28, pp. 102849-102861, 2022. († Contributed equally)

3. **Ritesh Soni**, Shalik Ram Joshi, Mamata Karmacharya, Hyegi Min, Shin-Kwan Kim, Sumit Kumar*, Gun-Ho Kim*, Yoon-Kyoung Cho*, and Chang Young Lee*, "Superhydrophobic and self-sterilizing surgical masks spray-coated with carbon nanotubes", *ACS Applied Nano Materials*, vol. 4, pp. 8491–8499, 2021.

4. Saikat Sinha Ray, **Ritesh Soni**, Dao Thi Thanh Huyen, Srinath R, Chang Young Lee, and Young-Nam Kwon*, "Chemical engineering of electrospun nanofibrous based three-layered nonwoven polymeric protective mask for enhanced performance", *Journal of Applied Polymer Science*, vol. 140, pp. 53584–53597, 2023.

5. Saikat Sinha Ray†, Pranav Peddinti†, **Ritesh Soni**, You-In Park, In-Chul Kim, Chang Young Lee, Byungmin Kim* and Young-Nam Kwon*, "Effectiveness of

nanoparticles-based ultrahydrophobic coating for concrete materials", *Journal of Building Engineering,* vol. 66, pp. p. 105799–105814, 2023.

6. Abu Talha Aqueel Ahmed, **Ritesh Soni**, Abu Saad Ansari, Chang Young Lee, Hyun-Seok Kim*, Hyunsik Im*, and Chinna Bathula*, "Biowaste-derived TiO2 interfaced graphitic carbon as anode for lithium-ion battery", *Surfaces and Interfaces*, vol. 35, pp. 102404-102410, 2022.